2019

Tuning of layered materials: Studies of CrAuTe4, PdSn4 and WTe2

Na Hyun Jo
Iowa State University

Tuning of layered materials: Studies of $CrAuTe_4$, $PdSn_4$ and WTe_2

by

Na Hyun Jo

A dissertation submitted to the graduate faculty

in partial fulfillment of the requirements for the degree of

DOCTOR OF PHILOSOPHY

Major: Condensed Matter Physics

Program of Study Committee:
Paul C. Canfield, Major Professor
Sergey L. Bud'ko
Adam Kaminski
John Lajoie
Rebecca Flint
Ralph E. Napolitano

The student author, whose presentation of the scholarship herein was approved by the program of study committee, is solely responsible for the content of this dissertation. The Graduate College will ensure this dissertation is globally accessible and will not permit alterations after a degree is conferred.

Iowa State University

Ames, Iowa

2019

DEDICATION

I would like to dedicate this dissertation to my family, Sang Dong Jo, Jung Wha Ko, Byung Sun Kim, In Sun Jo, Kyu Dong Jo, So Hyun Jo, Hyun Kyu Lee, and Amin Lee.

TABLE OF CONTENTS

Page

LIST OF TABLES

Page

LIST OF FIGURES

Page

ACKNOWLEDGEMENTS

When I recall the last six years of my Ph.D. life, there were many ups and downs. Thanks to lots of good people around me, I was able to overcome many obstacles and enjoy Ph.D. life. I would like to take this opportunity to express my gratitude to those who supported me in various ways.

First and foremost, I would like to thank my advisor Dr. Paul C. Canfield and unofficial co-advisor Dr. Sergey L. Bud'ko for their trust, support, and guidance. I have learned a lot about research from Dr. Paul C. Canfield and I am a lucky person to have him as my advisor. He is incredibly patient, enthusiastic, and thorough in regards to research. He has also supported me in various aspects of life including cooking and good food. I have learned a lot about instrumentation and critical thinking from Dr. Sergey L. Bud'ko. Discussions with him were always fruitful and many times heart warming. [Our promise: daisy, sunflower, or 4.99 Hyvee. Odd number for you and even number for me.]

I would like to thank all my committee members. Especially, Dr. Adam Kaminski and Dr. John Lajoie, who helped me through the hardest times of my Ph.D. life. I hope I will be able to help other students in the future as they did for me. Dr. Rebecca Flint was always willing to help not only with physics but also other subject concerns that I had. (In addition, thank you for your suggestion about the best pizza place in Prosecco.) I appreciate Dr. Ralph E. Napolitano for his time and valuable discussions about phase diagrams.

I would also like to thank to Dr. Peter P. Orth. I presented him with hard questions and he always did his best to help me. His guidance with the CMP journal club was invaluable to many students and early career researchers including myself. He and his family also saved me when I was struggling alone in Los Alamos.

I am very thankful for the help, support, and friendship that my colleagues have provided: Dr. Eundeok Mun, Dr. Halyna Hodovanets, Dr. Hyunsoo Kim, Dr. Sheng Ran, Dr. Anton

Jesche, Dr. Valentin Taufour, Dr. Tai Kong (Good friend who has the magic hand), Dr. Udhrara Kaluarachchi (GDM, the trouble maker but good friend), Dr. Wageesha Jayasekara, Dr. William Meier (My dearest "coworker" ever), Dr. Andreas Kreyssig (Great scientific discussions, quark and blue cheese was soooo good), Tej Lamichhane, Li Xiang (Little ant with incredible patience), Dr. Soham Manni, Dr. Anna Böhmer, Dr. Gil Drachuck, Mingyu Xu (Ready for next big hit), Amelia K. Estry (Penguin lover weirdo), Elizabeth Wille (Sissors), Dr. Raquel A. Ribeiro (Mom), Victor Barrena, Dr. Xiaojuan Xi (Happy virus), Dr. Elena Gati (Smart Elena), Brinda Kuthanazhi (Be strong Brinda), Scott Saunders, Dr. Andriy Palasyuk, Dr. Dominic Ryan (The right English, ham sandwich with quarter muffin), Juan Schmidt (Nerdy jokes), Dr. Myung-Hwa Jung, Dr. Douglas Finnemore, Dr. Lin-lin Wang (The best DFT), Dr. Yun Wu (The best ARPES), Dr. Manh Cuong Nguyen, Dr. Qisheng Lin, Dr. Benjamin Ueland, Dr. Robert McQueeney, Michael Onyszczak, Morgan Masters, Dr. Makariy Tanatar, Dr. Kyuil Cho, Dr. Joongmok Park, Dr. Richard Kim, and Kyungchan Lee, and the undergrad army: Savannah Downing, Kathryn Neilson, and Connor Schmidt.

I would like to thank Dr. Yujin Cho (I would not able to make it without you.), Dr. Chung-man Kim, Dr. Jasmine Choi, Dr. Daeho Rho, Zach Hand, and my friends in Ames who have accompanied me and brought me joy.

I would like to thank the Gordon and Betty Moore Foundation for supporting me during my Ph.D. through their EPiQS Initiative (Grant No. GBMF4411). This work was also supported by the U.S. Department of Energy (DOE), Office of Basic Energy Sciences, Division of Materials Sciences and Engineering at the Ames Laboratory under contract number DE-AC02-07CH11358. Ames Laboratory is operated for the DOE by Iowa State University.

ABSTRACT

Layered materials are of great and growing interest for material scientists and condensed matter physicists, not only because of their possible applications but also because of the diverse and controllable ground states. In addition, tuning of layered materials through external fields, doping, or strain can lead to the emergence of novel phenomena. In this dissertation, the importance of the study of layered materials is emphasized in Chapter 1. Before getting into experimental results, the theoretical background and experimental methods, including growth of single crystals of selected layered materials, are introduced in Chapter 2 and Chapter 3. Chapters 4, 5 and 6 are devoted to experimental results on selected layered materials. Chapter 4 presents the physical properties of $CrAuTe_4$ at ambient pressure and the tuning of its properties using hydrostatic pressure. The physical properties of $PdSn_4$ are shown in Chapter 5, and then the origin of extremely large magnetoresistance in this material is discussed in comparison/contrast to the physical properties of $PtSn_4$. Chapter 6 focuses on the tuning of the physical properties of WTe_2 using temperature, magnetic field and uniaxial strain. In appendix A, I list all the growth attempts regarding Te and Se containing materials. In appendix B, I explain the growth of single crystal, $EuCd_2As_2$, using salt (NaCl/KCl) as a solution. In appendix C, I summarize other publications during my Ph.D. years.

CHAPTER 1. INTRODUCTION

The 2010 Nobel prize in physics was awarded to Dr. Geim and Dr. Novoselov for groundbreaking experiments on graphene, the monolayer of graphite. [1] Graphene has received much attention since then, not only because of its possible applications but also because it became a test ground for numerous exotic effects. [2, 3] However, the lack of a band gap in graphene has stimulated the search for other 2D materials, including transition metal dichalcogenides, for possible future application purposes. [4] The search became more important as heterostructures built from layers of two dimensional materials have more readily available and studied. [5]

Even before the discovery of graphene, bulk layered materials were of great interest in condensed matter physics. This is because layered materials are usually considered to manifest reduced dimensionality and exhibit anisotropic properties or quasi-two dimensional Fermi surfaces. Such reduced dimensionality is thought to enhance the likelihood of discovering (and understanding) interesting ground states like charge density waves, superconductivity etc. [6] For example, the charge density wave phase in 2H-$NbSe_2$ has intrigued condensed matter physicists for decades. [7, 8]

Tuning of layered materials through applied fields, doping, pressure or strain can lead to the emergence of novel phenomena. For instance, an external magnetic field changes the resistance of WTe_2 enormously ($\mathrm{MR} \sim 10^5\,\%$ at $B = 14.7\,\mathrm{T}$ and $T = 4.5\,\mathrm{K}$). [9] Superconductivity has been found upon the suppression of the charge density wave ground state by applying pressure on the transition metal dichalcogenides such as TaS_2 and $TaSe_2$. [4] In addition, superconductivity is found in proximity to magnetism in the cuprates and iron pnictides, and the interplay of these phases can be studied via doping or pressure. [10]

In this dissertation, I will discuss how tuning affects the properties of selected bulk layered materials. This dissertation includes a description of both the growth of these materials, as well as the experimental efforts to tune their properties. Firstly, the effect of the hydrostatic pressure on

the antiferromagnetic material $CrAuTe_4$ was studied. (Chapter 4) Secondly, by comparing $PtSn_4$ and $PdSn_4$, we tried to understand the origin of the extremely large magnetoresistance in these materials. (Chapter 5) Thirdly, we grew and studied WTe_2. (Chapter 6) We devised an improved synthetic route, and studied resistivity, thermoelectric power and angle resolved photoemission spectroscopy (ARPES). In addition, we discovered that uniaxial strain has huge impacts on WTe_2. In particular, elastoresistance in WTe_2 exhibits an unusual non-monotonic behavior as a function of temperature that arises from peculiar details of the band structure and its response to strain in this material. For the first time, we consider the effects of magnetic fields on elastoresistance by combining magnetic field and strain in our experiment. We observe an unprecedented sensitivity of the elastoresistance to applied magnetic fields over the full temperature range and hitherto unknown elastoresistance quantum oscillations in the low temperature regime.

CHAPTER 2. BASIC THEORY

2.1 Two-band model of electrical conductivity

We are interested in modeling magnetoresistance and Hall effect to obtain information about carrier densities and mobilities. The simple two band model of electrical conductivity works well for analyzing data for $PdSn_4$. This section is based on Refs. [11, 12].

On the basis of a condensed Fermi gas of electrons with an approximately spherical Fermi surface, the classical Drude conductivity is;

$$\sigma_0 = \frac{ne^2\tau}{m^*} \tag{2.1}$$

with electron density n, effective mass m^* and relaxation time τ. In the presence of the magnetic field B, electronic motion is bent due to the Lorentz force $F = ev \times B$ where v is the velocity of electrons. This results in an angular velocity $\omega_c = eB/m^*$ such that $\gamma \equiv \omega_c\tau = \frac{eB\tau}{m^*}$. If we consider this motion of electrons as cyclotron confined to a surface rather than spiral, we can express the conductivity as two by two tensor. Here, the plane normal to B is treated as a complex plane for convenience. In this sense, conductivity in the magnetic field can be written as;

$$\sigma = \frac{\sigma_0}{1 - i\gamma}. \tag{2.2}$$

If both electrons and holes are present in the system, the total conductivity is given by

$$\sigma = \frac{\sigma_e}{1 - i\gamma_e} + \frac{\sigma_h}{1 - i\gamma_h}. \tag{2.3}$$

Resistivity is simply $1/\sigma$

$$\rho = \frac{1}{\sigma} = \frac{B}{n_e} \frac{\left[\gamma_e + c\gamma_h + \gamma_e\gamma_h\left(\gamma_h + c\gamma_e\right)\right] - i\left[\gamma_e^2 - c\gamma_h^2 + (1-c)\,\gamma_e^2\gamma_h^2\right]}{\left(\gamma_e + c\gamma_h\right)^2 + (1-c)^2\gamma_e^2\gamma_h^2} \tag{2.4}$$

where $c = n_h/n_e$, and then the matrix representation of complex numbers gives

$$\rho_{xx}\left(B\right) = \frac{1}{e} \frac{\left(n_h\mu_h + n_e\mu_e\right) + \left(n_h\mu_e + n_e\mu_h\right)\mu_h\mu_e B^2}{\left(n_h\mu_h + n_e\mu_e\right)^2 + \left(n_h - n_e\right)^2{\mu_h}^2{\mu_e}^2B^2} \tag{2.5}$$

$$\rho_{xy}(B) = \frac{B}{e}\frac{\left(n_h{\mu_h}^2 - n_e{\mu_e}^2\right) + (n_h - n_e)\,{\mu_h}^2{\mu_e}^2B^2}{(n_h\mu_h + n_e\mu_e)^2 + (n_h - n_e)^2{\mu_h}^2{\mu_e}^2B^2} \tag{2.6}$$

where $\mu = \gamma/B$. Note that $\rho_{xx}(B) - \rho_{xx}(B=0)/\rho_{xx}(B=0)$ is called the magnetoresistance and ρ_{xy} is called the Hall resistivity.

If the system is not compensated ($n_e \neq n_h$), ρ_{xx} and ρ_{xy} can be expanded in the low magnetic field regime as follows:

$$\rho_{xx} = \frac{1}{n_e\mu_e + n_h\mu_h} + B^2\left(\frac{n_e\mu_e{\mu_h}^2 + n_h\mu_h{\mu_e}^2}{(n_e\mu_e + n_h\mu_h)^2} - \frac{(n_h - n_e)^2{\mu_e}^2{\mu_h}^2}{(n_e\mu_e + n_h\mu_h)^3}\right) + O\left[B^4\right]. \tag{2.7}$$

$$\rho_{xy} = \frac{B}{e}\frac{\left(n_h\mu_h^2 - n_e\mu_e^2\right)}{(n_h\mu_h + n_e\mu_e)^2} + O\left[B^3\right] \tag{2.8}$$

While in the high magnetic field limit, based on Eq. 2.5 and 2.6

$$\rho_{xx} = \frac{1}{e}\frac{(n_h\mu_e + n_e\mu_h)}{(n_h - n_e)^2\mu_h\mu_e} \tag{2.9}$$

$$\rho_{xy} = \frac{B}{e}\frac{1}{(n_h - n_e)}. \tag{2.10}$$

Thus the magnetoresistance initially shows a quadratic increase before saturating at higher magnetic fields. In addition, the Hall resistivity is a linear function of magnetic field.

In a perfectly compensated metal ($n_e = n_h$), the behavior of magnetic field dependent resistivity is rather simple. The magnetoresistance is purely quadratic without any approximation, and does not saturate even at high magnetic fields. Note that this non-saturating behavior in a compensated metal does not necessarily guarantee an extremely large magnetoresistance, because of the proportionality factor in front of B^2 in Eq. 2.5. In other words, the magnetoresistance value can remain small if the mobilities of carriers are small. Similarly, the Hall resistivity is linear in B without any approximation, $\rho_{xy} = \frac{B}{e}\frac{\left(n_h\mu_h^2 - n_e\mu_e^2\right)}{(n_h\mu_h + n_e\mu_e)^2}$. Here, the sign of the Hall resistivity reflects that of the dominant carrier.

A nearly compensated metal ($n_e \sim n_h$, $c = n_h/n_e = 1 \pm \epsilon$ ($\epsilon \ll 1$)) behaves similarly to an uncompensated system but needs a higher magnetic field before it saturates. In addition, we need to retain terms of higher order in B for the low-field Hall resistivity approximation leading to possible nonlinearities in the magnetic field response.

2.2 Kohler's rule

We are interested in scailing large magnetoresistance and temperature dependent resistance data. Kohler's rule may give us more information about large magnetoresistance in $PdSn_4$ and $PtSn_4$. This section is based on Refs. [11, 13, 14].

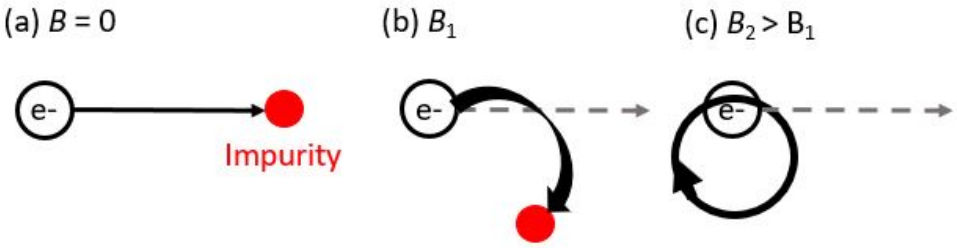

Figure 2.1 (a) Electron motion without any applied magnetic field (b) Electron motion with an applied magnetic field of B_1 (c) Electron motion with an applied magnetic field of B_2 which is larger than B_1

In the free electron gas model, the electron motion in the magnetic field can be deviated or even described as cyclotron motion in the plane perpendicular to the applied magnetic field direction. (see Fig. 2.1) As the magnetic field increases, mean free path (l) is gradually taken over by the Larmor radius (r_L). Based on this picture, we can assume $\rho(B,T)/\rho(0,T)$ depends only on the ratio l/r_L. Since $r_L \propto B^{-1}$ and $l \propto [\rho(0,T)]^{-1}$, $\rho(B,T)/\rho(0,T)$ may be considered to be dependent only on the $B/\rho(0,T)$. This is called Kohler's rule and can be expressed as a scaling function;

$$\Delta\rho/\rho(0,T) = F(B/\rho(0,T)) \tag{2.11}$$

where $\Delta\rho$ is $\rho(B,T) - \rho(0,T)$. F is a function depending on the geometrical configuration and on the metal. In general, scaling usually follows the power law; $(B/\rho(0,T))^n$ with $n \sim 2$, but there are changes of slope at high fields.

Note that Kohler's rule holds only if the extra collisions are of the same sort: more impurities or more phonons with the same frequency distribution. In particular, it can break down when the orbit is quantized, open trajectories are present or the scattering mechanism changes (such as from magnetic impurities). In addition, this rule is not strictly valid for an anisotropic metal.

2.3 Quantum oscillations

This section is based on Refs. [15, 16, 17].

In Section 2.2, we discussed about the cyclotron motion of electrons in the magnetic field. Cyclotron motion in a quantum picture leads to quantization, and forms discrete Landau levels. This manifests as oscillatory effects occurring in density of states and various physical quantities under special conditions: strong magnetic field, low temperature, and high purity single crystals. By analyzing quantum oscillation, the Fermi surface information can be inferred.

2.3.1 Density of states of the two-dimensional and three-dimensional electron gas in magnetic fields

For a two-dimensional electron gas without the magnetic field, the density of states (DOS) is continuous and constant in terms of energy. (Fig. 2.2 (a) blue dashed line) The DOS becomes discrete in the presence of the magnetic field. (Fig. 2.2 (a) red solid lines) To be more specific, let's assume the electron motion is in the xy plane with applied field along the z direction. Then, the Hamiltonian can be written as

$$H = \frac{1}{2m}(p_x + \frac{e}{c}A_x)^2 + \frac{1}{2m}(p_y + \frac{e}{c}A_y)^2 \tag{2.12}$$

where e is the absolute value of the electron charge, the effective mass is taken equal to the electron mass m, and $A(r)$ is the vector potential of the magnetic field. For simplicity, the vector

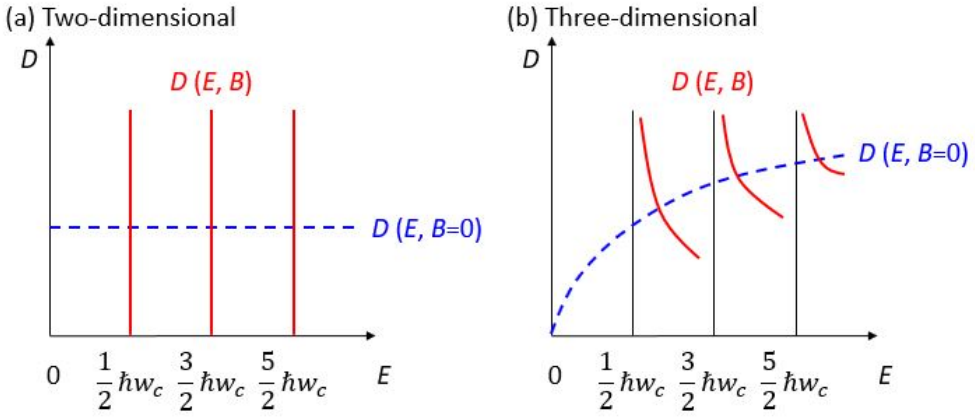

Figure 2.2 (a) Density of states of a two-dimensional electron gas without the magnetic field (blue dashed line) and with the magnetic field (red solid line) (b) Density of states of a three-dimensional electron gas without the magnetic field (blue dashed line) and with the magnetic field (red solid line)

potential can be chosen as $A(r) = (-By, 0, 0)$ by placing the magnetic field along z direction. The Hamiltonian then becomes

$$H = \frac{1}{2m}(p_x - \frac{eB}{c}y)^2 + \frac{1}{2m}p_y^2 = \frac{1}{2}m\omega_c^2(y - y_0)^2 + \frac{1}{2m}p_y^2 \tag{2.13}$$

where $\omega_c = \frac{eB}{mc}$ (cyclotron resonance frequency), $y_0 = \frac{\hbar c}{eB}k_x$ (centers of oscillation), and $l = \sqrt{\frac{\hbar c}{eB}}$ (magnetic length). Corresponding eigenvalues are

$$E_{nk_x} = (n + \frac{1}{2})\hbar\omega_c \qquad n = 0, 1, 2, ..., \tag{2.14}$$

where n indicates the Landau level. Since the energy levels do not depend on k_x, their degeneracy is given by the number of allowed k_x values of the system. In particular, the orbital degeneracy $N_L(B)$ of a Landau level is

$$N_L(B) = \frac{L_x}{2\pi}\frac{eB}{\hbar c}L_y = \frac{e}{hc}BS \tag{2.15}$$

in the condition of $0 \leq y_0 = \frac{\hbar c}{eB}k_x < L_y$, where L_x and L_y are the lengths of the rectangular box where the electron is confined, and $S = L_xL_y$. This implies that the degeneracy is proportional to the applied magnetic field which means piling up of states into discrete Landau levels. At the same time, the separation of the Landau levels is proportional to the applied magnetic field based on Eq. 2.14.

For a three-dimensional electron gas without an applied magnetic field, the DOS is proportional to $E^{1/2}$. (Fig. 2.2 (b) blue dashed line) The DOS becomes discrete in the presence of the magnetic field. (Fig. 2.2 (b) red solid lines) Assuming the same configuration as for the two-dimension case above, the Hamiltonian is

$$H = \frac{1}{2m}(p_x - \frac{eB}{c}y)^2 + \frac{1}{2m}p_y^2 + \frac{1}{2m}p_z^2, \tag{2.16}$$

and the eigenvalues are

$$E_{nk_z} = (n + \frac{1}{2})\hbar\omega_c + \frac{\hbar^2 k_z^2}{2m}. \tag{2.17}$$

Here, the DOS of the n-th sub-band can be obtained using the one-dimensional character of the dispersion ($\propto E^{-1/2}$) along z, $N_L(B)$ from two-dimensional case, and the spin degeneracy.

$$D_n(E,B) = \frac{L_z}{2\pi}(\frac{2m}{\hbar^2})^{1/2}\frac{1}{\sqrt{E-(n+\frac{1}{2})\hbar\omega_c}}N_L(B)\,2 \quad \text{for} \quad E > (n+\frac{1}{2}\hbar\omega_c) \tag{2.18}$$

Summing up the contributions from every Landau sub-band,

$$D(E,B) = \frac{L_z}{\pi}(\frac{2m}{\hbar^2})^{1/2}N_L(B)\sum_{n=0}^{\infty}\frac{1}{\sqrt{E-(n+\frac{1}{2})\hbar\omega_c}}\Theta[E-(n+\frac{1}{2})\hbar\omega_c] \tag{2.19}$$

where $\Theta(x)$ is the step function. This indicates that the DOS becomes infinite at the edge of the Landau levels and then is proportional to $E^{-1/2}$ as shown in Fig. 2.2 (b) by the red solid lines.

2.3.2 de Haas-van Alphen effect

An intuitive way of understanding quantum oscillation is through Landau tubes. Let's assume a spherical Fermi surface. Then, the quantized energy (Eq. 2.17) can be thought as cylinders in k-space as shown in Fig. 2.3. This cylinders are called Landau tubes. As the magnetic fields are increased, the Landau tubes move outward. Once it crosses the extremal areas of the Fermi surface, sharp changes of DOS can happen. Therefore, a periodic variation of DOS at the Fermi surface as a function of $1/B$ can be observed.

To be more specific, Landau levels are formed in an electron gas system in response to an applied magnetic field. This increases the overall energy and gives rise to Landau diamagnetism. Besides

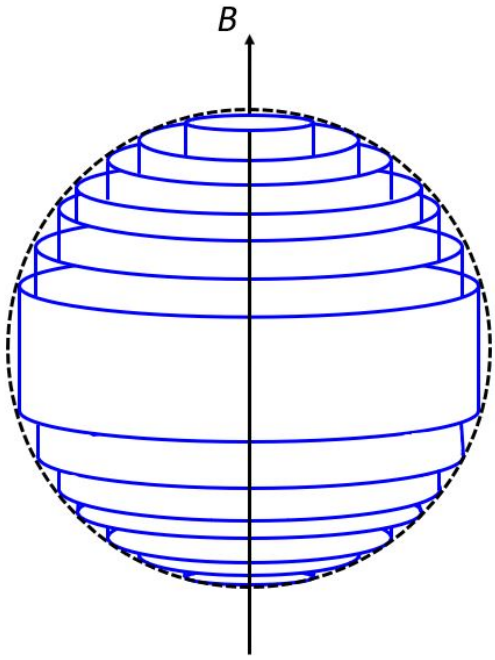

Figure 2.3 Landau tubes for spherical Fermi surface

that, we can consider the population and depopulation effects as the Landau levels cross the Fermi energy. Because of this sharp change, oscillations in the ground-state energy are expected. As a consequence, the magnetization will also oscillate. The period of such oscillations is

$$(j+\frac{1}{2})\hbar\omega_c = (j+\frac{1}{2})\hbar\frac{eB_j}{mc} = E_F \quad \Leftrightarrow \quad \frac{1}{B_j} = (j+\frac{1}{2})\frac{\hbar e}{mcE_F} \tag{2.20}$$

where j is an integer. Therefore, the oscillations in magnetic susceptibility, called de Haas-van Alphen oscillations, are periodic in inverse magnetic field with period $\frac{\hbar e}{mcE_F}$. The oscillations in resistivity, due to the same variation in the DOS, are called Shubnikov de Haas oscillations. Note that the sharpness of the Fermi-Dirac distribution function is required to observe the oscillation in an experiment. This means that (i) the applied magnetic field should be large and temperature should be low ($k_BT \ll \hbar\omega_c$) and (ii) the crystal has to be very clean (or pure) ($\omega_c\tau \gg 1$).

In a three dimensional system with parabolic dispersion ($E_F = \hbar^2k_F^2/2m$), we can rewrite Eq. 2.20 as

$$\Delta(\frac{1}{B}) = (\frac{1}{B})_{j+1} - (\frac{1}{B})_j = \frac{e}{\hbar c}\frac{2\pi}{\pi k_F^2}. \tag{2.21}$$

Here, πk_F^2 correspond to the extremal areas in the k-plane, perpendicular to the applied magnetic field direction and enclosed by the Fermi energy. This is because the DOS also becomes extremal.Therefore, extremal area of Fermi surface perpendicular to the applied magnetic field direction can be experimentally obtained by analyzing frequencies of oscillations.

2.3.3 Lifshitz-Kosevich theory

The theoretical expression for the oscillations in magnetization was suggested by Lifshitz and Koshevich:

$$M_{osc} = \sum_r \sum_i \frac{(-1)^r}{r^{3/2}} A_i sin(\frac{2\pi r F_i}{B} + \beta_i), \tag{2.22}$$

$$A_i \propto B^{1/2} \left| \frac{\partial^2 S_i}{\partial k_H^2} \right|^{-1/2} R_T R_D R_S, \tag{2.23}$$

$$R_T = \frac{\lambda r m_{ci}^* T/B}{sinh(\lambda r m_{ci}^* T/B)}, \tag{2.24}$$

$$R_D = exp(-\lambda r m_{ci}^* T_D/B), \tag{2.25}$$

$$R_S = cos(\pi g_i r m_{ci}^*/2m_0), \tag{2.26}$$

$$\lambda = 2\pi^2 c k_B/e\hbar \sim 14.69\,\mathrm{T/K} \tag{2.27}$$

where i indicates each orbit, r is the harmonics and g_i is the free electron value. The formula states that finite temperature (R_T), finite electron relaxation time (R_D) and electron spin (R_S) can introduce phase smearing.

From the thermal damping (R_T) term, the cyclotron effective mass (m_{ci}^*) can be obtained. To be more specific, the magnetic field dependent resistivity at fixed temperature data need to be measured with fine step sizes (Quantum Design Physical Property Measurement System: persistent mode with less than 250 Oe step). At least five sets of data with different temperatures are required. Each data set has to be processed the same way: the magnetic field range, number of points etc. Details about data processing can be found in Chapter 6. Plot the amplitude of a frequency as a

function of temperature, and fit with Eq. 2.24. Then, one can get cyclotron effective mass of the frequency. Similarly, the so called mass plot can be used. Eq. 2.24 can be transformed into

$$ln\frac{A_i}{T}[1 - exp(\frac{-2\lambda m^*_{ci}T}{B})] = -\frac{\lambda m^*_{ci}}{B}T + const. \tag{2.28}$$

Using Eq. 2.28 and a method of successive approximation, the cyclotron effective mass can be obtained.

The R_D term is related to the Landau level broadening k_BT_D, where T_D is called Dingle temperature. T_D reflects by both the lifetime broadening and the inhomogeneous broadening caused by impurities, crystalline imperfections and strains. It is given by

$$T_D = \frac{\hbar}{2\pi k_B}\frac{1}{\tau}. \tag{2.29}$$

In order to determine T_D, the field dependence of the oscillation amplitude needs to be measured. Equations 2.23-2.25 yield

$$ln[A_iH^{1/2}sinh(\frac{\lambda m^*_{ci}T}{B})] = -\lambda m^*_{ci}T_D\frac{1}{B} + const. \tag{2.30}$$

A plot of $ln[A_iH^{1/2}sinh(\frac{\lambda m^*_{ci}T}{B})]$ as a function of $1/B$ at constant T is called a Dingle plot. From the slope of the plot, one can obtain the Dingle temperature. Note that m^*_{ci} should be obtained prior to this analysis.

2.4 Lifshitz transition

This section is based on Refs. [18, 19].

In the energy spectrum of the conduction electrons, the energy (E_k), where the topology of the Fermi surface changes, can exist. In many cases, this critical energy point (E_k) is far from the chemical potential (μ). However, there are some cases where a continuously changing parameter cause the difference, $z = \mu - E_k$, to pass through zero. Such zero crossing also causes peculiarities of the density of states which leads to singular anomalies of thermodynamic and kinetic characteristics of the electron gas in the metal. Note that these changes in the topology of the Fermi surface are not related to changes in the symmetry of the lattice. It is not a second order phase transition. Instead,

the Lifshitz transition is considered to be a 2.5 order phase transition with the order parameter z. This is because the second derivative of the thermodynamic potential has a singularity at $z^{1/2}$ and the third derivative of the thermodynamic potential has a singularity at $z^{-1/2}$.

Parameters that can induce a Lifshitz transition include pressure, [20, 21] chemical doping, [22, 23] and temperature. [24] The chemical doping can be problematic, because it is also considered as a sort of impurity (disorder in system). Thus, doping level needs to be finite. To be more specific, the Fermi surface loses its exact meaning for an irregular lattice, owing to the absence of translational symmetry. Thus, the density of state can be smeared out.

2.5 Strain

This section is based on Refs. [25, 26, 27, 28].

2.5.1 Stress tensor

There are forces exerted on the surface of an object and proportional to the area of the surface of an object. Stress (τ) is defined as the force (F) divided by the area (A), $\tau = F/A$. It has nine components and is a second-rank tensor, $\tau_{\alpha\beta}$ where α, $\beta = x, y, z$ or in matrix form

$$\begin{pmatrix} \tau_{xx} & \tau_{xy} & \tau_{xz} \\ \tau_{yx} & \tau_{yy} & \tau_{yz} \\ \tau_{zx} & \tau_{zy} & \tau_{zz} \end{pmatrix}. \tag{2.31}$$

Here, diagonal terms are called the normal components and off diagonal terms are called the shear components. This can be visualized as Fig. 2.4.

Two particular stresses are relevant to this dissertation. One is uniaxial stress, T, along [100]. This can be written in matrix forms:

$$\begin{pmatrix} T & 0 & 0 \\ 0 & 0 & 0 \\ 0 & 0 & 0 \end{pmatrix}. \tag{2.32}$$

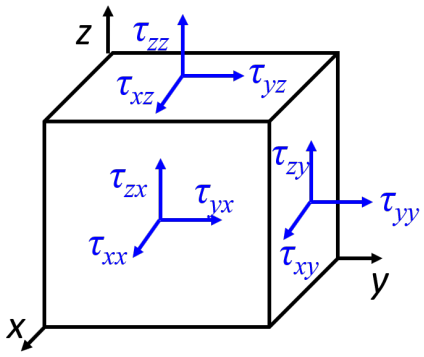

Figure 2.4 Stress tensor

The other is hydrostatic pressure, p, which can be expressed as

$$\begin{pmatrix} -p & 0 & 0 \\ 0 & -p & 0 \\ 0 & 0 & -p \end{pmatrix}. \tag{2.33}$$

This is because pressure is a force that only acts perpendicular to the surface. Therefore, all shear stresses are zero. In addition, hydrostatic pressure means uniform pressure on all surfaces of the specimen.

The hydrostatic pressure mainly changes lattice parameters and corresponding electronic structures. It can sometimes modify the structure of a crystal depends on the range of applied hydrostatic pressure and the details of crystal structure. [29] On the other hand, the uniaxial stress not only can changes the lattice parameters, but also can break a symmetry of a crystal.

2.5.2 Strain tensor

Stress induces stain. For better understanding, we will start with the one-dimensional case. Let's assume an extendible string like a rubber band as shown in Fig. 2.5.

The origin is marked as O. After stretching, an arbitrary point P on the string moves to P'. Similarly, a point Q, near P, moves to Q'. Strain does not care about the actual displacement but

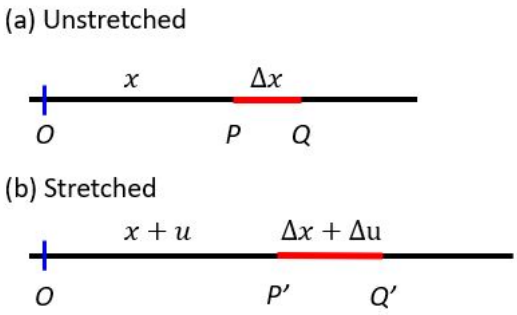

Figure 2.5 The deformation of an extendible string. (a) Unstreched. (b) Streched.

rather the relative displacements. To be more specific, the strain of the section PQ is defined as

$$\frac{increase\ in\ length}{original\ length} = \frac{P'Q' - PQ}{PQ} = \frac{\Delta u}{\Delta x}. \tag{2.34}$$

The strain at the point P is

$$\epsilon = \lim_{\Delta x \to 0} \frac{\Delta u}{\Delta x} = \frac{du}{dx}. \tag{2.35}$$

If we expand the one-dimensional argument to the three-dimensional case, the variation of the displacement u_i with position x_i in the body is used to define nine tensor components

$$\epsilon_{ij} = \frac{\partial u_i}{\partial x_j}, \text{where } i, j = 1, 2, 3. \tag{2.36}$$

or in matrix form:

$$\begin{pmatrix} \epsilon_{11} & \epsilon_{12} & \epsilon_{13} \\ \epsilon_{21} & \epsilon_{22} & \epsilon_{23} \\ \epsilon_{31} & \epsilon_{32} & \epsilon_{33} \end{pmatrix}. \tag{2.37}$$

2.5.3 Hooke's law

Hooke's law is in general linear response between force and displacement. ($F = k\Delta x$) In this particular case, Hooke's law states that below the elastic limit the amount of strain is proportional to the magnitude of the applied stress.

$$\epsilon_{ij} = \sum_{\alpha\beta} S_{ij\alpha\beta}\tau_{\alpha\beta} \quad \text{or} \quad \tau_{\alpha\beta} = \sum_{ij} C_{\alpha\beta ij}\epsilon_{ij} \tag{2.38}$$

Here, $S_{ij\alpha\beta}$ is the elastic compliance constant or compliance. $C_{\alpha\beta ij} = S^{-1}_{ij\alpha\beta}$ is the elastic stiffness constant or stiffness. If we change this tensor notation to matrix (Voigt) notation (i.e. $11 \rightarrow 1$, $22 \rightarrow 2$, $33 \rightarrow 3$, 23 & $32 \rightarrow 4$, 31 & $13 \rightarrow 5$, and 12 & $21 \rightarrow 6$),

$$\epsilon_k = \sum_l S_{kl}\tau_l \quad \text{, where } k, l = 1, 2, 3, 4, 5, 6. \tag{2.39}$$

Note that the Hooke's law is only true below the elastic limit. In the elastic regime, the strain is recoverable. In other words, the object returns to its original shape when the stress is removed. Once the object experience a stress beyond the elastic limit, it undergoes plastic deformation.

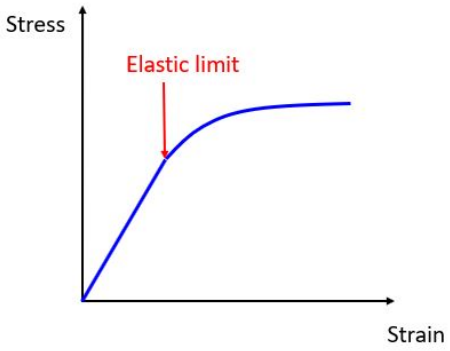

Figure 2.6 Stress-strain curve.

Although the detailed form of the stess-strain curve (shown in Fig. 2.6) varies a lot between materials, the elastic limit can be determined as the point where the curve starts to deviate from linear behavior.

2.5.4 Piezoelectricity

If a stress is applied to certain crystals they develop an electric moment whose magnitude is proportional to the applied stress. This is known as the direct piezoelectric effect. In the opposite sense, when an electric field is applied to a piezoelectric crystal the shape of the crystal will change slightly. This is called the converse piezoelectric effect. Interestingly, there is a linear relation

between the electric field within the crystal and the strain tensor which describes the change of shape.

$$\epsilon_{jk} = \sum_i d_{ijk} E_i \tag{2.40}$$

where the d_{ijk} are the piezoelectric moduli.

2.5.5 Gauge factor and elastoresistance tensor

The elastoresistance (a.k.a. Gauge factor) of a material characterizes the changes of the resistance of the material due to the stress experienced by the material. Based on the definition of resistance, $R = \rho\frac{L}{A}$, changes in the resistance can be written as

$$\frac{dR}{R} = \frac{d\rho}{\rho} + \frac{dL}{L} - \frac{dA}{A}. \tag{2.41}$$

The first term is the change in the resistivity of the material due to changes in the electronic properties of the material. The second and third terms are purely geometrical factors. Let's consider a system with a cylindrical rod and strain along the length direction. Then, strain can be defined as $\epsilon = \frac{dL}{L}$ and geometrical factors can be simplified with Poisson's ratio (ν): $\nu = \frac{dr}{r}/\epsilon$, where r is radius of the cylindrical rod. The Gauge factor (GF) can be obtained:

$$GF = (\frac{(dR/R)}{\epsilon}) = \frac{(d\rho/\rho)}{\epsilon} + (1 + 2\nu). \tag{2.42}$$

The GF of ordinary metals, like copper, is temperature independent with a magnitude around 2. This is because the geometric factors are the dominant term and Poisson's ratio for most metals is $0.3 < \nu < 0.5$. [30]

In reality, it can be more complicated because all physical quantities are tensors and the crystal symmetry matters. Then the resistivity component can be described by:

$$(\frac{d\rho}{\rho})_i = \sum_{k=1}^{6} m_{ik}\epsilon_k \tag{2.43}$$

where m_{ik} is the elastoresistive strain matrix and ϵ_k is the strain tensor in Voigt notation (or matrix form). Here, m_{ik} is depend on cyrstal symmetry. In this dissertaion, only orthorhombic structures

are studied under uniaxial strain. For an orthorhombic structure, there are nine independent terms in the elastoresistivity tensor: [28]

$$\begin{pmatrix} m_{11} & m_{12} & m_{13} & 0 & 0 & 0 \\ m_{12} & m_{22} & m_{23} & 0 & 0 & 0 \\ m_{13} & m_{23} & m_{33} & 0 & 0 & 0 \\ 0 & 0 & 0 & m_{44} & 0 & 0 \\ 0 & 0 & 0 & 0 & m_{55} & 0 \\ 0 & 0 & 0 & 0 & 0 & m_{66} \end{pmatrix}. \tag{2.44}$$

CHAPTER 3. EXPERIMENTAL METHODS

One of the most intriguing parts of studying condensed matter physics, in contrast to many other areas of physics (e.g. astrophysics, nuclear and particle physics etc.), comes from the fact that it offers better access to diverse, reproducible and tunable experiments. For example, astrophysics is more like observational physics rather than experimental physics, while nuclear and particle experimental physics require so much effort including thousands of people, years of time and huge instruments. On the other hand, experimental condensed matter physics can be done in a laboratory with controllable, extreme environments such as low or high temperature, high magnetic fields, pressures and strains. In addition, its subjects of study are diverse. Condensed matter physics researchers can create and explore fractional charge, exotic superconductivity or even new particle such as Majorana fermions in laboratory settings. [31]

3.1 Crystal growth

The first step of experimental condensed matter physics often is growing a good quality crystals. They can be as simple as an element or compounds with various elements, and each of them has their own properties. Considering the 80 stable, non-noble gas, elements on the periodic table as a building blocks, one can imagine an almost unlimited playground of experimental condensed matter systems. For the studies presented in this dissertation, bulk single crystals were synthesized. There are some advantages to using single crystals over polycrystals. For example: (i) anisotropic thermodynamic and transport properties can be studied or (ii) electronic structures (a.k.a band structures) can be experimentally studied through ARPES and quantum oscillations. It is important to understand the band structures of crystals, because the band structure near the Fermi level is key to understanding many of their intrinsic physical properties.

There are several techniques for growing bulk single crystalline samples: vapor transport, floating zone, Bridgman method and solution growth. [32] Here, high temperature solution growth will be discussed. The principle of solution growth is similar to that of the growth of a salt crystal out of cooling saturated salty water. To be more specific, salt (NaCl, melting temperature of 801 °C) can be dissolved in hot water ($\leq$100 °C). On cooling (or evaporating water), crystals of salt can be obtained. Similarly, one can dissolve higher melting elements into a solvent of lower melting elements, and then single crystals can be obtained on cooling. The solvent can be one element or a mixture of elements comprising the final compound, or some other compounds (eg. water for salt growth). In the following, some details about high temperature solution growth will be explained using examples.

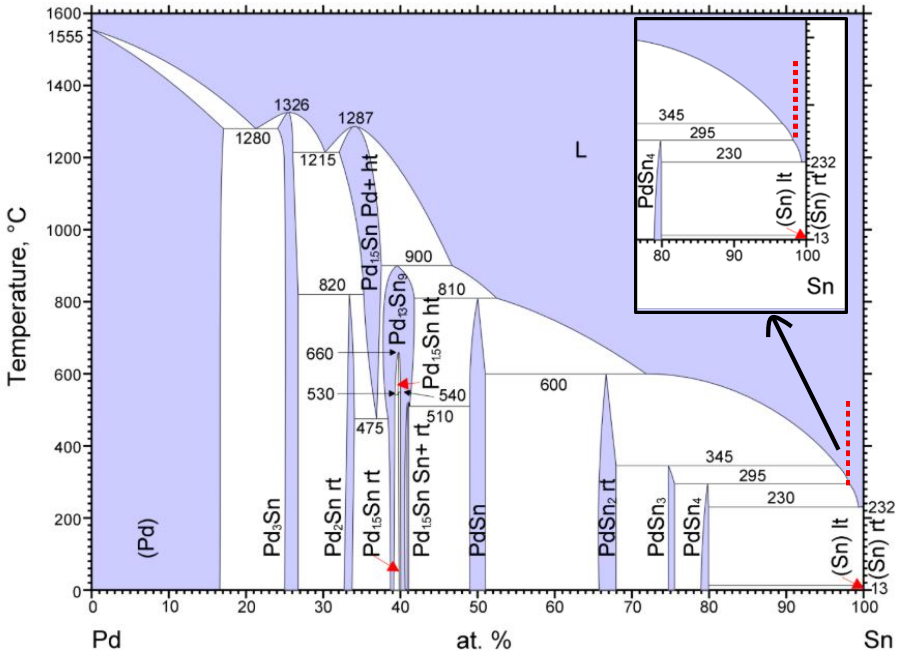

Figure 3.1 Phase diagram of Pd-Sn from ASM alloy phase diagram. [33] Inset shows the enlarged right bottom conner of the phase diagram. Reprinted with permission of ASM International. All rights reserved. www.asminternational.org

A phase diagram has composition and temperature information about how to potentially grow the target compound. As an example, Fig. 3.1 shows the phase diagram of Pd-Sn. Blue color stands for single phase regions and white color indicates two phase regions. The large blue area on

the top/right of the phase diagram is the homogeneous liquid regime. The boundary between the liquid region and the white, two phase region is called the liquidus line, where solid crystals start to precipitate on cooling below the line. I will use this phase diagram to illustrate how we grew single crystals of $PdSn_4$.

To start, the starting stoichiometry should be in the range where the $PdSn_4$ liquidus line can be intersected upon cooling. Since the window for $PdSn_4$ is relatively small, the initial stoichiometry of Pd_2Sn_{98} can be a reasonable choice (Fig. 3.1 inset). To contain the growth, a fritted alumina crucible [CCS] [34] was chosen. This is because neither of the elements (Pd or Sn) react with alumina crucibles and the growth does not require temperatures above 1200 °C. However, as described in [34] and [35], at low temperatures, such as those used here, Sn has a large enough surface tension as to require large holes in the separation frit for successful decanting. Therefore, we put an initial stoichiometry of Pd_2Sn_{98} into a CCS, and then sealed it into an amorphous silica tube under partial Ar atmosphere. Next, materials need to be heated up until they become a homogeneous liquid. Considering high melting temperature of Pd, we heated the elements up to 600 °C which is $\sim$ 300 °C higher than the liquidus line and stayed there for 5 hours to make sure all elements become a homogeneous, single phase, liquid. We then rapidly cooled to 325 °C, because no precipitation (ie. crystal growth) is expected above 325 °C. Then, we slowly cooled down to 245 °C over more than 100 hours, and then finally decanted using a centrifuge. [36] Note that we did not cool down all the way to room temperature, instead we stopped at 245 °C, which is above the solidifying temperature of Sn, and centrifuge the ampoule. This way the fritted alumina crucible [CCS] allowed us to cleanly separate the crystals from the excess Sn. The obtained crystals were rectangular shaped plates. Interestingly, the size of the single crystals varied a lot, depending on the form (powder or chunk) of Pd that we used for the growths. When we used the powder form of Pd, we obtained many small crystals of maximum $2\,\text{mm} \times 1\,\text{mm} \times 0.3\,\text{mm}$. On the other hand, crucible limited single crystals of $PdSn_4$ were obtained when we used the chunk form of Pd.

Single crystals of $PdSn_3$, $PdSn_2$ and PdSn can, in theory, be grown similar to the method as $PdSn_4$, although the initial stoichiometry as well as the temperature sequence would be different.

On the other hand, Pd_3Sn and Pd_2Sn requires some modification of the growth procedures. Firstly, the required temperature to grow Pd_3Sn is too high for fused silica tubes. This is because, SiO_2 glass begins to soften above 1200 °C. In addition, there is a greater risk of devitrification of fused silica. In order to avoid this issues, one might try to use an $in-situ$ decanting furnace system, [35] Bridgman growth method or other low melting elements as a solvent. Pd_2Sn on the other hand does not have an exposed liquidus line. In this case, one might try to use other growth methods, such as vapor transport, or other low melting elements as a solvent. In order to select the right solvent, one needs to check the solubility of the elements in the compound into the solvent. At the same time, the elements should not form the secondary phases with the solvent.

3.1.1 Te/Se Growth

The high vapor pressure of some elements can be an obstacle to doing high temperature solution growth. This is because the initial composition of the melt can be changed via evaporation or worse, the ampoule can explode in extreme cases due to vapor pressures in excess of 5-10 atm. A detailed study of how to work with sulfur [37] was carried out and paved the way to more common use of S-based melts. Both tellurium and selenium also have high vapor pressures (the boiling point of Te is 988 °C and Se is 685 °C). In addition, both elements are well known for their toxicity. As a result, fewer studies have been done on compounds containing these two elements compared to other elements. This implies that there are still a lot of unexplored properties associated with compounds containing these elements. In addition, quasi two dimensional materials with van der Waals bonding between layers recently gained lots of attention due to their potential use for applications; Te/Se commonly form van der Waals bonding networks and many compounds containing Te/Se have quasi two dimensional structures and easily exfoliate. For these reasons, Te/Se based compounds are a focus of this dissertation.

Although Te and Se based materials have great interest, experiments need to be conducted carefully. Firstly, understanding elements and being aware of their hazards is important. [38] Secondly, one needs to wear proper personal protecting gears (lab coat, gloves, mask and safty

glasses) when preparing growths. Thirdly, back-filling growth ampoules with a partial pressure of Ar is recommended due to high vapor pressure of Te/Se. Fourthly, it is better not to exceed the boiling temperature of both materials. However, higher temperature can be achievable depends on the solubility with other elements and the amount of Te/Se. Fifthly, decanting needs extra caution. This is because Te vapor (yellow color) presents in the ampoule instead of Te droplet above 600 °C. Therefore, there is some risk of inhaling the Te gas or generating Te powders if the ampoule breaks. The list of Te/Se growth attempts can be found later in appendix A. As examples, two growth projects (single crystal growth of $CrAuTe_4$ and WTe_2) will be discussed below.

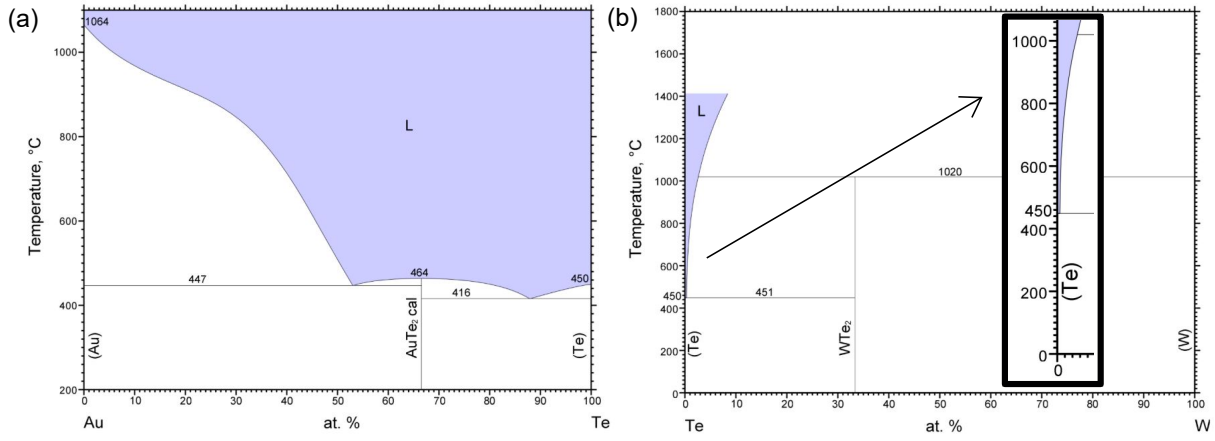

Figure 3.2 (a) Phase diagram of Au-Te from ASM alloy phase diagram. [33] (b) Phase diagram of W-Te from ASM alloy phase diagram. [33] Inset shows the enlarged left bottom conner of the phase diagram. Reprinted with permission of ASM International. All rights reserved. www.asminternational.org

The Au-Te binary phase diagram has very accessible, Te-rich low temperature liquid as shown in Fig. 3.2 (a). Owing to this high solubility of Au into Te, there are several benefits in terms of solution growth: (i) the high melting point element, Au, can be introduced in a compound, (ii) Te vapor pressure can be lowered, and (iii) other high melting temperature third elements can be introduced through Au-Te melts. By adopting these benefits, we grew single crystals of $CrAuTe_4$. We added small amounts of Cr into this Au-Te low temperature melts to grow the single crystals of $CrAuTe_4$. In particular, high purity elemental Cr, Au and Te were put into alumina crucible with initial stoichiometry, $Cr_2Au_{30}Te_{68}$, and sealed in an amorphous silica tube. [34, 36] The ampoules

were heated up to 900 °C over 5 hours, kept at 900 °C for 3 hours, rapidly cooled to 625 °C and then slowly cooled down to 500 °C, over 75 hours, and finally decanted using a centrifuge. [36] We obtained both blade-like $CrAuTe_4$ with typical dimensions of $5 \times 0.2 \times 0.1$ mm and platelike Cr_5Te_8. Identifying the two compounds was possible given their different morphologies as well as their different magnetic properties. Since Cr_5Te_8 is a ferromagnet, [39] even a small amount of Cr_5Te_8 could be detected by measuring the magnetic properties.

Another example of a Te based growth is the single crystal growth of WTe_2. Previously, single crystals of WTe_2 were grown via chemical vapor transport using halogens as transport agents. [9, 40] However, we grew WTe_2 single crystals from a Te-rich binary melt. This was possible because W has finite (albeit small) solubility into Te liquid. (see Fig. 3.2 (b)) To be more specific, high purity, elemental W and Te were placed in alumina crucibles in W_1Te_{99} and W_2Te_{98} ratios. The crucibles were sealed in amorphous silica tubes and the ampoules were heated to 1000 °C over 5 hours, held at 1000 °C for 10 hours, then slowly cooled to 460 °C over 100 hours, and finally decented using a centrifuge. The resulting crystals were blade- or ribbonlike in morphology with typical dimensions of $3 \times 0.5 \times 0.01$ mm with the crystallographic c axis being perpendicular to the larger crystal surface; the crystals are readily cleaved along this crystal surface. There were no significant differences between two different initial stoichiometries.

3.2 Characterization

Once single crystals are obtained, it is important to determine their crystal structure, composition and intrinsic physical properties. Here, I review the use of X-ray diffraction (XRD), magnetization, resistivity, specific heat and thermoelectric power (TEP) measurements.

3.2.1 X-ray diffraction

XRD measurements can provide data that allow for the determination of a sample's crystal structure. Once x-rays are incident on a crystal, the x-rays are diffracted with specific angles due to the periodic arrangement of atoms. To be more specific, the diffracted beams are found when

the reflections from parallel planes of atoms interfere constructively. This constructive interference condition can be described by Bragg's law: $2d\sin\theta = n\lambda$, where d is the spacing between the lattice planes, 2θ is the angle between incoming photon and outgoing photon, n is the integer multiplier and λ is photon wavelength. [41]

A Rigaku MiniFlex diffractometer (Cu-$K_{\alpha 1,2}$ radiation) was used for acquiring an XRD pattern at room temperature. Most of the specimens are prepared by grinding a single crystal and then spreading the ground powder on a thin layer of vacuum grease on a zero background sample holder, made out of single crystalline Si. A typical data acquisition profile was 0.02° step size with 1-3 seconds data collection time at each angle. The range was determined based on the expected continuous of peaks from the compound or generally $10^o \leq 2\theta \leq 80^o$. The obtained powder pattern was fitted with a Le Bail refinement. [42]

We also used single crystals with nice clean surfaces. By placing the surface parallel to sample holder, the orientation of single crystals could be determined out. [43] This is because diffraction peaks from the oriented single crystals arise from periodicity in only one crystallographic direction, which is perpendicular to the surface of the sample.

3.2.2 Magnetization

Magnetic measurements were performed in a Quantum Design (QD) magnetic property measurement system (MPMS) superconducting quantum interference device magnetometer over the temperature range of $1.8\,\mathrm{K} \leq T \leq 300\,\mathrm{K}$ with applied magnetic fields up to 70 kOe. A measurement can be done by moving a sample through the superconducting detection coils. As the sample moves, an electric current is induced in the detection coils by the magnetic moment of the sample. Note that any other discrepancy throughout the scan length can induce additional current in the detection coils, so the mounting procedure is very important. Samples were most commonly mounted using transparent plastic straws which are homogeneous throughout the scan length. Some of the possible ways of mounting are shown in Fig. 3.3.

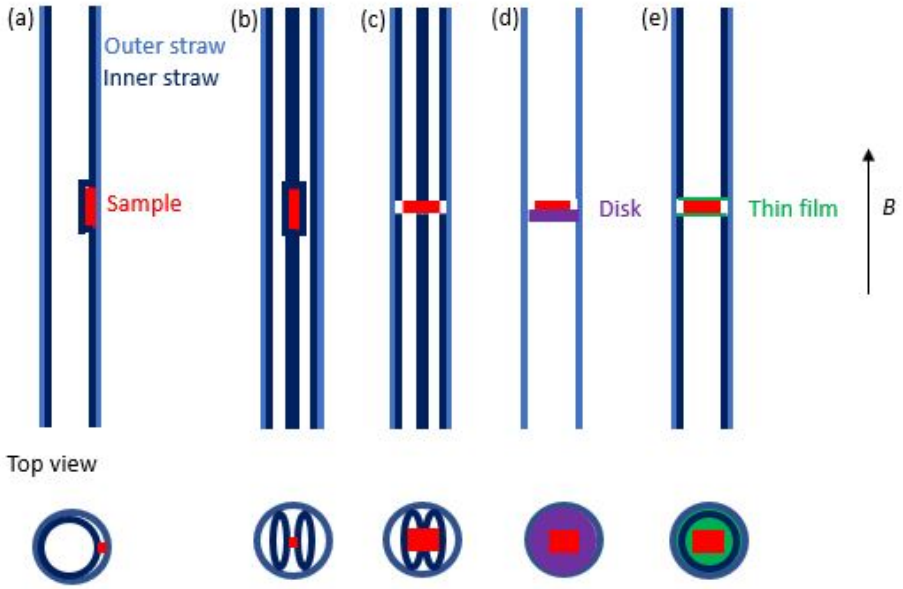

Figure 3.3 Various ways of mounting crystals for magnetization measurement. (a) Sample in between outer and inner straw. (b) Sample in between two inner straws. (c) Sample in between two straws in the bottom and two straws on the top. (d) Sample on the disk. (e) Sample in between two thin film.

The first way is mounting a sample in between outer and inner straw (Fig. 3.3 (a)). An advantage of this method is almost no background, because of the uniformity of the straws along the scan length. However, small errors come from the fact that the sample is slightly off-center, and does not match the location where the MPMS calibration sample ($\sim$200 mg Pd) is measured. The second mounting method (Fig. 3.3 (b)) is locating the sample between two inner straws and inserting all inside of an outer straw. It is better than the first method in terms of possible positional errors, since sample location is in the middle of the sample space. On the other hand, sample can experience more force than in the case of 3.3 (a), thus, it is not an appropriate mounting method for brittle or flexible samples. Both methods shown in Figs. 3.3 (a) and (b) are limited to having the applied field along the longer dimension of a plate or rod like sample.

In order to measure the anisotropic properties of plate or rod like samples, three other mounting methods, as shown in Fig. 3.3 (c), (d) and (e), were used. One method is mounting a sample between two inner straws on the bottom and two inner straws on the top, as shown in Fig. 3.3 (c).

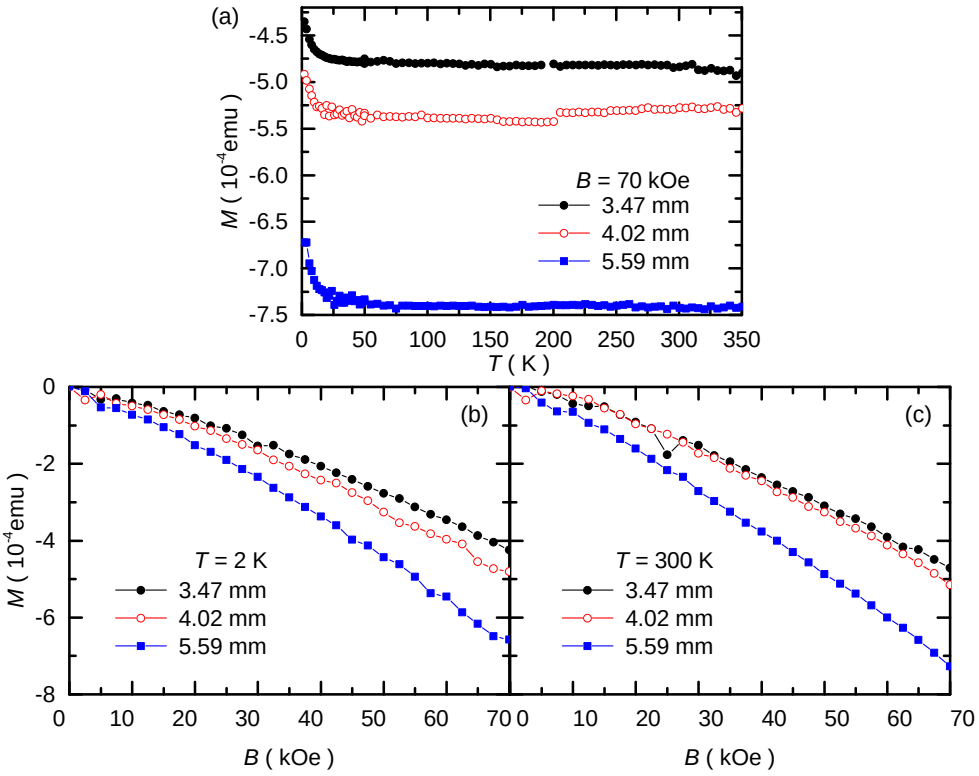

Figure 3.4 (a) Temperature dependent magnetization data of three different length of straws at $B = 70\,\mathrm{kOe}$. (b) Magnetic field dependent magnetization data of three different length of straws at $T = 2\,\mathrm{K}$. (c) Magnetic field dependent magnetization data of three different length of straws at $T = 300\,\mathrm{K}$.

A background still comes from the gap between upper and lower straws. However, the background signals are usually small compared to the sample because the thickness of a plate or rod like sample is usually tens or hundreds of μm. In order to understand how much background comes from the gap, magnetization measurements on three different length of straws were conducted (see Fig. 3.4). Based on the data, one can roughly estimate the background due to the gap. Note that the background from the gap should have opposite sign of magnetization of a straw. Another methods is gluing a sample on a PCTFE (Poly-Chloro-Tri-Fluoro-Ethylene) disk. This way one can get precise magnetization data by subtracting the background from the disk. Finally, we also tried mounting a sample between two thin films (press-and-seal wrap, the Glad Products Company), which have small diamagnetic signals. This was actually the worst mounting method among all

three, because of a background from both the films and also from the gap between the straws. Moreover, the films can bend easily, allowing the sample to locate in a tiled orientation, as opposed to perpendicular to the magnetic field direction.

3.2.3 Resistivity

Temperature- and field-dependent electrical transport measurements were carried out in a QD Physical Property Measurement System (PPMS) for $1.8\,\mathrm{K} \leq T \leq 305\,\mathrm{K}$ and $|H| \leq 140\,\mathrm{kOe}$ with the ac-resistivity ($f = 17\,\mathrm{Hz}$, $I =$ 1-3 mA) option. Four Pt or Au wires were attached to bar shaped single crystals using various methods, depending on the sample properties. Most of the time, Epotek-H20E silver epoxy (cure at 120 °C for about 20 mins) or DuPont 4929N silver paint (air dried for a couple of minutes) was used. For many of the Te based materials, neither silver epoxy nor silver paint gave a good contact resistance values (from $\sim 100\,\Omega$ to MΩs). Therefore, spot welding was used with Au wires (12.7 m diameter) or Au sputtering was done prior to attaching wires with silver epoxy or paint. To be more specific about Au sputtering, we first made a simple mask using aluminum foil, sputtered Au on top, took out the aluminum foil mask, and then put wires with silver epoxy or paint. This way we could have contact resistance values below $5\,\Omega$.

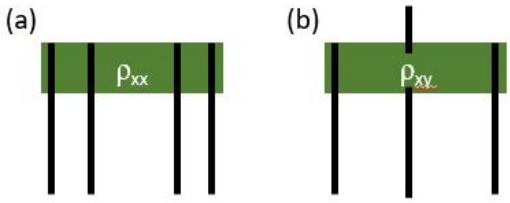

Figure 3.5 (a) 4 probe contacts for ρ_{xx} measurement (b) 4 probe contacts for ρ_{xy} measurement

Both ρ_{xx} and ρ_{xy} were measured with four wires on the sample, although the configuration were different as shown in Fig. 3.5. For ρ_{xx}, all four wires (2 current wires at the end and 2 voltage wires in the middle) were parallel. (see Fig. 3.5 (a)) For ρ_{xy}, two current wires were on the edge and two voltage wires were aligned at the middle of the sample. (see Fig. 3.5 (b)) In the case of ρ_{xy}, it is very hard to align the voltage wires perfectly, so the measured resistivity is almost always a combination

of ρ_{xy} and ρ_{xx}. Therefore, we measured both magnetic field directions and then corrected by subtracting the resistance values measured in negative magnetic field from the resistance values measured in positive magnetic field ($\rho_{xy} = (\rho_{positive\,magnetic\,field} - \rho_{negative\,magnetic\,field})/2$). This was possible because ρ_{xx} is symmetric and ρ_{xy} is anti-symmetric as a function of the applied magnetic field.

3.2.4 Specific heat

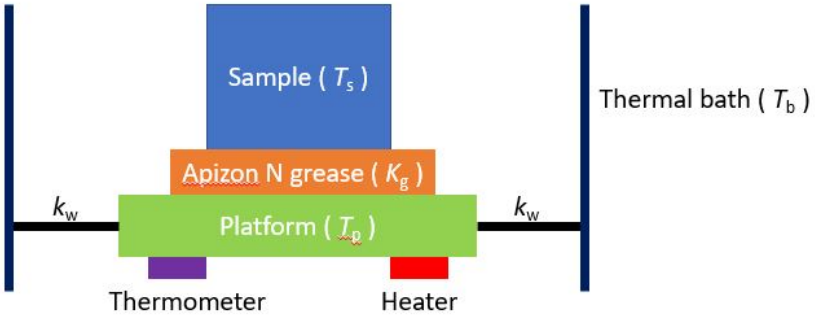

Figure 3.6 Schematics of the specific heat measurement

Temperature dependent specific heat measurements ($2\,\mathrm{K} \leq T \leq 200\,\mathrm{K}$) were performed in a QD PPMS using a relaxation method. [44] Prior to attaching sample on the addenda, we measured addenda and grease over T and H ranges that we used for the sample measurement. The relaxation method determines heat capacity values by fitting the thermal response of a system after it experiences a heat pulse of a known size. In particular, the following equations describes the two-tau model:

$$P(t) = C_{platform}\frac{dT_p}{dt} + K_w(T_p(t) - T_b) - K_g(T_s(t) - T_p(t)) \tag{3.1}$$

$$0 = C_{sample}\frac{dT_s}{dt} + K_g(T_s(t) - T_p(t)) \tag{3.2}$$

where $C_{platform}$ and C_{sample} are specific heat of the sample platform and the sample, K_w and K_g are thermal conductance of the supporting wires and the grease, T_b, T_p and T_s are temperature of the thermal base, platform and sample, and P is power. (see Fig. 3.6) The solution of these

equations are proportional to exponential $e^{-t/\tau}$. Here, two τ values are used; τ_1 for the relaxation between thermal bath and the platform and τ_2 for the relaxation between sample and the platform.

3.2.5 Thermoelectric power

TEP measurements were performed by a dc alternating temperature gradient technique [45] using QD PPMS over the temperature range of $2\,\mathrm{K} \leq T \leq 300\,\mathrm{K}$ and the magnetic field up to 140 kOe. Samples were picked or shaped in a bar shape with dimension of $l \sim 3\,\mathrm{mm}$, $w \sim 0.2\,\mathrm{mm}$ and $t \leq 0.1\,\mathrm{mm}$. Especially, in the case of WTe_2 we used as grown crystal because morphology of the crystal was already very thin bar which fufills requirements for TEP measurement. Ends of a prepare sample were attached to the two Cernox thermometers using DuPont 4929N silver paint, cured overnight at room temperature and made sure no crack as suggested by Ref. [46].

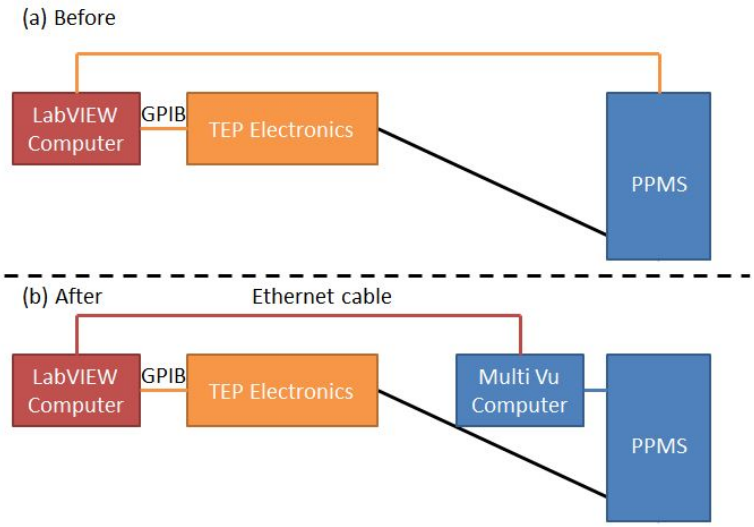

Figure 3.7 (a) System controlled solely by LabVIEW program, (b) System controlled by both LabVIEW and Multi Vu programs

Previously, both TEP electronics and QD PPMS hardware were controlled directly by a LabVIEW program (Fig. 3.7). Therefore, several advantages of Multi Vu program for PPMS including safeguarding were not available while measuring TEP. In order to improve the issue, we separated the controlling system; LabVIEW program to control TEP electronics and Multi Vu program to

control PPMS systems, and then connected these two programs using Ethernet cable with QDInstrument sub VIs (detailed information can be found in QD application note 1070-210). After implementing such programs, we did Pt reference measurements and confirmed the TEP system.

3.3 Resistance under uniaxial strain

Although it is important to characterize the properties of novel materials at ambient pressure or strain, the response of a material to strain is also a great interest. This is because strain can be a powerful tool for tunning the structural and thereby electronic and magnetic, properties of novel materials. In general, strain can change the lattice parameters of single crystals and thereby change the band structure (the size of those changes varies depending on the material). Furthermore, larger impacts can be expected from strain by breaking certain symmetries of single crystals. For example, four fold symmetry of cubic or tetragonal crystal structure can be broken by applying uniaxial strain along the crystallographic a direction.

3.3.1 Razorbill uniaxial strain cell

Razorbill uniaxial strain cell [Instruments] is made out of Ti, with one inner and two outer piezoelectric stacks and a capacitance sensor. Figure 3.8 shows working principle of the cell. A sample is mounted at the unstrained position of the cell. By applying positive (negative) voltage differences across the outer (inner) piezoelectric stacks, a strain can be applied to the sample. For example, one can apply positive strain (tension) by extending the outer piezo stacks and retracting the inner piezo stack as shown in the middle picture of Fig. 3.8. While, negative strain (compression) can be applied to the mounted sample by retracting the outer stacks and extending the inner stack. (the last picture of the Fig. 3.8)

3.3.2 Probe for the strain cell

Figure 3.9 (a) shows a QD PPMS Multi-function probe (MFP) modified for use with a Razorbill strain cell. A top head plate made out of aluminum was replaced with plastic one with two holes

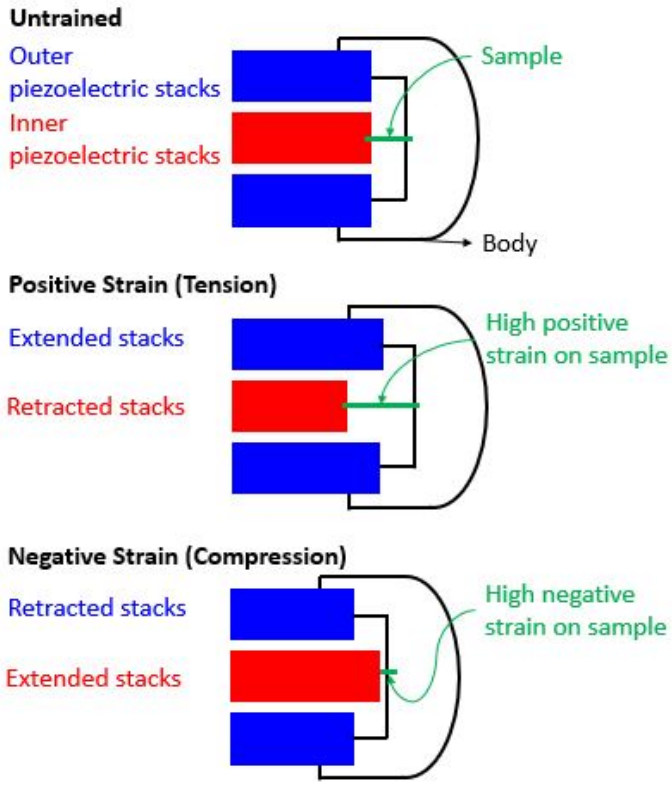

Figure 3.8 Razorbill uniaxial strain cell in three different configurations; unstrained, positive strained and negative strained based on Ref. [Instruments].

(3/8 drill bit) in the middle. (see Fig. 3.9 (b)) Two BNC female hermetically sealed connectors (Pasternack, part number: PE4077) were fed through these two holes to allow for connection to the capacitance sensor. Four holes for voltage wires to control the piezoelectric stack were drilled (3/8 drill bit) on the side of a top head body, and same BNC connectors were attached. (see Fig. 3.9 (b)) By using only the middle wire of the BNC connector, voltage wires are isolated from the system. In order to achieve mechanical strength and improve vacuum seal of the connecting part between the connector and the head, we put small amount of Stycast 2850 FT on sides of the BNC connectors.

Low thermal conductivity wires were used to provide a degree of thermal insulation between the top of the probe (room temperature) and the bottom of the probe (1.8 K minimum). To be more specific, the Lake Shore stainless coax cable (part number: CC-SS-50) was used for the capacitance sensor and the Lake Shore phosphor bronze wire (part number: WQT-36-100) was used for the

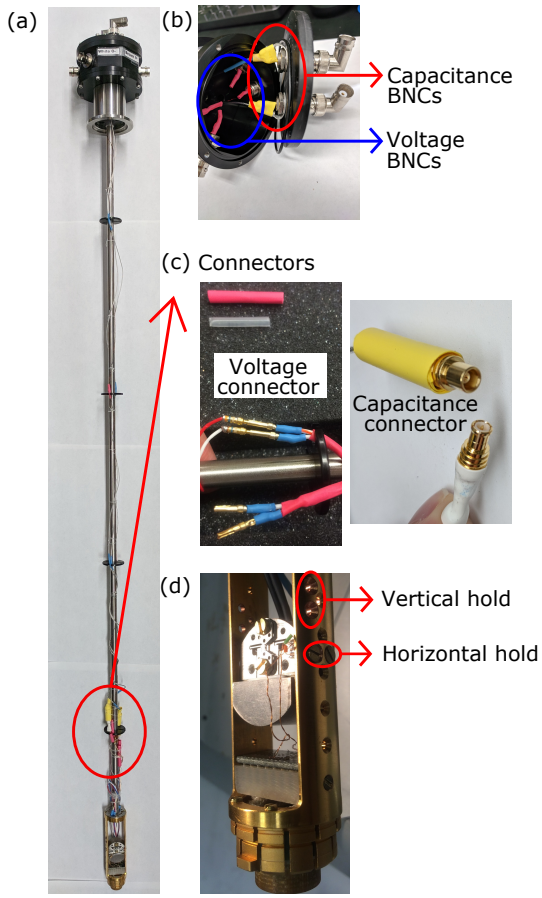

Figure 3.9 (a) Entire probe for the strain cell. (b) Top head of the probe with side four voltage BNCs and top two capcitance BNCs. (c) Four voltage connectors and two capacitance connectors. (d) Bottom of the probe. Showing vertical and horizontal holes to hold the cell and wiring for resistance measurements.

voltage sources. At the bottom end of each wire, we put a connector to facilitate mounting and demounting cells as shown in Fig. 3.9 (c). For resistance measurements of a sample, insulated Cu wires are run from the electrical pad on the strain cell to the sample socket connected to the pins on the bottom of PPMS. Similarly, an extra thermometer (Cernox thin film RTD, CX-1030-Sd-HT, Serial number: X121805) was also attached through the bottom socket. There are two reasons that we use an extra thermometer on the strain cell probe. One is large thermal mass of the strain cell, so it takes certain time to stabilize the temperature. The other is that the location of the cell is slightly above the bottom of the PPMS. The PPMS cooling system can be controlled via exchange

gas and the bottom thermal connection. Therefore, one can lose fine control of temperature by being away from the bottom of the PPMS. In general, we measured a temperature difference of $T_{diff,avg} = 1.67\,\mathrm{K}$ (the temperature difference gets smaller upon cooling, $T_{diff\,at\,2\,K} \leq 0.01\,\mathrm{K}$) between our extra cernox thermometer and the PPMS thermometer with the $1\,\mathrm{K/min}$ sweep rate.

Eight holes were made at the bottom of the MFP probe to hold the Razorbill cell. (See Fig. 3.9 (d)) Four horizontal holes (two in one side and the other two in another side) hold the cell vertically so that one can apply the magnetic field in an "in-plane direction" of a plate like sample. Additionally, four vertical holes hold the cell horizontally so that the magnetic field can be applied in an "out-of-plane direction" of a plate like sample.

3.3.3 Mounting a crystal

Prior to mounting a sample on the strain cell, the sample needs to be picked and shaped correspondingly. Typical sample dimension suggested by the Ref. [Instruments] is $l = 2\,\mathrm{mm} \times w = 0.4\,\mathrm{mm} \times t = 0.2\,\mathrm{mm}$. Length limit is in between 1.2 mm and 2.5 mm. Other than length, one of the most important parameter that one need to keep in mind before mounting the sample is the spring constant of the sample (upper limit of $5 \times 10^6\,\mathrm{N/m}$). This is because if the stiffness of the sample is above the upper limit, it can substantially limit the displacement that the strain cell can apply.

The mounting procedures are well explained in the separate sheets of paper that the company provide with the cell.[Ref. [Instruments]] Here, some missing details are given for future users. The first step of the mounting sample on the Razorbill strain cell is put the bottom two plates in a position. One can use a guide (shown in Fig. 3.10 (a) left) to assist the procedure. The two plates should be parallel and the gap between the two should be adjusted based on the sample length. Very light addition of GE Varnish between the plates and the cell can help the mounting procedure.

After fixing the bottom plate, we added small amount of glue on the edge of the plates as shown in the Fig. 3.10 (b). Here, the glue should have the right volume and texture. Small enough to increase the transmitted strain to the sample and not overflow through the edge of the plates, but

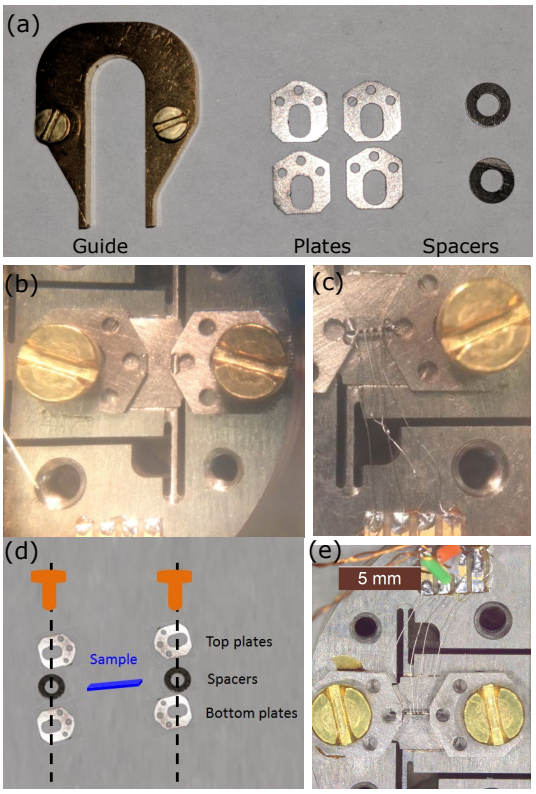

Figure 3.10 (a) Mounting tools; guide, plates and spacer. (from left to right) (b) Locate plates in line, and then put a bit of glue on the edge of the plates. (c) Place a crystal on top of the glue and put another layer of glue on top of the crystal. (d) Schematic drawings of full assmbly. (e) Place the spacers and top plates, and then tight the golden screws to hold them all together.

large enough to electrically isolate the cell from the sample. Texture wise, it should be viscous enougth that the sample does not sink through the glue, but it also should not be so solid that it does not actually hold a sample well. The glue can be Devcon 5 minute epoxy, Devcon 2 ton epoxy or Stycast 2850 FT. (Use $T \leq 270\,\mathrm{K}$) The type of glue may not the biggest component to determine the transmitted strain on the sample. [47] Thickness and width of sample and the thickness of glue are more crucial components to determine the transmitted strain on the sample. Place the sample with four wires gently on top of the glue and then wait a day for it to solidify. The contacts for the electrical transport measurement were prepared in a standard linear four-probe configuration using Epotek-H20E silver epoxy and silver paint.

Once glue is cured, the wires from the sample can be soldered onto the electrical pad on the cell. Note that the sample has to be electrically isolated from the cell using the proper amount and thickness of glue on top of the sample. Align spacers, top plates and golden screws that can match with the bottom plates. Here, the spacers need to be polished using sand paper to have same height, as sample and glue. Tighten up the screws well so that all the mounting components are secured. Then, another day is need to for the glue to cure.

3.3.4 Electronic connections

Figure 3.11 shows a schematic diagram and a real picture of the measurement system. The outer and inner piezoelectric stacks were controlled by two Keithley Model 2400 source meters, and corresponding length changes of the sample were measured by capacitance sensor using an Andeen-Hagerling(AH) Model 2550A capacitance bridge. Note that there are always certain errors in the length change measurements due to thermal contraction of different parts of the cell. Although some thermal effects were fixed (i.e. the thermal effect from piezoelectric materials was canceled via symmetric usage of outer and inner piezoelectric stacks, and the thermal effect from the capacitance sensor was corrected by subtracting the temperature dependent capacitance of the empty cell), others, including the thermal contraction from the cell and the crystal itself, were not considered.

Two Lake Shore Model 370 AC resistance bridges were used, one each for the resistance measurement of the crystals and the Cernox thermometer. Due to the limit of the resistance bridge (resolution is $1\,\mu\Omega$ with $I = 3.16\,\mathrm{mA}$ in the range of $2.0\,\mathrm{m}\Omega$), we were not able to carry out elastoresistance measurements below $50\,\mathrm{K}$ with $H = 0\,\mathrm{T}$ in the above experimental setting for WTe_2 and $PtSn_4$ which have high residual restivity ratios (RRR) of close to 1000. In order to overcome this measurement limit, we performed the zero field elastoresistance experiment using a Stanford Research Systems(SRS) 860, Lock-In Amplifier and SRS Model CS580, voltage controlled current source in a Janis SHI-950-T closed cycle cryostat.

Similar to the TEP setup (see 3.2.5), both Multi Vu and LabVIEW programs were used to control the strain system.

3.3.5 Empty cell measurements

We have two Razorbill cells; CS100 and CS130. While the working principle of the two cells is the same, the difference between two cells is the size of the piezo electric stacks which gives different displacements. It is important to understand the empty Razorbill cell behavior prior to attaching a sample to the cell for strain measurements. First of all, voltage sweeps of the empty cell at various temperatures, as shown in Fig. 3.12 (a) and (c), need to be performed in order to determine how "healthy" the cell is and what the maximum length changes of the cell are at various temperature. To be more specific, if the hysteresis loops are not symmetric, it means the cell is broken. In addition, two factors which have opposite effects determine the maximum length changes of the cell. One is that the maximum voltage which can be applied to the inner and outer piezo stacks, varies with temperature due to dielectric breakdown and de-poling of the piezoelectric stacks. The other is that the displacement achieved for a given applied voltage drops as the temperature decreases. (At high temperatures, the domain boundaries move more compared to low temperature.) The difference in maximum length changes between the CS100 (Fig. 3.12 (a), $L_{max} \sim \pm 7.5\,\mu$m around $T \sim 130\,$K) and the CS130 (Fig. 3.12 (c), $L_{max} \sim \pm 30\,\mu$m around $T \sim 130\,$K) is due to the size of piezoelectric stacks.

As explained earlier in Subsection 3.3.4, thermal expansion effects came from many sources. One of them originates from the differential thermal expansion of the materials used for the capacitance sensor. This has nothing to do with length changes in the mounted sample, but is an artifact solely from the capacitance measurements. By subtracting the temperature dependent displacement of the empty cell (Fig. 3.12 (b) and (d)), this artifact from the capacitance sensor can taken into account.

He gas is another source of error in displacement measurement. Changes of displacement are calculated by changes in capacitance using an equation, $C = \epsilon A/(d+d_0)+0.25\,$pF, where A and d_0 is given by manufacturer. Here, the problem is dielectric constant, ϵ. We used vacuum permittivity, ϵ_0, for ϵ to calculate the displacement. However, $\sim 4\,$Torr (at $T = 300\,$K) of He exchange gas was present during the measurement. Therefore, we conducted a capacitance measurement of empty cell

at $T = 300\,\mathrm{K}$ while switching mode from high vacuum ($\sim 10^{-4}\,\mathrm{Torr}$) to vent continuous ($\sim 760\,\mathrm{Torr}$). The changes were $d = 0.03\,\mu\mathrm{m}$. Since we used only $4\,\mathrm{Torr}$ at $300\,\mathrm{K}$, the expected displacement error due to the presense of the He exchange gas is rather small compared to the actual displacement triggered by the piezo stacks. In addition, the elastoresistance value is not affected by this effect because, by definition, elastoresistance is the first derivative of resistance versus strain.

Another capacitance measurement was conducted while ramping the magnetic field to determine the effect of the magnetic field. The results show that the capacitance value is more or less constant in the magnetic field range of $0 \leq H \leq 140\,\mathrm{kOe}$. When the magnetic field was ramped at the rate of $100\,\mathrm{Oe/min}$ ($20\,\mathrm{Oe/min}$), the fluctuations were $\leq 0.002\,\mu\mathrm{m}$ ($\leq 0.001\,\mu\mathrm{m}$). The fluctuation level was inversely proportional to the magnetic field ramping rate. This said, neither ramping rates cause any significant changes in the measured displacement.

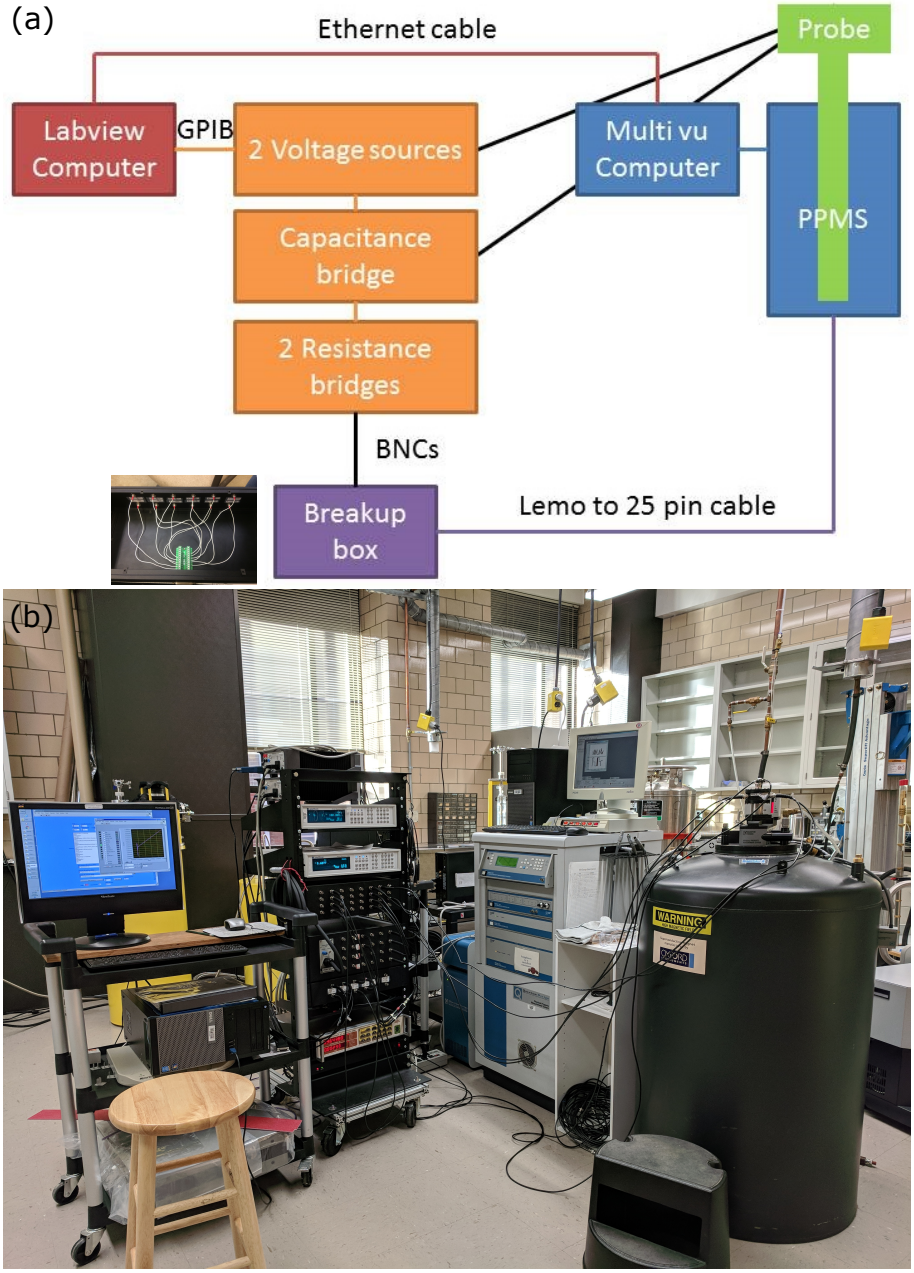

Figure 3.11 (a) Schematic diagram of connections. (b) Picture of measurement system.

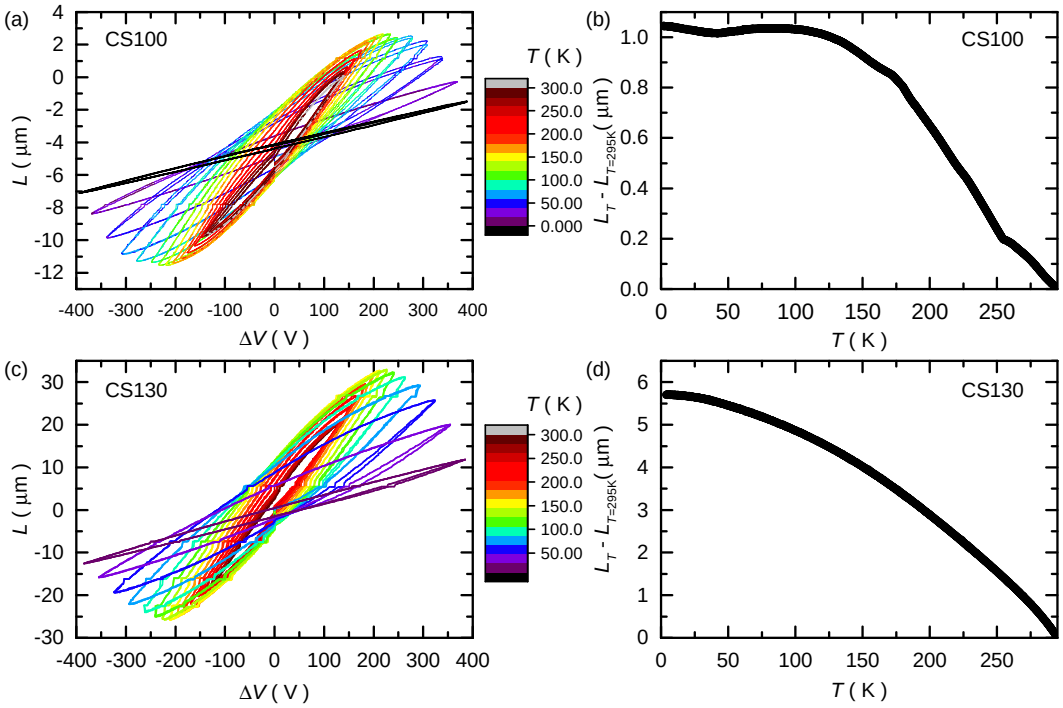

Figure 3.12 (a) Voltage sweeps of CS100 at various fixed temperature. Temperatures are marked with difference colors, rainbow scale; red for 300 K and purple for base temperature. (b) Temperature sweep of CS100 at $V = = 0$ V. (c) Voltage sweeps of CS130 with various temperature. Temperatures are marked with difference colors, rainbow scale; red for 300 K and purple for base temperature. (d) Temperature sweep of CS130 at $V = = 0$ V.

CHAPTER 4. ANISOTROPIC PHYSICAL PROPERTIES AND PRESSURE DEPENDENT MAGNETIC ORDERING OF $CrAuTe_4$

The following context is a slightly modified version of the published work in Ref. [48]. DOI: http://dx.doi.org/10.1103/PhysRevB.94.184413. Reprinted (abstract/excerpt/figure) with permission from [N. H. Jo *et. al.*, Phys. Rev. B 94, 184413 (2016)] Copyright (2016) by the American Physical Society.

Transition metal based antiferromagnetism (AFM) can be considered to be a necessary, but clearly not sufficient, ingredient for high temperature superconductivity in both the CuO- and Fe-based superconductors. When long-range AFM can be suppressed by either substitution or pressure in these systems superconductivity emerges, often with remarkably high transition temperatures and upper critical fields. One proposed route to the discovery of new high-Tc superconductors is through the study of other transition metal based antiferromagnets, specifically their response to pressure. [49] Many studies have been done on Cr based AFM materials not only at ambient pressure but also under pressure. Pure, elemental Cr showed rapid decrease of T_{N} as pressure was applied. [50, 51, 52] V doped Cr also showed a substantial decrease in T_{N}, [53] and several studies examined the effects of pressure on V doped Cr to see quantum criticality. [54, 55, 56] More recently, pressure studies on CrAs, which has $T_N = 265\,\mathrm{K}$ at ambient pressure, demonstrate complete suppression of AFM, and even a superconducting transition around 2 K at the critical pressure of 8 kbar. [57] All of these pressure studies are important, because new physics around the quantum critical point can be studied. [58]

$CrAuTe_4$ was reported to crystallize in a monoclinic space group ($P2/m$) with lattice parameters $a = 5.4774(7)\,\mathring{A}$, $b = 4.0169(6)\,\mathring{A}$, $c = 7.3692(13)\,\mathring{A}$ and $\beta = 90.604(10)\,^{\circ}$, [59] and it has a layered structure. The layered structure is composed of slabs made up of a central Cr-Au plane capped on each side by a Te layer. These 3 layer slabs are then stacked along the crystallographic a axis

with van der Waals bonding between Te atoms. (see Fig. 4.1 (a) inset) It has only one Cr site with monoclinic centrosymmetric point symmetry (2/m), and it reported AFM ordering temperature was below 255 K. [59] Previous studies were done on polycrystalline samples and only at ambient pressure.

In this chapter, the physical properties of single crystal $CrAuTe_4$ at ambient pressure as well as temperature and field dependent resistivity for pressures up to 5.22 GPa will be presented. We find that $CrAuTe_4$ orders antiferromagnetically with $T_N = 255$ K at ambient pressure, with the ordered moments along the crystallographic c-axis. Angle resolved photoemission spectroscopy (ARPES) data show that there is a clear reconstruction of the Fermi Surface associated with the magentic ordering and pressure dependent resistivity measurements show that the ordering temperature can be suppressed to 236 K by 5.22 GPa. In addition to the suppression of the antiferromagnetic ordering temperature we are able to infer that for $P \sim 2$ GPa there is an additional, pressure induced phase transition that leads to clear changes in the temperature and field dependent resistivity.

4.1 Single crystal growth and XRD

Single crystals of $CrAuTe_4$ were grown by adding small amount of Cr to the low temperature Au-Te eutectic. [33] Growth detail can be found in the Methods chapter, subsection 3.1.1.

The powder data were fit with a Le Bail refinement (Fig. 4.1 (a)). Lattice parameters obtained from this refinement were a=5.49$\AA$, b=4.02$\AA$, c=7.37$\AA$, and the angles α=90°, β=90.64°, γ=90° in agreement with reported values. [59]. The orientation of the crystal was determined by single crystal XRD. [43] When the largest surface of the crystal was exposed to XRD, only (h 0 0) peaks, where h is integer number, were detected (Fig. 4.1 (b)). After confirming the a-axis direction, we rotated the sample almost 90° (β=90.64°) and measured XRD again to confirm the c-axis direction; in this case, only (0 0 l) peaks were detected (Fig. 4.1 (c)). By elimination, the long axis of the crystal is the crystallographic b-axis.

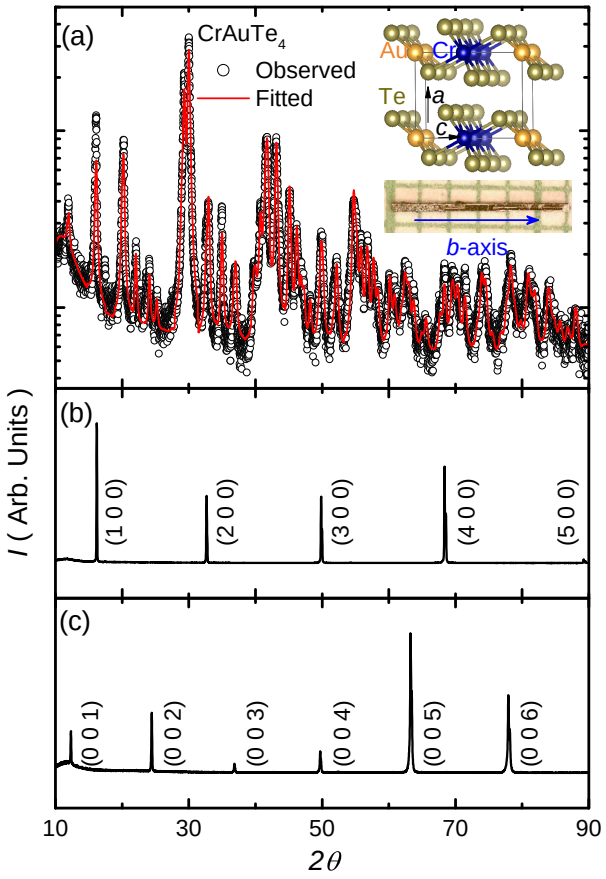

Figure 4.1 (a) Observed and fitted powder x-ray diffraction (XRD) pattern of $CrAuTe_4$ shown on a semi-log plot. Inset schematic drawing shows crystal structure of $CrAuTe_4$.Inset picture is typical $CrAuTe_4$ single crystal with the b-axis as the longest edge. (b) Single crystal XRD along the a-axis. (c) Single crystal XRD along the c-axis.

4.2 Magnetization

In Fig. 4.2 (a), magnetic susceptibility as a function of temperature, $M(T)/H$, measured in $H = 10\,\mathrm{kOe}$ shows the AFM transition just above 250 K. Because we mounted sample with diamagnetic thin film (see Fig. 3.3 (c)), the magnetic susceptibility data for $H \parallel$ a and $H \parallel$ c have a diamagnetic background, which is a likely cause for the differences above T_N. In addition, no anisotropy is expected in the paramagnetic state of Cr^{3+} in octahedron environment with $S = 3/2$ considering the crystalline electric field effect. Therefore, the $H \parallel$ a and $H \parallel$ c susceptibilities have been additively

shifted to overlap the high temperature $H \parallel$ b data (the sample was mounted between two long straws for $H \parallel$ b. see Fig. 3.3 (b)) in Fig. 4.2 (b).

Magnetic susceptibility data below 250 K (in the antiferromagnetically ordered state) are highly anisotropic with the ratio of the magnetization data for $H \parallel$ c and $H \perp$ c being $\sim$10 at around 100 K. We were not able to take the data below 100 K for $H \parallel$ c, because magnetization of our single crystal dropped below $\sim 10^{-6}$ emu which is below the MPMS sensitivity. Simple visual inspection of the anisotropic data suggests that the ordered Cr moments are along the c-axis. [41]

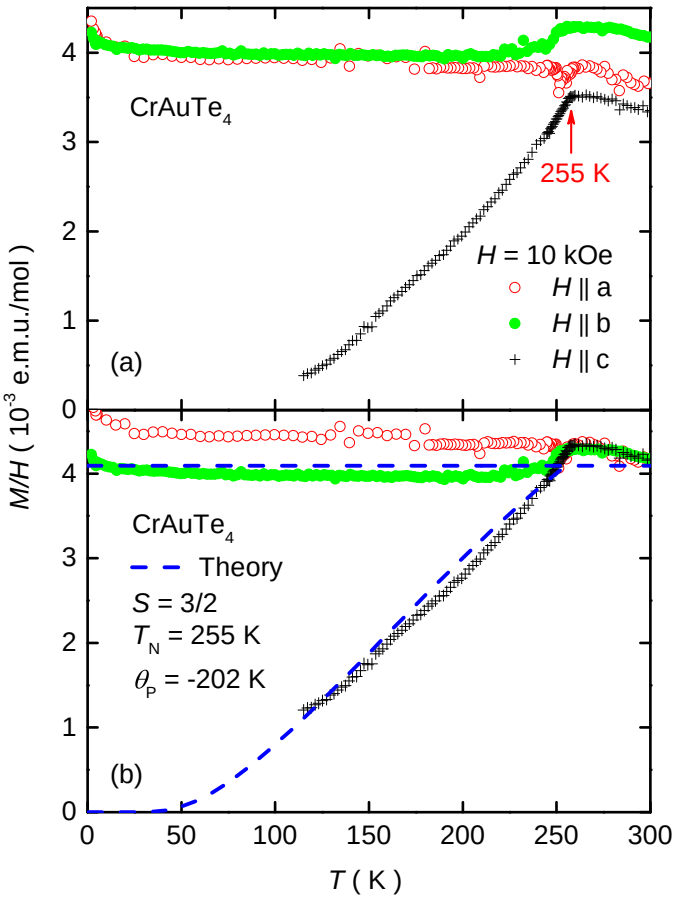

Figure 4.2 (a) Anisotropic magnetization data along three different directions. Black cross represents the magnetization when $H \parallel$ c, green filled dot corresponds to $H \parallel$ b magnetization, and red open dot is the magnetiztion with $H \parallel$ a. (b) anisotropic magnetization data with $H \parallel$ a and $H \parallel$ c data shifted additively to compensate for small addenda contribution (see text). Dashed lines are from a MFT result (see text).

More quantitatively, the anisotropic, temperature dependent magnetic susceptibility of AFM systems can be analyzed within the context of mean field theory (MFT). [60, 61] The magnetic susceptibility with H perpendicular to the ordered magnetic moment below $T_{\rm N}$ can be described by MFT.

$$\frac{\chi_{\perp}(T \leq T_{\rm N})T_{\rm N}}{C} = \frac{1}{1-\theta_{\rm P}/T_{\rm N}} \tag{4.1}$$

where $\theta_{\rm P}$ is the paramagnetic Weiss temperature and,

$$C = 2[S(S+1)]^{1/2} \tag{4.2}$$

Based on previous magnetization data on polycrystalline $CrAuTe_4$, [59] Cr is known to be trivalent. Cr^{3+} has $S = 3/2$ and the corresponding C was calculated by using $C = 2[S(S+1)]^{1/2}$. We used $T_N = 255$ K which is determined from both our magnetization and resistivity data (see below). The only free parameter that has to be determined is $\theta_{\rm P}$. By matching the theoretical prediction and the magnetic susceptibility data for $H \parallel$ b, which has almost no background, we find $\theta_{\rm P}$ = -202 K.

From this value, the magnetic susceptibility with field along the easy axis, $H \parallel c$, of collinear antiferromagnet below T_N can be calculated without any free parameters:

$$\frac{\chi_{\parallel}(T)}{\chi(T_{\rm N})} = \frac{1-\theta_{\rm P}/T_{\rm N}}{\tau^{*}-\theta_{\rm P}/T_{\rm N}} \tag{4.3}$$

where

$$\tau^{*}(t) = \frac{(S+1)t}{3B_{S}^{'}(y_0)} \tag{4.4}$$

In the function $\tau^{*}(t)$, t and $B_{S}^{'}(y_0)$ are

$$t \equiv \frac{T}{T_{\rm N}}, \quad B_{S}^{'}(y_0) = [dB_S(y)/dy]|_{y=y_0} \tag{4.5}$$

where $B_S(y)$ is unconventional Brillouin function which is defined as

$$B_S(y) = \frac{1}{2S}\left\{(2S+1)coth[(2S+1)\frac{y}{2}] - coth\left(\frac{y}{2}\right)\right\} \tag{4.6}$$

and $y_0 = \frac{3\overline{\mu_0}}{(S+1)t}$. $\overline{\mu_0}$ can be calculated numerically by graphical method from $\overline{\mu_0} = B_S(y_0)$. The calculated behavior, based on MFT, is shown in Fig. 4.2 (b) with dashed blue lines. The MFT calculated anisotropic susceptibility is consistent with the experimental data.

4.3 Resistivity

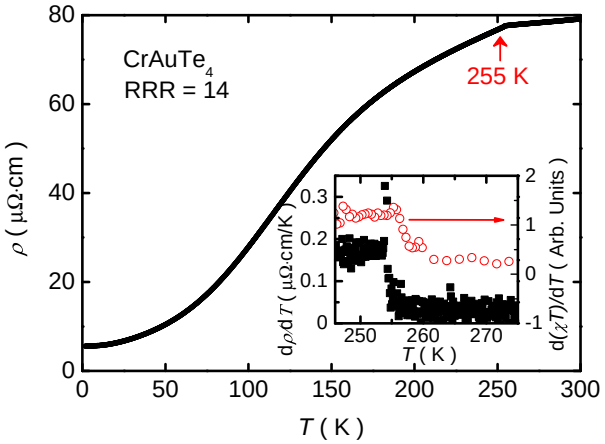

Figure 4.3 Zero-field, temperature dependent resistivity $\rho(T)$ of $CrAuTe_4$. Filled black squares show derivative of $\rho(T)$ with respect to temperature and open red circles represent the $d(\chi T)/dT$. Both show a clear peak near 255 K.

Samples for transport measurement were prepared by attaching four Au wires (12.7 μm diameter) via spot welding. The contact resistance values were all around 1 Ω. Prior to spot welding, we tried to use silver epoxy but the contact resistance was above 1 kΩ. Since silver paint itself cannot give rigid enough contacts between the sample and the wires for pressure experiments, spot welding was used.

The electrical resistivity, $\rho(T)$, of $CrAuTe_4$ was measured from 1.8 K to 305 K. A kink, where an abrupt slope change occurs, is found at T_N, in Fig. 4.3. The residual resistivity ratio (RRR) determined by $\rho(300\,\mathrm{K})/\rho(2\,\mathrm{K})$ of the sample is 13 with $\rho_0 = 5.57\,\mu\Omega\cdot\mathrm{cm}$. The low residual resistivity and high RRR demonstrate the good quality of the single crystal. In order to evaluate the transition temperature from different measurements, we used Fisher's arguments of singular behavior near an AFM transition transition. [62, 63] It is expected that the anomaly shown in specific heat due to AFM material is similar to anomaly in $d(\chi T)/dT$, [62] and that the resistivity anomaly, $d\rho/dT$, due to short-range fluctuation near transition temperature exhibits similar feature as specific heat. [63] We calculated $d(\chi T)/dT$ and $d\rho/dT$ as shown in Fig. 4.3 inset. Both $d(\chi T)/dT$ and $d\rho/dT$ show step like features just above and just below 255 K (respectively), giving $T_N = 255\,\mathrm{K} \pm 1\,\mathrm{K}$.

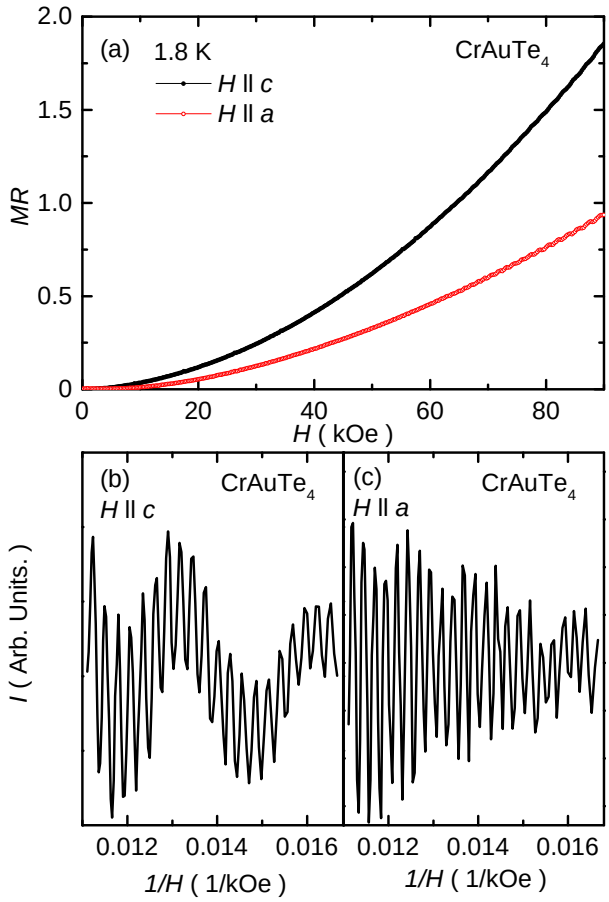

Figure 4.4 (a) Magnetoresistance (MR = $\rho(H)/\rho(H=0)$) of $CrAuTe_4$ at 1.8 K for two different field directions. (b) and (c), Shubnikov-de Haas oscillations after subtracting a second order polynomial background. (b) magnetic field along the c direction. (c) magnetic field along the a direction.

The field dependent resistivity was measured up to 90 kOe at 1.8 K along two different directions of applied magnetic field (Fig. 4.4). When the field direction is $H \parallel$ c, the magnetoresistance (MR = ($\rho(H)$-$\rho(H=0)$)/$\rho(H=0)$) for $T = 1.8$ K is 1.85 at 90 kOe. On the other hand, MR is 0.94 at 90 kOe for $H \parallel$ a. In the high field regime, Shubnikov de Haas (SdH) oscillations become increasingly apparent. We subtract the background by using second order polynomial function and plot the obtained oscillatory part of MR as a function of $1/H$ in Fig. 4.4 (b) and (c). Two distinct frequencies are found for $H \parallel$ c. On the other hand, a beat-like feature, due to two adjacent frequencies, is detected for $H \parallel a$.

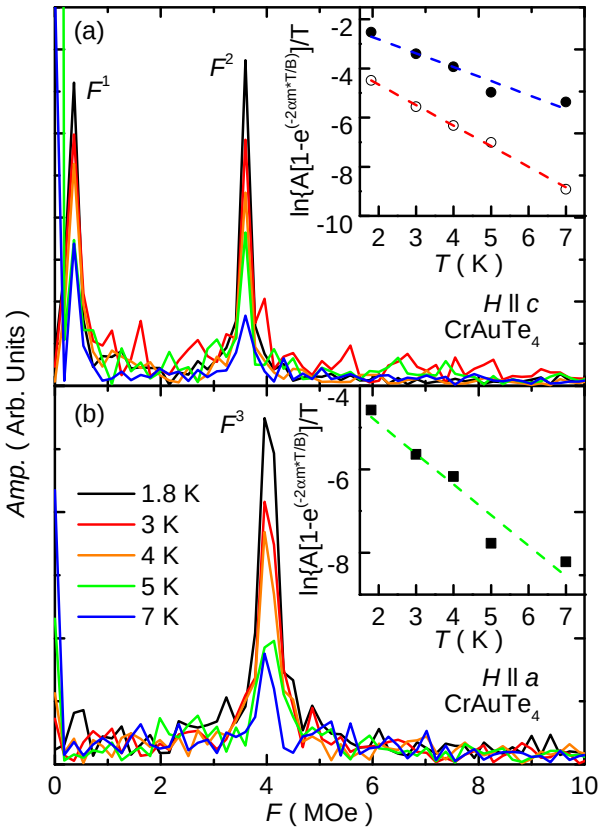

Figure 4.5 (a) Fast Fourier Transform (FFT) analysis of quantum oscillation data for $T = 1.8\,\mathrm{K}$, $3\,\mathrm{K}$, $4\,\mathrm{K}$, $5\,\mathrm{K}$ and $7\,\mathrm{K}$ when magnetic field is applied along the c-axis. Inset is the mass plot. The closed circle is the data from F^1 and open square is the data from F^2. (b) Same as (a) except the magnetic field direction on the crystal was along the a-axis.

We use a Fast Fourier Transform (FFT) algorithm to compare the quantum oscillation for the two directions of applied field. (Fig. 4.5) The FFT result for $H \parallel c$ shows two sharp peak; $F^1 = 0.36\,\mathrm{MOe}$ and $F^2 = 3.6\,\mathrm{MOe}$. At first glance only one frequecy is found from $H \parallel a$: $F^3 = 3.9\,\mathrm{MOe}$, but, if we look at the FFT data for $H \parallel a$ more carefully, we can see that the peak is broader that those found for $H \parallel c$. This may indicate that it indeed has two adjacent frequencies associated with the beat like feature seen in Fig. 4.4 (c). From the Onsager relation, $F^i = \frac{\hbar c}{2\pi e} S^i$, which states direct proportionality between frequency and extremal areas, three corresponding extremal area of the Fermi surface were calculated: $S_{F^1} = 0.00344\,\mathring{A}^{-2}$, $S_{F^2} = 0.0344\,\mathring{A}^{-2}$ and $S_{F^3} = 0.0378\,\mathring{A}^{-2}$.

MR was also measured at 5 different temperatures; 1.8 K, 3 K, 4 K, 5 K, and 7 K, and the FFT is done on each MR data set (Fig. 4.5) with same data processing. The amplitude of quantum oscillations decreases as temperature increases. Using Lifshitz-Kosevich theory explained in Chapter 2, we obtain the effective mass m^* by linear fitting using the mass plot in Fig. 4.5 insets. The calculated effective mass for F^1 is 0.19 m_e, F^2 is 0.25 m_e and F^3 is 0.25 m_e. The effective masses for F^2 and F^3 are same, and their frequencies are also almost same as well. These features in F^2 and F^3 might indicate that these frequencies are associated with an almost spherical sheet of the Fermi surface whereas F^1 is not.

4.4 ARPES

ARPES data were acquired using a tunable, vacuum ultraviolet laser-based ARPES [64] in collaboration with Yun Wu in Adam Kaminski's group. The samples were cleaved *in situ* at 40 K at a base pressure lower than 8×10^{-11} Torr. Momentum and energy resolution were set at ~0.005 Å^{-1} and 2 meV, respectively.

The clear signatures of T_N in magnetization and resistivity are accompanied with changes in the Fermi surface as well. Whereas the SdH oscillations can provide information about the low temperature, extremal orbit dimension, a T_N value of 255 K makes quantum oscillations measurements for $T > T_\text{N}$ highly unlikely. Fortunately, ARPES measurements can probe the Fermi surface both above and below T_N.

In Fig. 4.6, we show the Fermi surface plot and band dispersion measured using 6.70 eV photon energy. Fig. 4.6 (a) shows the $T = 40$ K, ARPES intensity in the first Brillouin zone, integrated within 10 meV about the chemical potential. The red arrows point to the location of two Fermi sheets identified in Figs. 4.6 (e) and (i). In Figs. 4.6 (b)-(e), we show the band dispersion along cuts 1-4 (marked in panel (a)) measured at $T = 40$ K. As we move away from Γ to Z (i.e. from cut 1 to cut 4 in Fig. 4.6), two hole pockets emerge as indicated by the red arrows, which can be better seen in the second derivative plots of the ARPES intensity shown in Figs. 4.6 (f)-(i).

In Figs. 4.7 (a)-(b), we show the band dispersion along cut 4 in Fig. 4.6 (a) measured at two temperatures: 270 and 40 K (above and below the AFM transition temperature, respectively). We can clearly see that above the AFM transition temperature of 255 K (in the paramagnetic state), there is only a single hole pocket (marked by red arrows). When the sample temperature is decreased to 40 K, another hole pocket emerges in the center. To better illustrate the band dispersion, we calculate and plot second derivative of the ARPES intensity in Figs. 4.7 (c)-(d).

Diameters of the two pockets that we marked on Fig. 4.7 at 40 K are 0.1708 $\mathring{A}^{-1}$ and 0.0815 $\mathring{A}^{-1}$. Assuming circular orbits, the calculated surface areas are 0.023 $\mathring{A}^{-2}$ and 0.005 $\mathring{A}^{-2}$. Former one may correspond to F^2 and F^3. The differences between SdH data and ARPES data may be due to limited access to full Brillouin zone along the k_x direction. Thus, the values that come from ARPES data often are close to, but different from the extremal value inferred from SdH oscillations, which give the true minimal or maximal value along the applied field direction, regardless of position in Brillouin zone.

The Fermi surface topology change is due to the magnetic transition from paramagnet to AFM. In the AFM state, the unit cell size can change, and it can affect the Brillouin zone in k-space. Thus, it introduces the band folding in the system. [22, 65] This is the reason why two bands were observed below T_N, although only one band was observed above the transition temperature.

4.5 Resistivity under pressure

The resistivity data under pressure were collected in collaboration with Udhara S. Kaluarachchi with two types of pressure cells. A Be-Cu/Ni-Cr-Al hybrid piston-cylinder cell (PCC), similar to that used in Ref. [20], was used for pressures up to 2.1 GPa. For this pressure cell, a 4:6 mixture of light mineral oil: *n*-pentane [20, 66] was used as a pressure medium. It solidifies at ∼3-4 GPa at room temperature [66, 67]. For higher pressure, a modified Bridgman anvil cell (mBAC) [67, 68] was used with a 1:1 mixture of *n*-pentane:iso-pentane as a pressure medium [66, 67, 69, 70]; the solidification of this medium occurs around ∼6-7 GPa at room temperature [66, 67, 71, 70]. For both cells, the pressure was determined by the superconducting transition temperature of Pb [72]

measured resistivity. The temperature dependent electrical resistivity of $CrAuTe_4$ was measured up to 5.22 GPa.

The temperature dependence of the resistivity at various pressures is shown in Fig. 4.8 (a). Note that we used different samples for each cells; RRR = 14 for the sample used in the PCC and RRR = 13 for the sample used in the mBAC. The data from each of the two samples was normalized to the ambient pressure resistivity value from Fig. 4.3. The antiferromagnetic transition temperature decreases as we apply pressure. $T_{\mathrm{N}} = 254\,\mathrm{K}$ inferred from the ambient pressure decreases monotonically to $T_{\mathrm{N}} = 236\,\mathrm{K}$ at 5.22 GPa (see Fig. 4.9 (a)). The rate of suppression of T_N is -3.4 K/GPa when we assume a linear change. In fact, though, there are two breaks in slope of $T_{\mathrm{N}}(P)$, one at roughly 2 GPa and a second at roughly 4 GPa. Whereas the 2 GPa change will be discussed further below, the 4 GPa change is most likely associated with the $T_{\mathrm{N}}(P)$ line crossing the solidification temperature line ($T_{\mathrm{s}}(P)$) for the 1:1 mixture of n-pentane:iso-pentane pressure medium near 4 GPa. [67]

The residual resistivity ratio of $CrAuTe_4$ also changes with pressure and manifests a very clear, non-monotonic behavior (Fig. 4.9 (b)). The broad, local maxima between 1.7 and 2.1 GPa is followed by a shallow drop at higher pressures.

Figure 4.8 (b) shows the MR ratio (defined as $(\rho(H) - \rho(H = 0))/\rho(H = 0)$)for $T = 1.8\,\mathrm{K}$ measured at 14 different pressures. To be consistent, we always applied the current along the b-axis and magnetic field along the c-axis. MR shows quadratic behavior at low pressure, and near-linear behavior is detected at high pressure. To be more quantitative, we fitted the MR data with cH^n, where c is a constant, H is the field, and n is an exponent.The values of n are plotted in Fig. 4.9 (c). n is around 2 at low pressure, but starts to drop from 2 GPa. Finally, $n \sim 1$ around 5.22 GPa. Conventionally MR is proportional to H^2, but it sometimes shows linear MR when there is scattering and magnetic breakdown. [11] More recently, A. A. Abrikosov suggested that linear energy dispersion can induce linear MR. [73] Although sudden increases in scattering (with pressure) are possible, magnetic breakdown happens over limited high field regimes. However,

electronic transition is possible with introducing linear dispersion. It is possible, then, that the anomaly in MR exponent is a result of the electronic phase transition under pressure.

Figure 4.9 (c) also shows the MR at 90 kOe. The MR is 1.85 at ambient pressure, with a local maximum at 0.87 GPa of 3.45, and then drops down to 0.57 at 5.22 GPa. It noticeably starts to drop around 2 GPa, and, as expected, at higher pressures shows a similar pressure dependence as the exponent, n. Given that the pressure dependence of T_N, RRR, the MR as well as the MR power-law exponent all show changes in behavior just below 2 GPa, it is likely that there is a pressure induced transition near this pressure.

The pressure dependence of the SdH oscillations was tracked as well. As pressure increases, both frequencies move to higher values (Fig. 4.10). This implies that the respective Fermi surfaces areas in k-space increase in the ab plane.The pressure dependences of the changing frequencies are presented in Fig. 4.10 (a). Both frequencies, F^1 and F^2, show almost linear change. The pressure derivatives of extremal cross sections which is defined as $dlnF/dp$ are calculated for each frequencies; $dlnF_1/dp = 1.31$ GPa^{-1} and $dlnF_2/dp = 0.23$ GPa^{-1}. The pressure derivative of F_2 is comparable to previous results on Cd and Bi, [20, 74] but F_1 is at least 2 times greater.

Not only frequencies but also amplitudes are changed as pressure is increased. As F^1 and F^2 are smeared out, no more frequencies are detectable in the PCC for $P > 1.42$ GPa.. This may suggest that the local curvature near extremal cross-sections of the Fermi surface is changing as we apply pressure. In addition, we start to seeing a new low frequency peak from 2.08 GPa, and finally pronounced low frequency peak, $F^4 = 0.71$ MOe, is observed at 3.5 GPa. Low frequency peaks can sometimes be due to an artifact during the data processing. However, F^4 has large amplitude and, as shown in the inset of Fig. 4.10 (g), it can even be clearly seen in the raw data.

Based on the present data, it is apparent that the antiferromagnetism in $CrAuTe_4$ is not particularly "fragile" and much higher pressures would be needed to suppress it. On the other hand, there is a pressure induced phase transition near 2 GPa. We cannot identify the nature of this transition; it could be a pressure induced change in the magnetic ordering wave vector, it could be a structural phase transition, or it could be a Lifshitz transtion.

4.6 Summary

In summary, we studied physical properties of high quality single crystal, $CrAuTe_4$. The temperature dependent magnetization has been measured, and we observed the anisotropic susceptibility consistent with the spins aligned antiferromagnetically along the c-axis below 255 K. The temperature dependent resistivity also showed a clear, loss-of-spin-disorder-scattering feature at the antiferromagnetic transition temperature. The 2 K MR showed anisotropy with factor of 2, SdH oscillations are observed and analyzed. The band structure was measured by ARPES below and above the Neel temperature; band folding due to the antiferromagnetic transition is detected. To test for possible fragile magnetism, the pressure dependence of the temperature dependent electrical resistivity was measured for $p < 5.25$ GPa. T_N was suppressed to 236 K by 5.22 GPa. Suggesting a possible pressure induced phase transition that affects the electronic properties.

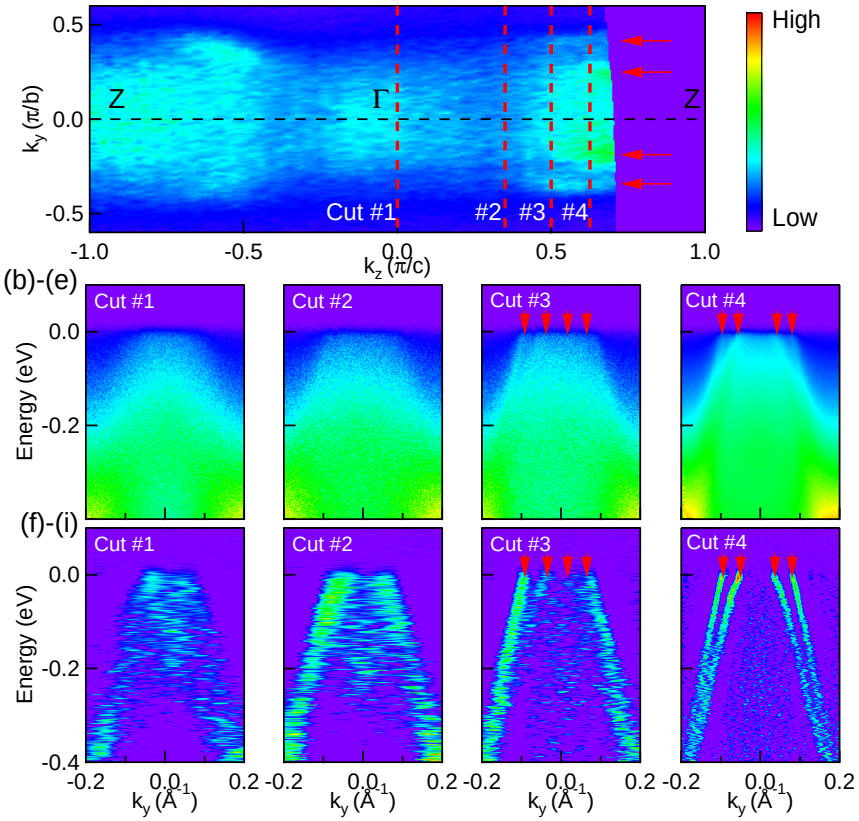

Figure 4.6 Fermi surface plot and band dispersion measured using 6.70 eV photon energy. (a) Plot of ARPES intensity integrated within 10 meV about the chemical potential measured at T =40 K. High intensity areas correspond to location of Fermi sheets and/or proximity of the bands to the chemical potential. The red arrows indicate the location of the Fermi momenta found in figures (e) and (i) below. (b)-(e) ARPES intensity along cuts 1-4 measured at $T = 40$. (f)-(i) The intensity plots of the second derivatives of data in (b), (c), (d) and (e). The red arrows in (d),(e), (h) and (i) mark the the locations of Fermi momenta.

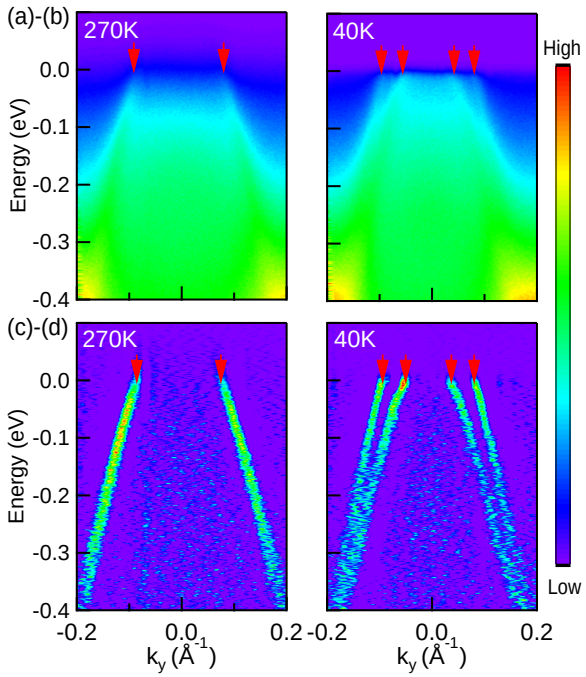

Figure 4.7 Band dispersion measured using 6.70 eV photon energy. (a)-(b) ARPES intensity along cut 4 measured at T =270 and 40 K, respectively. (c)-(d) The intensity plots of the second derivatives of data in (a) and (b). The red arrows mark the Fermi crossings.

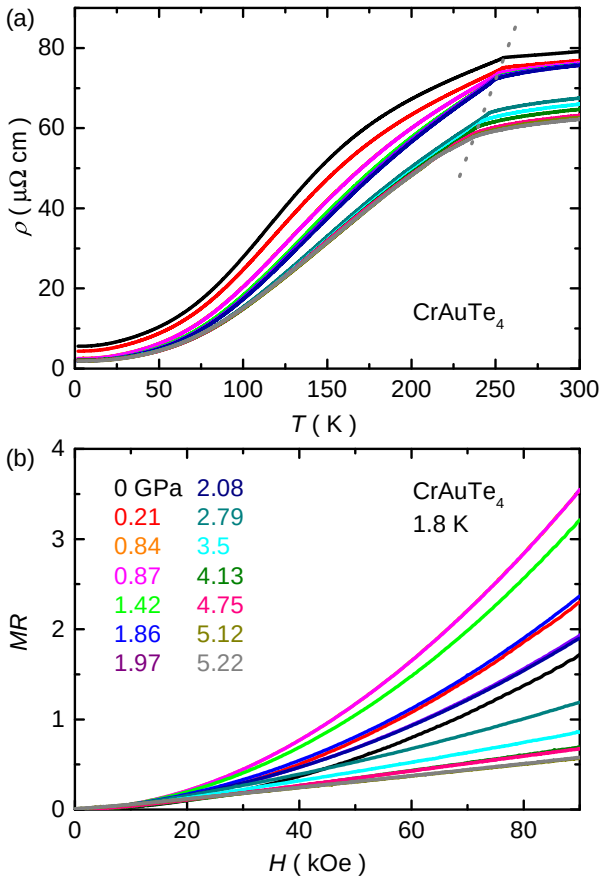

Figure 4.8 (a) Temperature dependent resistivity at 0, 0.21, 0.84, 0.87, 1.42, 1.86, 1.97, 2.08, 2.79, 3.50, 4.13, 4.75, 5.12 and 5.22 GPa. (b) MR as a function of field at 1.8 K with same pressures as (a).

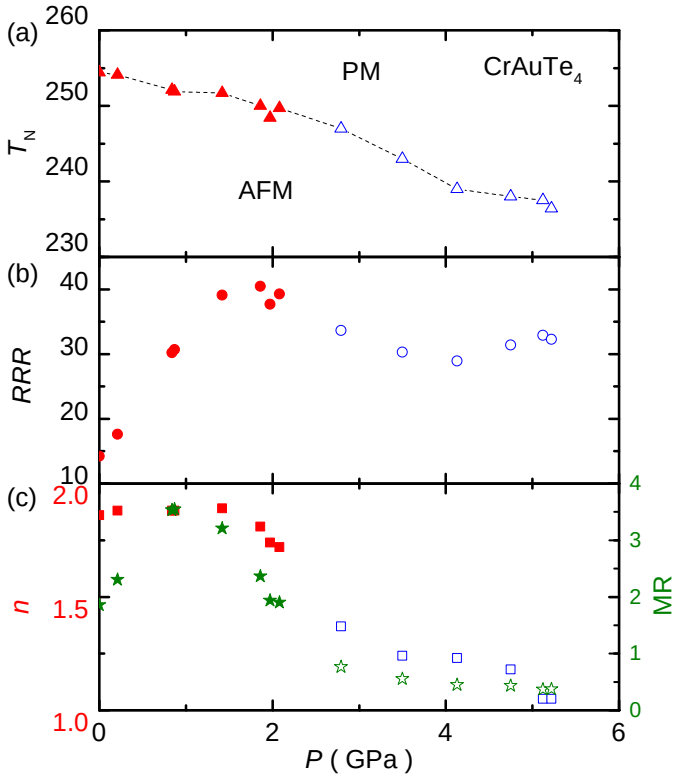

Figure 4.9 Pressure dependence of transport properties: (a) transition temperature (filled red triangle data was measured in piston-cylinder cell, open blue triangle data was measured in Bridgeman cell) (b) RRR (filled red circle data was measured in piston-cylinder cell, open blue circle data was measured in Bridgeman cell) (c) (left) square stands for exponent of H (filled red square data from piston-cylinder cell, open blue square data from Bridgeman cell), (right) green stars are MR at 90 kOe (filled data from piston-cylinder cell, open data from Bridgeman cell).

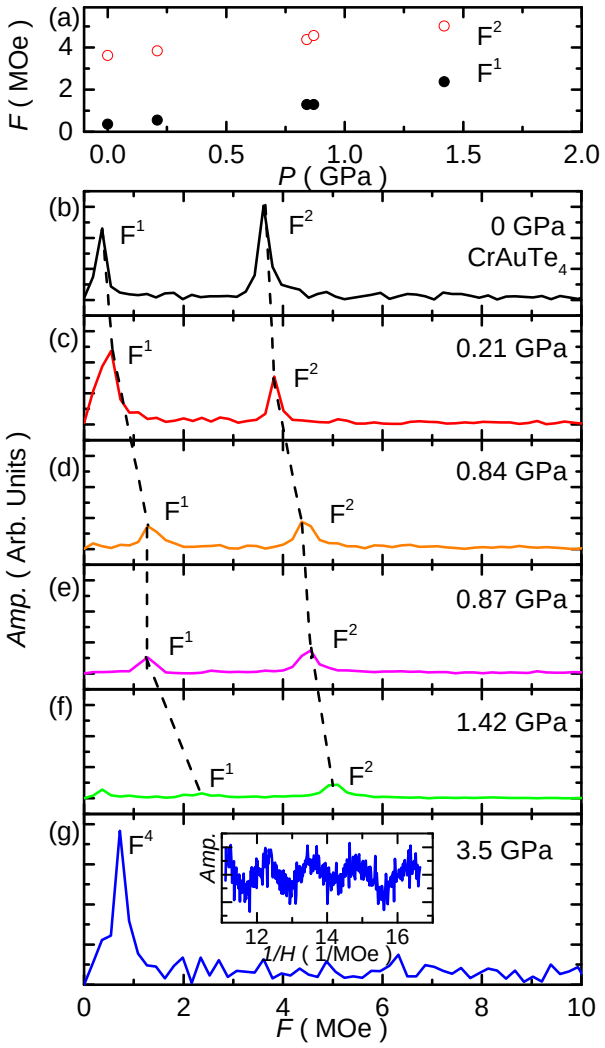

Figure 4.10 FFT results of SdH oscillation from 0 GPa to 1.42 GPa, and 3.5 GPa (a) overall trend of frequencies change as a function of pressure. (b) 0 GPa, (c) 0.21 GPa, (d) 0.84 GPa, (e) 0.87 GPa, (f) 1.42 GPa, (g) 3.5 GPa. Inset of (g) is the periodic oscillation as a function of 1/H after subtracting background.

CHAPTER 5. A STUDY OF THERMODYNAMIC, TRANSPORT AND BAND STRUCTURE PROPERTIES OF $PdSn_4$ INCLUDING EXTREMELY LARGE MAGNETORESISTANCE AND KOHLER'S RULE ANALYSIS

The following context is a slightly modified version of the published work in Ref. [75]. DOI: http://dx.doi.org/10.1103/PhysRevB.96.165145. Reprinted (abstract/excerpt/figure) with permission from [N. H. Jo *et. al.*, Phys. Rev. B 96.165145 (2017)]

The recent discovery of three-dimensional topological semi-metals generated lots of attention. Topological semi-metals can be classified as three different types: [76] a Dirac semimetal, a Weyl semimetal, and a nodal-line semimetal. A Dirac semimetal has points in the Brillouin zone where doubly degenerate conduction and valence bands are touching linearly, and has been realized in Na_3Bi and Cd_3As_2. [77, 78] A Weyl semimetal is similar to Dirac semimetal, but a Weyl semimetal exhibits Weyl points that are crossing of singly degenerate electronic bands, which requires the breaking of either time-reversal or inversion symmetry. Weyl points have chirality which is represented by the sign of the determinant for the velocity tensor. [79] Experimental manifestations of Weyl semimetals are: TaAs, NbAs, TaP and transition metal dichalcogenides including WTe_2 . [80, 81, 82, 83, 84] A nodal-line semimetal has a gap closing along a line in the Brillouin zone instead of at isolated points. Several materials have experimentally confirmed to be nodal-line semimetals: $PbTaSe_2$, ZrSiS and $TlTaSe_2$. [85, 86, 87] A different type of a novel topological quantum structure was identified recently in $PtSn_4$ which has a Dirac node arc feature on the surface, whose (topological) origin is still unknown. [88] In the bulk, $PtSn_4$ is a metallic with a number of complex electron and hole Fermi surface sheets containing significant carrier densities. [88]

The fascinating thermodynamic and transport properties of $PtSn_4$ were reported in Ref. [89]. Most importantly, it manifests an extremely large magnetoresistance (XMR) of $\sim 5 \times 10^5$ % for

$T = 1.8\,\mathrm{K}$ and $H = 140\,\mathrm{kOe}$, without any evidence of saturation. [89] In the following years, many of other topological materials that also showed XMR have been found.

Several mechanisms have been suggested for such XMR in various materials. Nearly perfect electron-hole compensation has been suggested as the origin of XMR ($\sim 10^5\,\%$ at 4.5 K and 147 kOe) in WTe_2. [9] (Although it has also been noted that in this material there is a clear relation between MR and the residual resistivity ratio, ρ_0). [90] Magnetic field induced changes in Fermi surface structure have been suggested as the cause of XMR in $NbSb_2$ ($\sim 10^5\,\%$ at 2 K and 9 T) and Cd_3As_2 ($\sim 10^5\,\%$ at 5 K and 9 T), specifically field induced gaps in Dirac points or splitting of Dirac Fermi points into separated Weyl points. [9, 91] More recently, for the case of LaSb ($\sim 10^6\,\%$ at 2 K and 9 T) and LaBi ($\sim 10^5\,\%$ at 2 K and 9 T) XMR has been associated with *d-p* orbital mixing. [92, 93] Despite all of these possible mechanisms, the origins of XMR in all of these materials are open to debate.

$PdSn_4$ is isostructural to $PtSn_4$; [94, 95] it has an orthorhombic structure and a space group number of 68, with Pd and Sn each having a unique crystallographic site. [95] The lattice parameters of $PdSn_4$ are $a = 6.4417\,\mathring{A}$, $b = 11.4452\,\mathring{A}$ and $c = 6.3886\,\mathring{A}$, which are very similar to those of $PtSn_4$: $a = 6.418\,\mathring{A}$, $b = 11.366\,\mathring{A}$ and $c = 6.384\,\mathring{A}$. [95, 96] Both materials have a layered structure along the crystallographic b direction owing to the weak van der Waals bonding between Sn atoms. Since not only the structure, but also the electron count is same, the primary difference between $PdSn_4$ and $PtSn_4$ may be the reduced spin orbit coupling strength or slight lattice expansion associated with $PdSn_4$. Therefore, it is interesting to compare these two materials.

In this chapter, the physical properties of $PdSn_4$, including temperature and the magnetic field dependent transport and magnetic properties as well as a detailed angle resolved photoemmision spectroscopy (ARPES) and density functional theory (DFT) study of its electronic bulk and surface band structure will be discussed. Compared to $PtSn_4$, the anisotropic physical properties of $PdSn_4$ are qualitatively similar. In contrast, our ARPES results show that whereas $PtSn_4$ exhibits a Dirac node arc at the surface, the corresponding surface state is clearly gapped out in $PdSn_4$. We rule out a number of proposed microscopic mechanisms for XMR in $PdSn_4$, through detailed analysis

of the magnetoresistivity and band structure. In particular, we show that carrier compensation cannot explain XMR in either $PtSn_4$ or $PdSn_4$. In addition, we point out a scaling property of the magnetoresistivity that follows Kohler's rule over a wide magnetic field and temperature range, revealing to a robust scale invariance of the electronic orbital motion known from classical descriptions of magnetotransport.

5.1 Single crystal growth and XRD

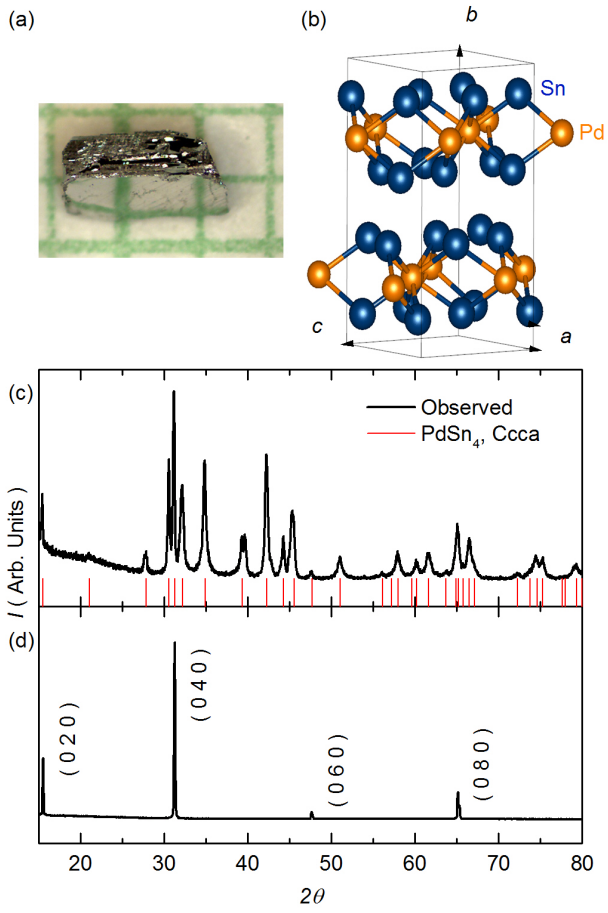

Figure 5.1 (a) Single crystal of $PdSn_4$. (b) Crystal structure (Pd: orange sphere, Sn: blue sphere). (c) Powder X-ray diffraction pattern (Black lines) and reported $PdSn_4$ (*Ccca*) peaks from Ref. [95] (Red lines). (d) Single crystal X-ray diffraction pattern identifying the (0 h 0) lines.

Single crystals of $PdSn_4$ were grown out of Sn-rich binary melts. Detailed explantion can be found in the section 3.1. We put an initial stoichiometry of Pd_2Sn_{98} into a fritted alumina crucible [Canfield Crucible Set (CCS)], [34] and then sealed in it into an amorphous silica tube under partial Ar atmosphere. The ampoule was heated up to 600 °C over 5 hours, held there for 5 hours, rapidly cooled to 325 °C and then slowly cooled down to 245 °C over more than 100 hours, and then finally decanted using a centrifuge. [36] The single crystalline sample has a clear plate like shape with mirrored surface and typical dimension of $\sim 2\,\text{mm} \times 1\,\text{mm} \times 0.3\,\text{mm}$.(Fig. 5.1 (a))

Fig. 5.1 (c) shows XRD patterns of $PdSn_4$. All the peak positions are well matched with the reported orthorhombic $PdSn_4$ structure. [95] However, the relative intensity of the peaks is different from the calculated powder pattern, presumably reflecting the preferential orientation of the ground powder due to the layered structure. The crystal structure in real space is shown in Fig. 5.1 (b) and preferential orientation. The crystallographic b-axis is anticipated to be perpendicular to the mirrored surface shown in Fig. 5.1 (a). To confirm this, we did XRD on oriented single crystals. [43] When the x-ray beam is incident perpendicular to the surface, only (0 k 0) peaks were observed as shown in Fig. 5.1 (d). This confirms that the crystallographic b direction is perpendicular to the mirrored surface shown in Fig. 5.1 (a).

5.2 Specific heat

The temperature dependent specific heat, C_P, of $PdSn_4$, shown in Fig. 5.2, does not show any signature of a phase transition. We plot the C_P/T as a function of T^2 in the inset to Fig. 5.2 to infer the electronic specific heat coefficient, γ, and the Debye temperature, Θ_D. This is based on the relation $C_P = \gamma T + \beta T^3$ at low temperature; $\gamma = 4\,\text{mJ/mol K}^2$ and $\Theta_D \sim 206\,\text{K}$. These values are very similar to those of $PtSn_4$ ($\gamma \sim 4\,\text{mJ/mol K}^2$ and $\Theta_D \sim 210\,\text{K}$). [89] Since both systems have γ values of less than $1\,\text{mJ/mol K}^2$ atom, neither has a significant density of states at the Fermi surface or strong electron correlations.

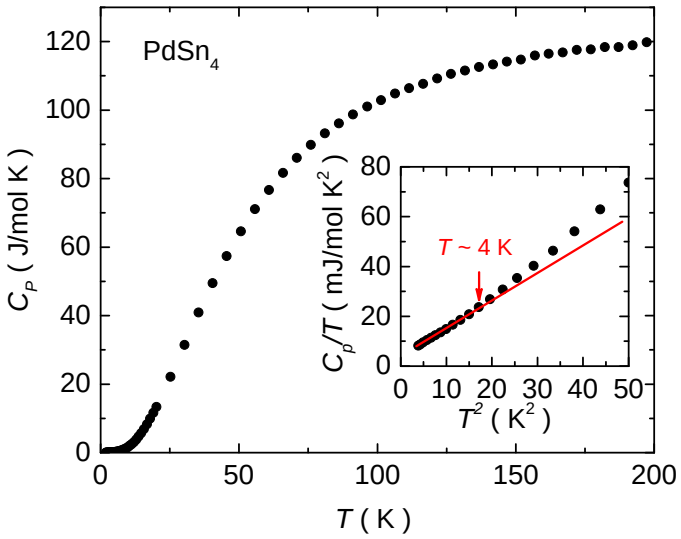

Figure 5.2 Temperature dependent specific heat, C_P, of $PdSn_4$. Inset shows C_p/T as a function of T^2. The red line is a linear fit to the lowest temperature $PdSn_4$ data.

5.3 Resistivity

Figure 5.3 (a) shows the temperature dependent resistivity, $\rho(T)$, measured from 1.8 K to 300 K. The current was applied perpendicular to the crystallographic b direction. (i.e. within the plane of the plate-like sample). Sample S1 has a residual resistivity ratio (RRR $= \rho(300\ \mathrm{K})/\rho(1.8\,\mathrm{K})$) value of 331, and sample S2 has RRR = 625. In both cases, the large RRR indicates the high quality of the crystals. The overall behavior of $\rho(T)$ is metallic, which is similar to $PtSn_4$. [89] It shows almost linear temperature dependence at high temperatures; the low temperature ($T < 10\,\mathrm{K}$) data from S1 and S2 were fitted with a polynomial function, $\rho\,(\mathrm{T}) = \rho_0 + AT^2$. The obtained values are $\rho_0 = 0.105\,\mu\Omega\,\mathrm{cm}$ and $A = 2.7 \times 10^{-4}\,\mu\Omega\,\mathrm{cm/K^2}$ for S1, and $\rho_0 = 0.049\,\mu\Omega\,\mathrm{cm}$ and $A = 2.2 \times 10^{-4}\,\mu\Omega\,\mathrm{cm/K^2}$ for S2. Given that S2 has RRR, ρ_0 and A values closer to those reported for $PtSn_4$ than S1, [89] we chose to use S2 to carry out further transport experiments with the applied magnetic field.

The difference in A values between two samples can be associated with uncertainty in geometric factors, since single crystals of $PdSn_4$ are easy to be exfoliated and bended. In order to confirm

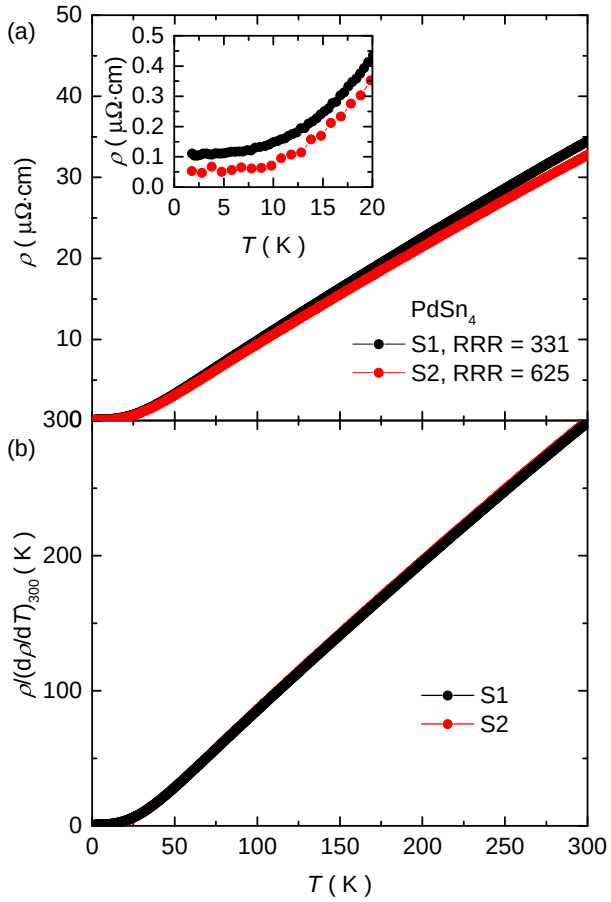

Figure 5.3 (a) Temperature dependent resistivity of two $PdSn_4$ single crystals. (b) Temperature dependent resistivity of two $PdSn_4$ single crystals nomalized to their room temperature respective slopes.

this hypothesis, we plot temperature dependent resistivity normalized to the room temperature slopes, which can compensate for the uncertainty of the geometric factor. [97] As shown in Fig. 5.3 (b), temperature dependent resistivity data of both samples are same except the slight different residual resistivity, ρ_0. Therefore, we can conclude that the difference in resistivity other than ρ_0 between two samples are indeed due to uncertainty in geometric factors.

The $\rho(T)$ of $PdSn_4$ for $H = 140\,\mathrm{kOe}$ was measured from 1.8 K to 300 K with the two different magnetic field directions (red filled circles for $H \perp b$ and blue filled squares for $H \parallel b$) (Fig. 5.4 (a)). Note that the current was always applied in an $I \perp b$ and $I \perp H$ direction. The current thus always flows in the a-c plane, perpendicular to the applied magnetic field. For comparison, we also

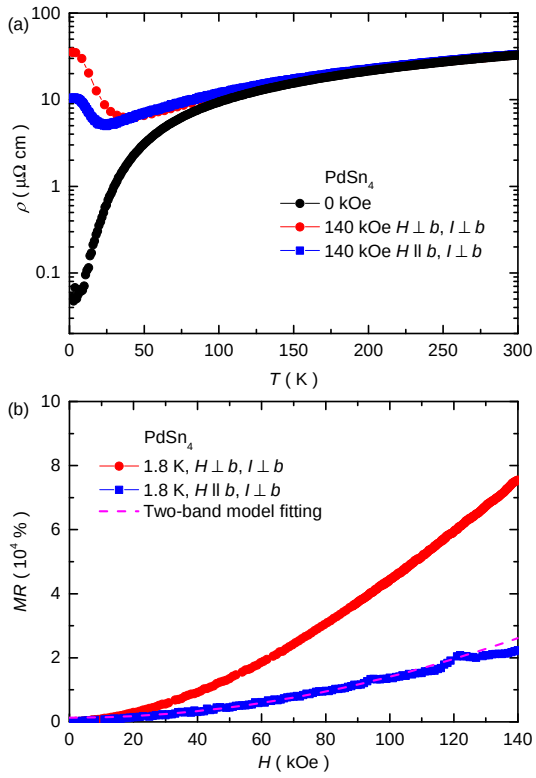

Figure 5.4 (a) Temperature dependent resistivity of $PdSn_4$ in zero applied magnetic field (black filled circles), and in 140 kOe for different magnetic field directions; red filled circles ($H \perp b$, $H \perp I$) and blue filled squares ($H \parallel b$, $H \perp I$). (b) Magnetoresistance (MR) of $PdSn_4$ at 1.8 K for different magnetic field and current directions; red filled circles ($H \perp b$, $H \perp I$), blue filled squares ($H \parallel b$, $H \perp I$). Magenta dashed-line is fitted line based on a two-band model (see text).

plotted the $\rho(T)$ of $PdSn_4$ for $H = 0$ kOe (black filled circles). For both field directions, $PdSn_4$ shows a strong field dependence at low temperatures. To be more specific, for both directions of applied field the 140 kOe MR starts becomming large below $\sim$100 K. A local minimum in the 140 kOe resistance is observed near 40 K ($H \perp b$) and 25 K ($H \parallel b$), followed by steep increases in resistivity that tends to saturate as $T \rightarrow 2$ K.

Transverse magnetoresistance (MR) measurements were carried out from 0 Oe to 140 kOe at 1.8 K, with MR defined as $(\rho(H) - \rho(H = 0)) \times 100/\rho(H = 0)$. The magnetic field dependency of MR in both directions is quadratic rather than linear, and there is no evidence of saturation in MR

up to 140 kOe. Anomalies in the higher magnetic field regime are due to quantum oscillations. (see discussion below). The size of the MR at 1.8 K and 140 kOe is $\sim 8 \times 10^4$ % ($H \perp b$) and $\sim 2 \times 10^4$ % ($H \parallel b$) both of which are extremely large values. It is interesting that both $PtSn_4$ and $PdSn_4$ show a larger MR when the magnetic field is applied perpendicular to the b direction (i.e. within the basal plane). This is in contrast to many layered materials with large MR anisotropy that manifest the largest MR when the magnetic field is applied perpendicular to the plane. [98, 99] Furthermore, for layered materials that manifest quasi-two dimensional Fermi surfaces, it has been predicted that the transverse MR along one magnetic field direction (perpendicular to the plane) increases quadratically while it tends to saturate for a field that lies within the plane. [12] Given the quadratic MR, for both field directions, found for $PdSn_4$ as well as $PtSn_4$, it seems that the mangetotransport is dominated by 3D Fermi surface (FS) sheets, even though each compound cleaves and exfoliates well.

5.4 Hall coefficient

Electron-hole compensation can be a reason for large MR and has been invoked in the case of WTe_2. [9] In general, the conductivity tensor components σ_{xy} and σ_{yx} are proportional to $1/H$ when the carrier density of electrons and holes are not approximately equal (i.e. $n_e > n_h$ or $n_e < n_h$). Then the diagonal components of resistivity tensors, except ρ_{zz}, saturate as the magnetic field goes to infinity. On the other hand, the resistivity tensor components ρ_{xx} and ρ_{yy} increase quadratically without saturating at high field when $n_e \approx n_h$ since σ_{xy} and σ_{yx} are then dominated by higher order of $1/H$ terms. One should note that this is true only if the following assumptions are fulfilled: (i) there are closed trajectories and (ii) in the high field regime. [12] In order to see whether such a compensation senario is possible for $PdSn_4$, we measured its Hall resistivity, ρ_H. In Fig. 5.5 (a), the temperature-dependent Hall coefficient, $R_H = \rho_H/H$, of $PdSn_4$ at 140 kOe from 1.8 K to 300 K is plotted. Above 65 K, the R_H of $PdSn_4$ shows a relatively weak, monotonic dependence on temperature with a positive value which indicates that hole-like carriers dominate its transport properties. R_H of $PdSn_4$ starts to decrease rapidly below 65 K, crosses $R_H = 0$ at

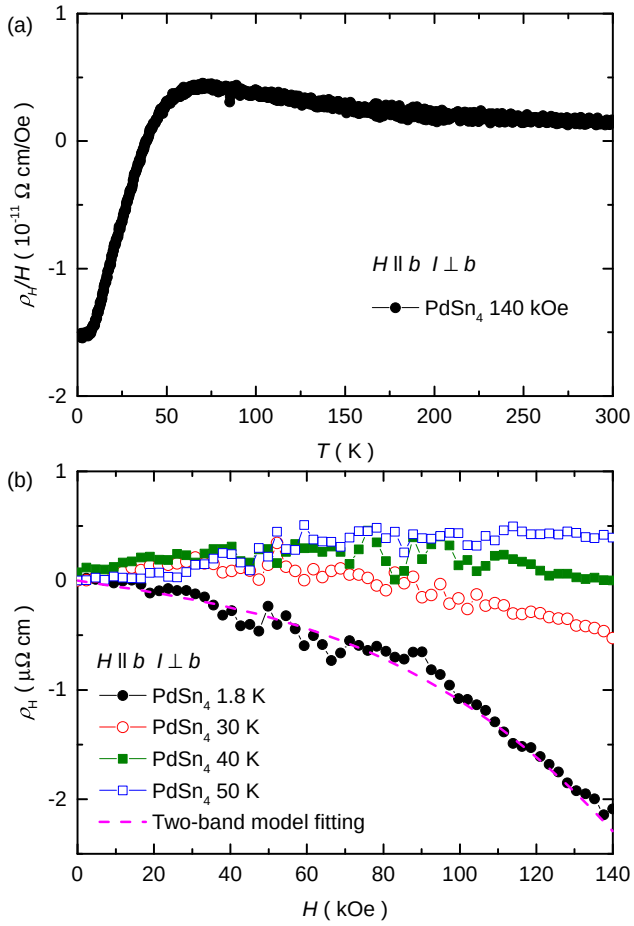

Figure 5.5 (a) Temperature dependent Hall resistivity divided by the applied magnetic field, $\rho(H)/H$, of $PdSn_4$ for $H = 140\,kOe \parallel b$. (b) magnetic field dependent Hall resistivity of $PdSn_4$ at 1.8 K, 30 K, 40 K, and 50 K. The dashed magenta line is based on a two-band model (see text).

38 K, and then saturates to $R_H \approx -1.5 \times 10^{-11}\,\Omega\,\mathrm{cm/Oe}$ below 7 K. Given that R_H changes sign at low temperatures, it is tempting to associate the zero crossing with perfect carrier compensation. However, this assumes that the mobilities of all carriers are equal. This is because R_H is not only a function of carrier density but also mobility. Therefore, we need a way to disentangle the carrier density and mobility contributions to R_H.

One indication of compensation is a nonlinear behavior of $\rho_{xy}(H) \equiv \rho_H$ in high magnetic fields. [12] Thus, we measured the ρ_H of $PdSn_4$ as a function of the magnetic field, as shown in

Fig. 5.5 (b). The ρ_H of $PdSn_4$ shows nonlinear behavior in the low temperature regime, where it shows non-saturating, large MR. This means $PdSn_4$ has very similar values of carrier densities, i.e. $n_e \approx n_h$, whereas the mobility of electrons is larger compared to the mobility of holes based on $R_H(T)$ at low temperature (see Fig. 5.5 (a)).

We were able to use a simplified two-band model to fit the $\rho_H(H)$ and MR data at 1.8 K in order to do a quantitative analysis. [11] This method has been successfully used in many materials. [100, 101, 102]

$$\rho_{xx}(B) = \frac{1}{e}\frac{(n_h\mu_h + n_e\mu_e) + (n_h\mu_e + n_e\mu_h)\,\mu_h\mu_e B^2}{(n_h\mu_h + n_e\mu_e)^2 + (n_h - n_e)^2\mu_h{}^2\mu_e{}^2B^2} \tag{5.1}$$

$$\rho_{xy}(B) = \frac{B}{e}\frac{\left(n_h\mu_h{}^2 - n_e\mu_e{}^2\right) + (n_h - n_e)\,\mu_h{}^2\mu_e{}^2B^2}{(n_h\mu_h + n_e\mu_e)^2 + (n_h - n_e)^2\mu_h{}^2\mu_e{}^2B^2} \tag{5.2}$$

The values obtained from the two-band model from the 1.8 K data, are $n_e = (1.6 \pm 0.1) \times 10^{27}\,\mathrm{m}^{-3}$, $n_h = (1.5 \pm 0.1) \times 10^{27}\,\mathrm{m}^{-3}$ such that their ratio is $c = n_h/n_e = 0.93 \pm 0.1$. The mobilities are found to be $\mu_e = (0.34 \pm 0.04)\,\mathrm{m}^2/\mathrm{V\,s}$ and $\mu_h = (0.27 \pm 0.03)\,\mathrm{m}^2/\mathrm{V\,s}$ such that their ratio is $c_\mu = \mu_h/\mu_e = 0.80 \pm 0.18$. The corresponding R^2-values of the fit are very good $R^2 - 1 = 0.02$, showing that although the Fermi surface clearly consists of several hole and electron pockets with different mobilities and effective masses (see below), the magnetoresistivity can be well captured (at least qualitatively) within a two-band model. We want to emphasize that the simplified two-band model equations above are based on the assumption of (i) only one electron and one hole band are present, (ii) the isotropic free electron gas model is applicable, and (iii) components of the conductivity tensor that contain z need not be considered. In addition, we have found that slightly worse but still reasonable fits can be obtained with other mobility ratios c_μ and total densities n_e. The data constrains the ratio c more than the value of n_e. [For example, similarly good fits to the data could be found for $n_e \simeq n_h \sim 10^{33}\ \mathrm{m}^{-3}$ with $c_\mu = \mu_h/\mu_e = 0.0013$. Clearly the size of n_e and n_h is not physical, but it is worth noting that they are still roughly equal.]

The best fits we have obtained are plotted in both Fig. 5.4 (b) and Fig. 5.5 (b) with magenta dashed lines. Unlike $PtSn_4$, [89] the values of n_e and n_h for $PdSn_4$ obtained from the fit are very

similar, within about 7 % of each other, whereas $\mu_e > \mu_h$, which was expected from the Hall data at the high magnetic fields. The shape of ρ_{xy} immediately yields two constraints $(i) n_e\mu_e^2 > n_h\mu_h^2$ and $n_h < n_e$, which follows directly from the fact that the linear and cubic coefficients in an expansion $\rho_{xy} = a_1 B + a_3 B^3$ both need to be negative $a_1, a_3 < 0$. From the fact that the non-linearity sets in around $B_2 \approx 8$T, we can further derive the relation $(1-cc_\mu^2)(1+cc_\mu)^2/[cc_\mu^2(1-c)(1+c_\mu)^2] \approx B_2^2\mu_e^2$.

5.5 Magnetization

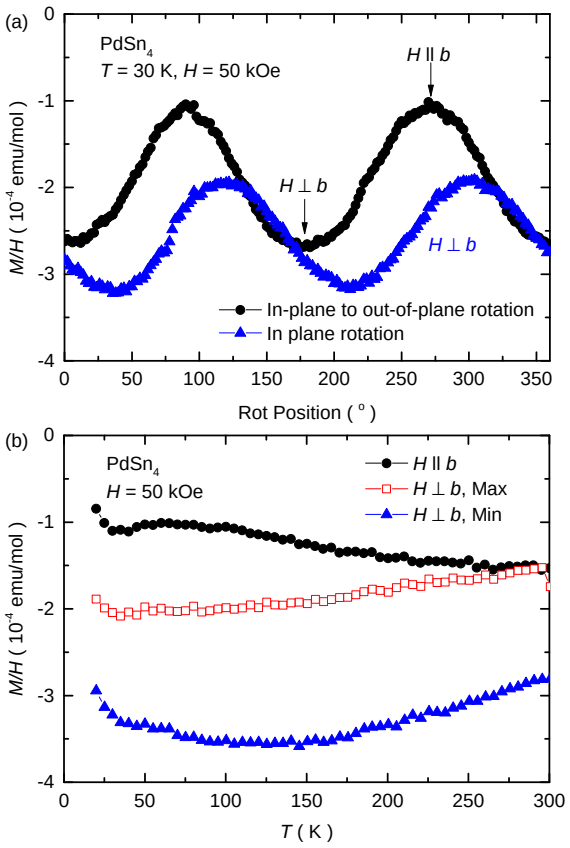

Figure 5.6 (a) Angular-dependent magnetic susceptibility of $PdSn_4$ in both in-plane to out-of-plane rotation and in-plane rotation at $T = 30$ K and $H = 50$ kOe. (b) Temperature-dependent magnetic susceptibility of $PdSn_4$ at 50 kOe, $H \parallel b$ (black filled circles), $H \perp b$ for maximal in-plane magnetization orientation (red open rectangles) and $H \perp b$ for minimal in-plane magnetization orientation (blue filled triangles)

A modified QD sample rotating platform for MPMS instrument with an angular resolution of 0.1 deg was used for angular-dependent dc magnetization measurements in collaboration with Sergey L. Bud'ko. Both out-of-plane and in-plane angular dependent magnetization measurements are shown in Fig. 5.6 (a). The observed magnetic properties of $PdSn_4$ are diamagnetic in all directions with a clear anisotropy between the a-c plane and the b direction. The data are taken at 30 K and 50 kOe, but the magnetization is linear as a function of the magnetic field for $H \leq 7$ T, so the angular dependent magnetic susceptibilities measured in different magnetic fields of 25 kOe, 50 kOe and 70 kOe are the same. On the other hand, both angular dependent magnetic susceptibility show deviations from simple sine function behavior when the temperature is below 30 K due to quantum oscillations.

Based on the angular dependent magnetization measurements, we find that the maximum susceptibility (smallest negative value) occurs for $H \parallel b$. For $H \perp b$, we find a simple angular variation of $M(\theta)$ and can identifiy an in-plane field orientation that produces a minimal and maximal response separated by 90^o. In Fig. 5.6 (b) we present the temperature dependence magnetization from 20 K to 300 K with 50 kOe along the three different magnetic field directions. All of them show weak temperature dependence, and the anisotropy gets smaller as temperature is increased. The low temperature upturn is due to entering the temperature range of quantum oscillations (see below).

In order to understand the physical meaning of an anisotropic susceptibility, it is important to separate core diamagnetism from Pauli paramagnetism and Landau diamagnetism. If we subtract the core diamagnetic contribution, [103, 104] we can infer the conduction electron contribution to the magnetic susceptibility. Even after the core diamagnetic correction, $\chi_{core} = -1.05 \times 10^{-4}$ emu/mol of $PdSn_4$, [103, 104] the remaining conduction electron susceptibility is still essentially diamagnetic. Based on an equation for the total electronic susceptibility of a metal [105]

$$\chi = \chi_P \left[1 - \frac{1}{3}\left(\frac{m_e}{m^*}\right)^2\right], \tag{5.3}$$

where m_e is an electron mass, m* is an effective mass and χ_P is Pauli paramangetism, the result indicates that the carriers should have rather small effective masses.

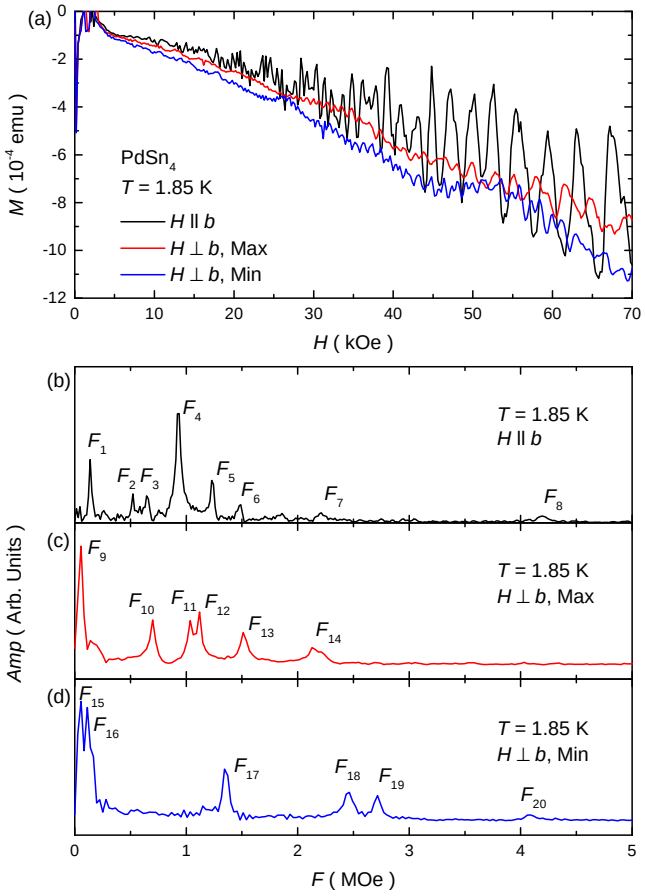

Figure 5.7 (a) Magnetization isotherms of $PdSn_4$ without background subtraction for $H \parallel b$, $H \perp b$, Max and $H \perp b$, Min at 1.85 K. (b) FFT spectra of dHvA data for $H \parallel b$. (c) FFT spectra of dHvA data for $H \perp b$, Max. (d) FFT spectra of dHvA data for $H \perp b$, Min.

More detailed information about the Fermi surface and effective masses can be obtained via measurement and analysis of quantum oscillations. Thus, we measured the magnetization of $PdSn_4$ as a function of the magnetic field, $M(H)$, up to 70 kOe at 1.85 K in all three salient directions: $H \parallel b$, $H \perp b$, Max and $H \perp b$, Min as shown in Fig. 5.7 (a). Note that the plotted magnetization data are raw data without subtracting the background of the sample rotator and data for low magnetic field ($H \leq 3$ kOe) are not reliable (Reg fit was below 0.5, possibly complication due to the background from the rotator), but clear de Haas van Alphen (dHvA) oscillations are readily detected. For analysis, the oscillatory part of the magnetization is obtained as a function of $1/B$

after subtracting a linear background. We then used a FFT algorithm. The FFT analyses are shown in Fig. 5.7 (b) for $H \parallel b$, Fig. 5.7 (c) for $H \perp b$, Max and Fig. 5.7 (d) for $H \perp b$, Min. All the frequencies are labeled on the figures and listed in the Table 5.1. F_{14} is broad, and it might be a superposition of the second harmonics of F_{11} and F_{12}. In addition, F_{19} is likely a second harmonic of F_{17}. Here, we note that Shubnikov-de Haas oscillation show some low frequencies (F_1, F_2 and F_3) for $H \parallel b$ as noted in Fig. 5.4 (b), but these oscillations are much clearer in the $M(H)$ data. The corresponding extremal areas were calculated via the the Onsager relation which gives a direct proportionality between frequency and extremal area, $F_{\rm i} = \frac{\hbar c}{2\pi e} S_i$.

Table 5.1 Frequencies of the peaks from Fig. 5.7 (b)-(d) and Fig. 5.8 (c), corresponding orbital areas $S_i = 2\,\pi\,e\,F_i/(\hbar\,c)$, and effective masses from Fig. 5.8

				Rotator						Plastic disk			
	$H \parallel b$				$H \perp b$, Max			$H \perp b$, Min			$H \perp b$		
	MOe	$Å^{-2}$	m_e		MOe	$Å^{-2}$		MOe	$Å^{-2}$		MOe	$Å^{-2}$	m_e
F_1	0.14	0.0013		F_9	0.06	0.00057	F_{15}	0.06	0.00057	F_9^*	0.06	0.00057	0.03
F_2	0.52	0.0050	0.07	F_{10}	0.70	0.0067	F_{16}	0.11	0.0011	F_{10}^*	0.76	0.0073	0.05
F_3	0.65	0.0062	0.08	F_{11}	1.04	0.0099	F_{17}	1.34	0.0128	F_{11}^*	1.06	0.0101	0.05
F_4	0.94	0.0090	0.09	F_{12}	1.12	0.0107	F_{18}	2.46	0.0235				
F_5	1.23	0.0118	0.08	F_{13}	1.51	0.0144	F_{19}	2.72	0.0260	F_{13}^*	1.57	0.015	0.05
F_6	1.47	0.0140	0.08	F_{14}	2.13	0.0203	F_{20}	4.09	0.0391	F_{14}^*	2.13	0.0203	0.06
F_7	2.20	0.0210	0.104										
F_8	4.18	0.0399	0.106										

$M(H)$ data were measured not only at the base temperature, 1.85 K, but also at the several other temperatures, 2.5 K, 3.2 K, 4 K, 5 K, 7 K and 10 K. (Fig. 5.8) For the measurement of these magnetic isotherms, the sample was mounted on a diamagnetic, isotropic, amorphous PCTFE disk and manually rotated with respect to the applied field. Exactly the same peaks that we detected from rotator (Fig. 5.7 (b)) are found when the $H \parallel b$. On the other hand, the FFT data for $H \perp b$ show slightly different peaks compared to both $H \perp b$, Max and $H \perp b$, Min measured from the rotator, although the frequency of the peaks are very similar to that of $H \perp b$, Max, except for F_{12}.

Figure. 5.8 shows that the oscillation amplitudes decrease as temperature increases. The Lifshitz-Kosevich formula [17] explains a phase smearing which is related to amplitude. Specifically, the

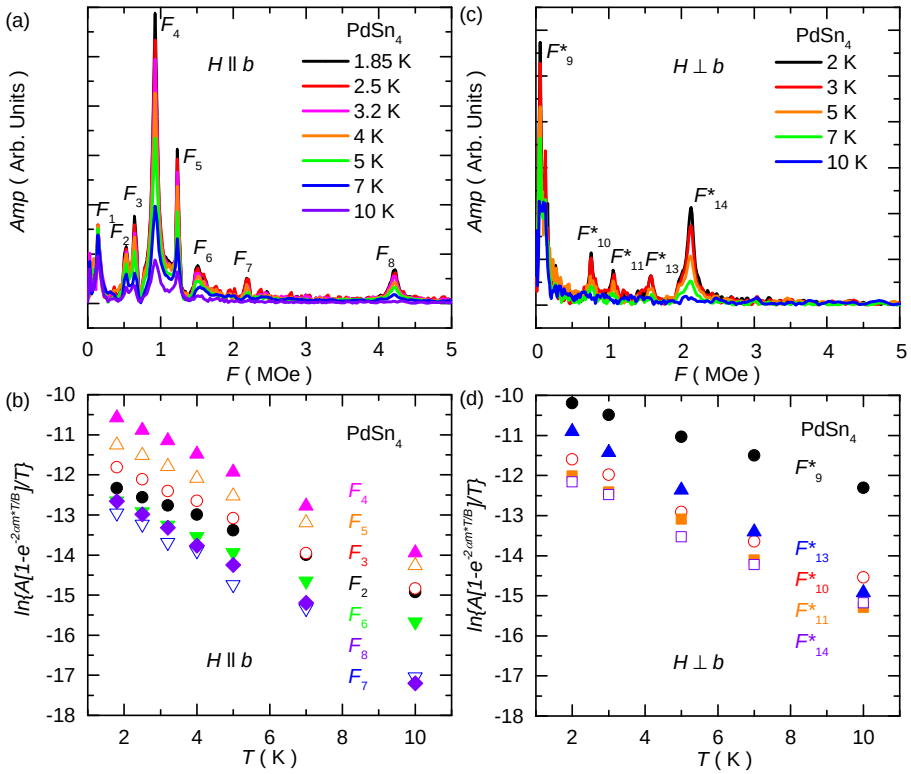

Figure 5.8 (a) Temperature dependence of the fast Fourier transformed dHvA data of $PdSn_4$ for $H \parallel b$ and $T = 1.85\,K$, $2.5\,K$, $3.2\,K$, $4\,K$, $5\,K$, $7\,K$, $10\,K$. (b) Mass plot of dHvA orbits at each frequency when the magnetic field was applied parallel to the crystallographic b-axis. (c) Temperature dependence of the fast Fourier transformed dHvA data of $PdSn_4$ for $H \perp b$ and $T = 2\,K$, $3\,K$, $5\,K$, $7\,K$, $10\,K$. (d) Mass plot of dHvA orbits at each frequency when the magnetic field was applied perpendicular to the crystallographic b-axis.

effect of temperature is described by

$$R_T = \frac{\alpha m^* T/H}{\sinh(\alpha m^* T/H)} \tag{5.4}$$

where $\alpha = 2\pi^2 c k_B/e\hbar$. We used an average value for $1/H = (1/H_{min} + 1/H_{max}) * 1/2$, where H_{min} and H_{max} indicate the range of the data, we used for FFT. Effective masses are obtained based on the above equation, and linear behavior in mass plot in Fig. 5.8 (b) and (d) suggests that the obtained effective masses are reasonable. The effective mass of each frequency is shown in the Table. 5.1. All effective masses are small and approximately equal to each other. However, the low frequency peak, F_9^* has a particularly small effective mass which suggests a potentially large

contribution to density of states. Thus, the carriers confined to the Fermi surface related to the F_9^* may give a dominant contribution to the anisotropy of the magnetic susceptibility.

5.6 Discussion and comparison to $PtSn_4$

The temperature and field dependent properties, including anisotropies, of $PdSn_4$ are qualitatively similar to those of $PtSn_4$, [89] but there exist some important quantitative differences. The question that we now would like to address is whether a comparison of these two, related, materials helps us understand the origin of XMR.

5.6.1 Carrier compensation

Carrier compensation is one of the reasons that many materials, including WTe_2, [9] LaBi, [93] LaSb [93] and $PtBi_2$ [106], are thought to exhibit XMR behavior. However, the scenario of nearly perfect compensation of carriers cannot explain XMR in $PdSn_4$ and $PtSn_4$. At the simplest level, $PdSn_4$ exhibits a larger degree of compensation than $PtSn_4$ but shows a smaller, MR. At low temperatures where MR is large, $PdSn_4$ shows a non-linear field dependence of $\rho_H(H)$ at high field whereas a linear ρ_H is observed for $PtSn_4$ in the high field regime. [89] Note that such non-linear behavior is an indication of carrrier compensation. Moreover, the results from classical two-band-model fitting indicate that $PdSn_4$ has similar electron and hole carrier densities albeit with different mobilities, whereas $PtSn_4$ has an almost two order of magnitude difference between electron and hole carrier densities. [89] (It should be noted, though, that if we consider classical carrier compensation theory, this describes the non-saturating H^2 behavior but not the prefactor.) [12] This means that, in this simplest treatment, the magnitude of MR cannot be explained. For the more specific case of WTe_2 an exitonic insulator was invoked; [9] for $PdSn_4$ and $PtSn_4$ such an insulating state is unlikely given their multiple and complex Fermi surfaces. Finally, a recent theoretical paper studied the compensated Hall effect in confined geometry with electron-hole recombination near the edge, inducing a large MR. [107] In this case, linear response regime is found when the edge currents dominate the resistance. [107] On the other hand, for $PdSn_4$ and $PtSn_4$ we find quadratic behavior

up to 140 kOe. We can thus confidently rule out (i) carrier compensation, (ii) the emergence of an excitonic insulating state, and (iii) MR enhancement by sample confinement as the primary origins of XMR in $PdSn_4$ and $PtSn_4$.

5.6.2 Dirac arc node feature

ARPES measurements were carried out using a laboratory-based tunable VUV laser ARPES system, consisting of a Scienta R8000 electron analyzer, picosecond Ti:Sapphire oscillator and fourth harmonic generator [64] in collaboration with Yun Wu in Adam Kaminski's group. All data were collected with a constant photon energy of 6.7 eV. Angular resolution was set at $\sim 0.05^\circ$ and 0.5° (0.005 Å^{-1} and 0.05 Å^{-1}) along and perpendicular to the direction of the analyzer slit (and thus cut in the momentum space), respectively; and energy resolution was set at 1 meV. The size of the photon beam on the sample was $\sim$30 μm. Samples were cleaved *in situ* at a base pressure lower than 1×10^{-10} Torr. Samples were cleaved at 40 K and kept at the cleaving temperature throughout the measurement.

Band structure with spin-orbital coupling (SOC) in density functional theory (DFT) [108, 109] have been calculated by Lin-Lin Wang with PBE [110] exchange-correlation functional, a plane-wave basis set and projected augmented wave method [111] as implemented in VASP5,6. [112, 113] For bulk band structure of $PdSn_4$, we used the conventional orthorhombic cell of 20 atoms with a Monkhorst-Pack [114] $(8 \times 6 \times 8)$ k-point mesh including the Γ point and a kinetic energy cutoff of 251 eV. The convergence with respect to k-point mesh was carefully checked, with total energy converged below 1 meV/atom. Experimental lattice parameters have been used with atoms fixed in their bulk positions. A tight-binding model based on maximally localized Wannier functions [115, 116, 117] was constructed to reproduce closely the bulk band structure including SOC in the range of $E_F \pm 1$ eV with Pd s and d orbitals and Sn s and p orbitals. Then Fermi surface and spectral functions of a semi-infinite $PdSn_4$ (0 1 0) surface were calculated with the surface Greens function methods [118, 119, 120, 121] as implemented in WannierTools. [122] The $PtSn_4$ data that are shown here for comparison are from our previous paper on $PtSn_4$. [89]

In order to check whether the Dirac arc node feature seen in $PtSn_4$ [88] can be associated with XMR in $PdSn_4$, or not, angle resolved photo emission spectroscopy (ARPES) measurements and surface band structure calculations were performed. The Fermi surface and band dispersion along key directions in the Brillouin Zone (BZ) for $PdSn_4$ are shown in Fig. 5.9. Panel (a) shows the ARPES intensity integrated within 10 meV about the chemical potential. High intensity areas mark the contours of the FS sheets. The FS consists of at least two electron pockets at the center of BZ surrounded by several other electron and hole FS sheets. Fig. 5.9 (b) shows the calculated bulk FS, which matches the ARPES data well close to the center of the zone in Fig. 5.9 (a). However, it does not predict the linear band dispersion near the Z point (see below) or the FS crossings close to the X point, missing a set of curved FS sheets that are present in Fig. 5.9 (a). This is similar to the results of $PtSn_4$, where a surface state calculation was needed to reproduced the Fermi surface sheets observed by ARPES in the proximity of the X point. [88] Thus we carried out a surface spectral function calculation as shown in Fig. 5.9 (c) and we can clearly see extra FS sheets connecting the bands close to the center of BZ and at the X point. Band dispersion along several cuts in proximity of the Z and X points are shown in Figs. 5.9 (d)–(g). Close to the Z point (Figs. 5.9 (d) and (e)), the dispersion resembles a Dirac-like feature. This linear dispersion was not found in bulk calculations and only appeared in the surface spectral function calculations (Figs. 5.9 (h) and (i)). The small gap in the Dirac-like feature at the Z point (Figs. 5.9 (e) and (i)) is reduced to zero for cuts further away from the BZ boundary (Figs. 5.9 (d) and (h)). Close to the X point [Fig. 5.9 (f)], the band dispersion consists of Dirac-like dispersion (surface origin) surrounded by broad hole bands (most likely bulk states). The data agree well with surface spectral function calculation shown in Fig. 5.9 (j). In Fig. 5.9 (g), the observed conduction band and valence band have a significant band gap as marked by the black arrows, which is in agreement with the surface spectral function calculation shown in Fig. 5.9 (k).

The data in Figs. 5.9 (a), (d)–(g) demonstrate that the experimentally observed band structure has both bulk and surface components, and the Dirac-like features near Z and X points have surface origin. Compared to the results of $PtSn_4$ shown in Fig. 5.9 (l), the Fermi surface of these

two compounds are very similar close to the zone center, which is consistent with the similar crystal structures and electronic configurations of the compounds. However, comparing the results in Figs. 5.9 (f) and (g) with those in Figs. 5.9 (m), the primary difference between these two data sets is that for $PdSn_4$, the double Dirac node arcs surface state is gapped out [Fig. 5.9 (g)].

In Fig. 5.10, we show details of the features of $PdSn_4$ near the Z point. An enlarged image from the red box in Fig. 5.10(a) is shown in panel (b), where two triangular-shaped FS sheets make a somewhat disconnected hourglass like shape. The detailed evolution of band dispersions along cuts no. 1 to no. 8 is shown in Fig. 5.10(c). A sharp linear dispersion (the inner band) starts to cross at a binding energy of ∼100 meV in cut no. 1; this band moves up in energy and eventually becomes almost degenerate with the outer bands in cut no. 5. As we move further toward the second BZ cuts(no. 6 – no. 8), the sharp band moves back down in energy, as expected.

A similar study of the band evolution near the X point is shown in Fig. 5.11. We focus on the Fermi surface and band dispersion in a small area in the part of the BZ that is marked by the red box in Fig. 5.11(a). The Fermi surface in this region consists of two parabolic FS sheets intersecting each other, forming two almost parallel straight segments in the overlapping region. Detailed band dispersion along cuts no. 1 to no. 10 are shown in Fig. 5.11(c). The data along cut no. 1 show a sharp electron band enclosed by the bulk intensity. As we move to cut no.2, a Dirac-like dispersion is revealed with the possible Dirac point marked by the red arrow. Moving closer to the X point (cut no. 3), we can see a gap develops between the conduction and valence bands, and another electron band emerges. As we move to cuts no. 4, 5, and 6, the two electron bands come closer and eventually merge together in cut no. 6 at the X point. A significant gap between the conduction and valence bands persists across these cuts. The gap size slowly decreases and seems to form another Dirac dispersion in cut no. 10 in the second BZ. The observed features around X point are markedly different for $PtSn_4$, [88] where gapless Dirac node arc structure is observed.

Even though, in $PdSn_4$ the Dirac point at Z is a surface state and the Dirac arc node feature is gapped out, XMR behavior is still present in both compounds. Moreover, both $PdSn_4$ and $PtSn_4$ show larger MR when the magnetic field is applied perpendicular to the b direction. This is

not consistent with the measured surface states at a surface perpendicular to b giving rise to the measured XMR, because the resulting orbits do not lie in the surface plane.

5.6.3 Kohler's rule

Let us now investigate whether a classical description of the electronic motion can give insight into the MR results. The well-known Kohler's rule states that the change of resistivity $\Delta\rho$, where $\Delta\rho = \rho(T,H) - \rho_0$ and where $\rho_0 \equiv \rho(T, H = 0)$, under the magnetic field H can be described as a scaling function of the variable $H\tau$. [123] Here, τ is the mean time between scattering events of conduction electrons, and it is inversely proportional to ρ_0. Such a scaling behavior expresses a self-similarity of the electronic orbital motion across different length scales: an invariance of the magnetoresponse under the combined transformation of shrinking the orbital length $L \sim 1/H$ by increasing H while at the same time also increase the scattering rate $1/\tau$ by the same factor such that $H\tau$ remains unchanged, indicates that the system behaves identical on different length scales. The formula for the Kohler's rule can be written as follows with scaling function $F(x)$.

$$\Delta\rho/\rho_0 = F(H/\rho_0) \tag{5.5}$$

It should be appreciated that Kohler's rule is both powerful and simplified; Kohler's rule scaling breaks down if different scattering mechanisms emerge on different temperature or lengthscales or if Landau orbit quantization plays a role. [11]

In Figs. 5.12 and 5.13 we plot MR data for $PdSn_4$ and $PtSn_4$ respectively as $\Delta\rho/\rho_0$ Vs. H/ρ_0 on a log-log scale. In Fig. 5.12, for $PdSn_4$ we plot MR data, for two field directions, extracted from two different extremes of MR sweeps: $\rho(T = 1.8\,\mathrm{K},\ 500\,\mathrm{Oe} \leq H \leq 140\,\mathrm{kOe})$ and $\rho(1.8\,\mathrm{K} \leq T \leq 300\,\mathrm{K},\ H = 140\,\mathrm{kOe})$. Remarkably although the two data sets, lie in very different field and temperature regimes, they fall precisely on top of each other on a sigmoidal-shaped curve. These plots demonstrate that the behavior of all of the MR data for $PdSn_4$, from 1.8 K to 300 K, from 0 Oe to 140 kOe is captured and described by a Kohler's rule. Figure 5.13 shows the same generalized Kohler's plot for MR data collected on $PtSn_4$. [89] We find that all of the $\rho(T, 500\,\mathrm{Oe} \leq$

$H \leq 140\,\mathrm{kOe}$) data for temperatures ranging from 1.8 K all the way up to 300 K fall onto similar sigmoidal-shaped curves.

The importance of the such complete MR data collapse in Figs. 5.12 and 5.13 cannot be over emphasized. In Fig. 5.12, for $PdSn_4$, we find precisely the same behavior at 1.8 K as we so for temperatures ranging up to 300 K. The two very different cuts through T-H phase space yield the same Kohler's rule curve. This means that the behavior of the MR at 1.8 K is governed by the simple physics as the behavior at 300 K; i.e. there is not a metal-to-insulator transition or other such feature associated with the local minima in the $\rho(T)$ data for any given applied field. Instead, given that a generalized form of Kohler's rule describes the $PdSn_4$ and $PtSn_4$ data exceptionally well, any features that are seen in the $\rho(T, H)$ data in the low temperature/high field limit originate from the same physics that gives rise to the high temperature/low field behavior.

This generalized Kohler's rule analysis, of course, raises the question of what is the origin of the sigmoidal-shape we find for both $PdSn_4$ and $PtSn_4$? In both Figs. 5.12 and 5.13 there is a well defined, linear, high field/low temperature (upper right hand corners of the plots) region that can be associated with power law behavior. As either temperature is increased or field is lowered the curvature associated with the sigmoidal-shape appears and grows. It is possible, even likely, given the clear dHvA oscillations, that the high magnetic field (or low temperature) regime is where $\omega_c\tau > 1$. Conversely, high temperatures and low magnetic field will be where $\omega_c\tau < 1$. It should be noted that large MR can be expected only when $\omega_c\tau \gg 1$. [11] For both $PtSn_4$ and $PdSn_4$ the middle of the sigmoidal region of the curves occur for $\Delta\rho/\rho_0 \sim 1$; this may provide a physical sense of, or criterion for, $\omega_c\tau \gg 1$.

We can use the Kohler's rule data shown in Fig. 5.13 (a) to delineate the low temperature/high field part of the T-H phase space from the high temperature/low field part. In Fig. 5.13 (c) we plot data inferred from (i) the deviation from high field/low temperature linear behavior in the upper right part of Fig. 5.13 (a), and (ii) the position of the inflection point associated with the sigmoidal-shaped curve. These data provide an estimate of the extent of the high field/low temperature region for this specific $PtSn_4$ sample. We can also use the local minima in the $\rho(T)$ data measured

for a constant applied magnetic field to define a set of (T,H) data points. We include these data in Fig. 5.13 (c) as well; they clearly are associated with crossing over from a low temperature limit to a high temperature limit in terms of $\omega_c\tau$.

The challenge that $PdSn_4$ and $PtSn_4$ present is to understand what specific feature of their band structure is responsible for the remarkable size of the MR that is observed. This still unresolved point is what makes research into these compounds, as well as other XMR materials a compelling topic for ongoing research.

5.7 Conclusion

In conclusion, the thermodynamic and transport properties of $PdSn_4$ are strikingly similar to those of $PtSn_4$; both compounds have closely related temperature dependent specific heat, anisotropic resistivity and magnetization, although the precise magnitudes of RRR and MR are quantitatively different. We have focused on the origin of XMR in these two materials. Based on our analysis, we can rule out carrier compensation and the surface state Dirac arc node features observed in $PtSn_4$ can be considered as key reasons for the XMR. Instead, we find that, by using a generalized Kohler's plot, all of the MR data for both $PdSn_4$ and $PtSn_4$ collapse onto simple sigmoidal manifolds. For $PdSn_4$, the fact that MR data from an isothermal field sweep at 1.8 K and a constant field (140 kOe) temperature sweep from 1.8 K to 300 K fall indistinguishably on top of each other (with similar results for $PtSn_4$) clearly emphasizes that the behavior of the MR data for these materials is captured by the basic metal physics encoded into Kohler's rule. A future challenge is to identify the specific properties of $PdSn_4$, $PtSn_4$ and other XMR compounds that give rise to the remarkable size and durability of the observed XMR.

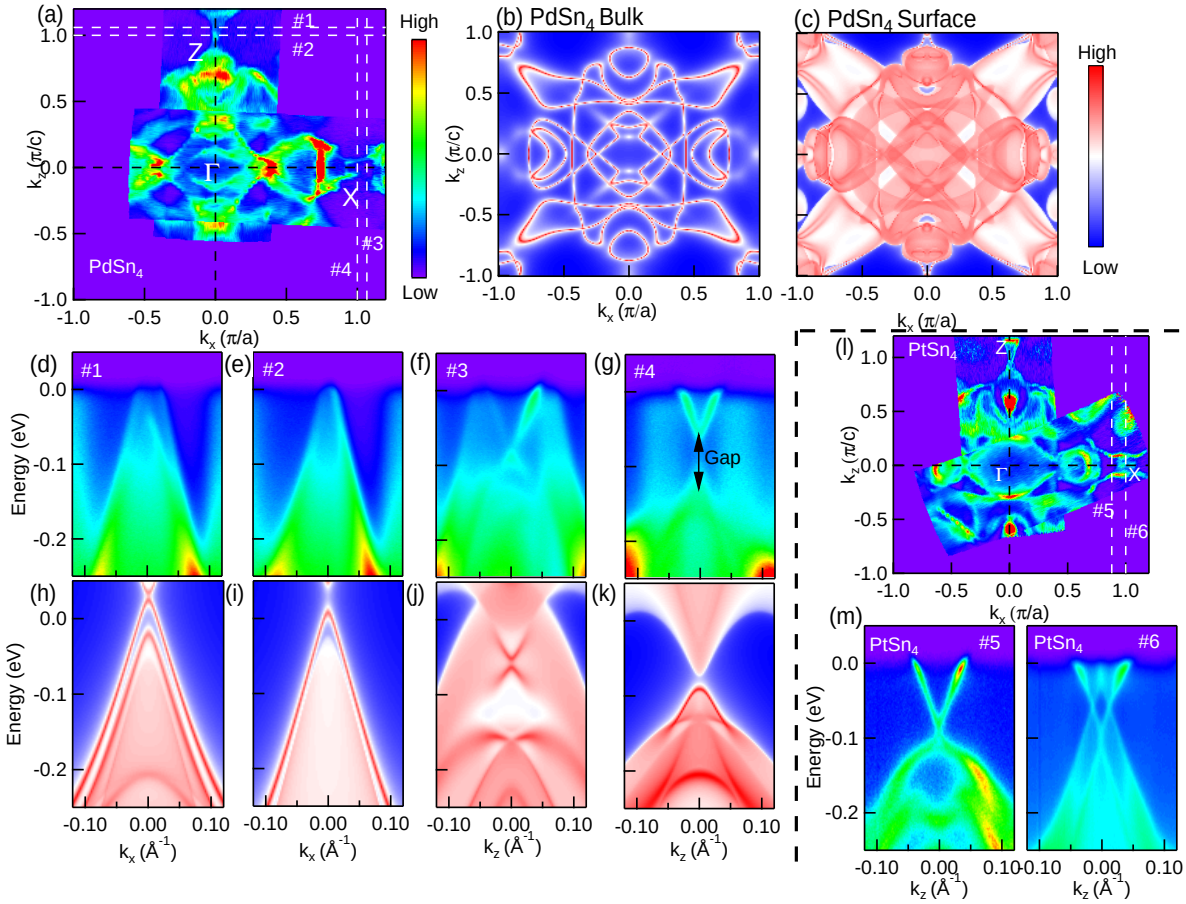

Figure 5.9 Experimental ARPES and calculated results for the electronic Fermi surface and band dispersion of $PdSn_4$. (a) Fermi-surface plot of ARPES intensity integrated within 10 meV of the chemical potential along $\Gamma - Z$ and $\Gamma - X$. (b) Bulk FS calculated by density functional theory (DFT) at $k_y = 0.364\ \pi/b$. (c) Calculated surface FS. (d)-(g) ARPES band dispersions along cut #1-#4 in (a), respectively. (h)-(k) Calculated surface band dispersion corresponding to (d)-(g). (l) For comparison, Fermi-surface plot of ARPES intensity integrated within 10 meV of the chemical potential along $\Gamma - Z$ and $\Gamma - X$ in $PtSn_4$. [88] (m) Band dispersion in $PtSn_4$ at $k_x = 0.88$ and $1.0\ \pi/a$ along cut #5 and 6 in (l). [88]

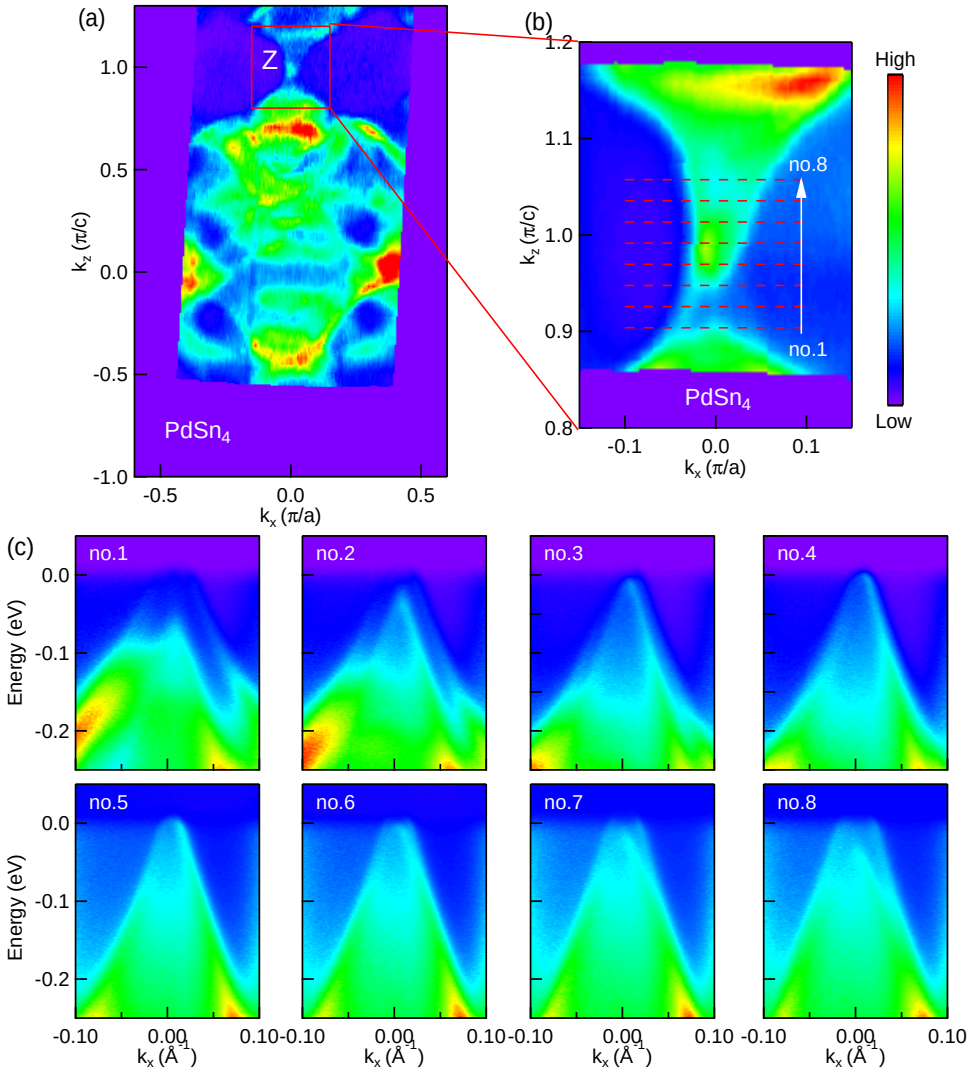

Figure 5.10 Fermi surface and band dispersion in the proximity of the Z point,(0,1), of $PdSn_4$. (a) Fermi surface plot of the ARPES intensity integrated within 10 meV of the chemical potential along $\Gamma - Z$. (b) Zoomed image of the red box in (a), red dashed lines mark cuts no.1 - no.8. (c) Band dispersion along cuts no. 1 - no. 8. Cut no. 5 passes through the Z point.

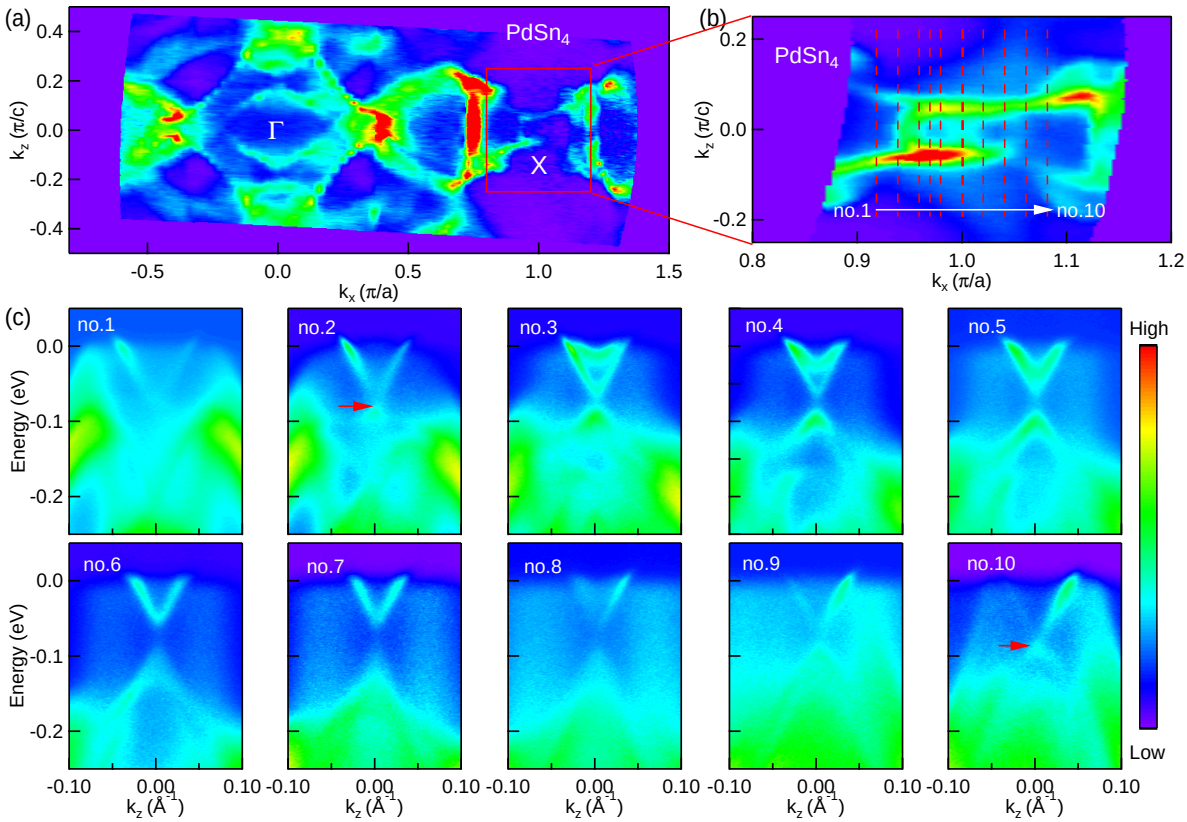

Figure 5.11 Fermi surface plot and band dispersion close to the X point, (1,0), of $PdSn_4$. (a) Fermi surface plot of the ARPES intensity integrated within 10 meV of the chemical potential along $\Gamma - X$. (b) Zoomed image of the red box in (a), red dashed lines mark cuts no.1 – no.10. (c) Band dispersion along cuts no.1 - no.10. Cut no. 6 passes through the X point.

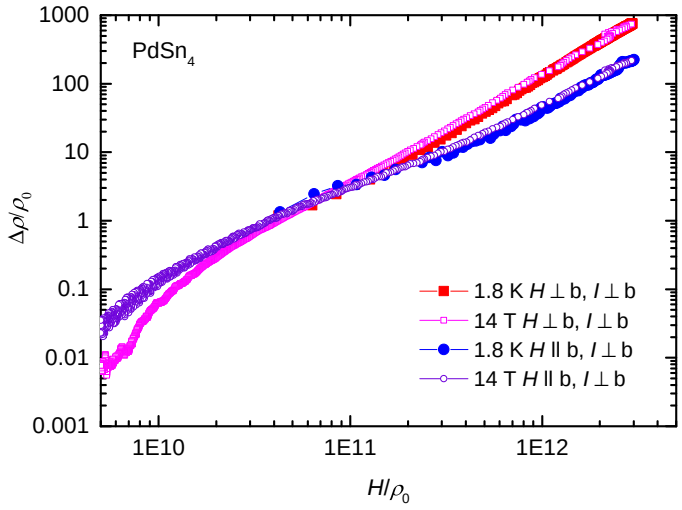

Figure 5.12 Kohler's plot of $PdSn_4$ magnetoresistance data. Red filled squares are based on $\rho(H)$ data taken at 1.8 K.($H \perp b$, $I \perp b$) Magenta open squares are based on $\rho(T)$ data taken under the magnetic field of 140 kOe. ($H \perp b$, $I \perp b$) Blue filed circles are based on $\rho(H)$ data taken at 1.8 K.($H \perp b$, $I \parallel b$) Purple open circles are based on $\rho(T)$ data taken under the magnetic field of 140 kOe.($H \perp b$, $I \parallel b$)

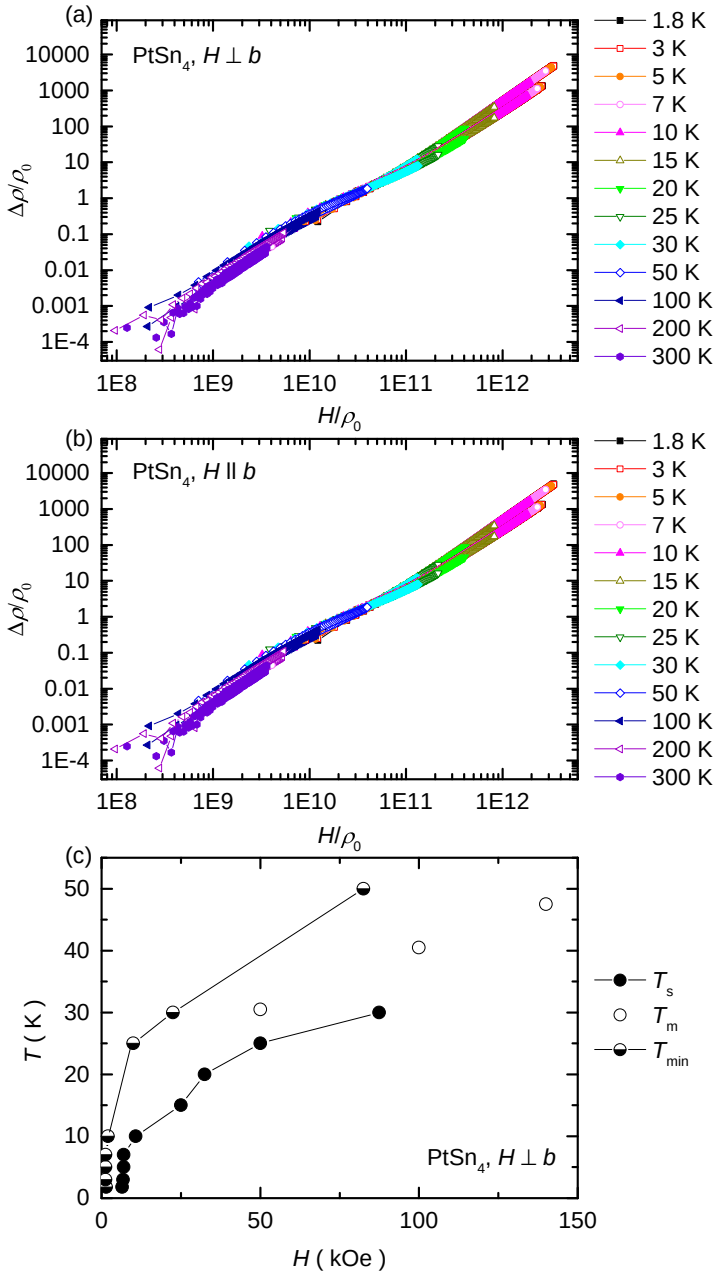

Figure 5.13 Kohler's plot of $PtSn_4$ magnetoresistance data with various temperatures; 1.8 K, 3 K, 5 K, 7 K, 10 K, 15 K, 20 K, 25 K, 30 K, 50 K, 100 K, 200 K, 300 K with two different magnetic field directions from Ref. [89] (a) $H \perp b$ and (b) $H \parallel b$. (c) Temperature-field phase diagram for $PtSn_4$ for $H \perp b$. Filled black circles are the starting point of the Kohler's rule slope change in (a) in the high magnetic field regime. Open black circles are the temperature of the local minimum in $\rho(T)$ data for an applied magnetic field of 50, 100 or 140 kOe. Half filled circles are the shallowest slope in the Kohler's plot in (a).

CHAPTER 6. PHENOMENAL MAGNETORESISTANCE AND MAGNETOELASTORESISTANCE OF WTe_2

The following context is a slightly modified version of the published work in Ref. [24, 124] and arXiv:1901.05090, (2019). [125]

DOI: http://dx.doi.org/10.1103/PhysRevLett.115.166602 and http://dx.doi.org/10.1103/PhysRevB.95.195138.

6.1 Ambient condition transport and thermal-transport properties of WTe_2

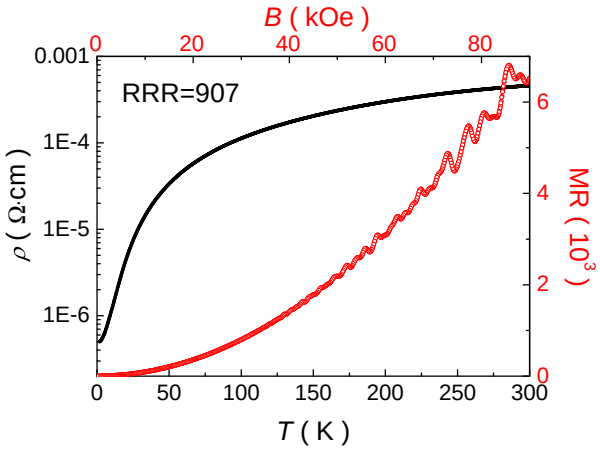

Figure 6.1 Temperature dependent resistivity with left and bottom scale in black color and MR with right and top scale in red color.

Whereas single crystals of WTe_2 had been to grown via chemical vapor transport using halogens as transport agents, [9, 40] we grew WTe_2 single crystals from a Te-rich binary melt. Elemantal W and Te were placed in alumina crucibles in W_1Te_{99} and W_2Te_{98} ratios. The crucibles were

sealed in amorphous silica tubes and the ampoules were heated to 1000 °C over 5 hours, held at 1000 °C for 10 hours, then slowly cooled to 460 °C over 100 hours, and finally decented using a centrifuge. Details about the single crystal growth of WTe_2 can be found in the method chapter, subsection 3.1.1. Interestingly, single crystals of WTe_2 grown via solution growth method show higher residual resistivity ratio (RRR) and magnetoresistance (MR) values than the ones grown via chemical vapor transport. [90] For instance, the first paper [9], that reported XMR behavior in WTe_2, used the chemical vapor transport method to growth the single crystals. They observed a RRR value of 370 and a MR value of 1730 (at $B = 9\,\mathrm{T}$). On the other hand, we observed RRR value of 907 and MR value of 6500 (at $B = 9\,\mathrm{T}$) with our solution growth sample as shown in Fig. 6.1. Later Ref. [90] further codified the correlation between RRR and MR ratio as well as relation between RRR and growth methods.

Owing to this high quality crystal, we were able to study transport and thermal-transport properties in detail.

6.1.1 Three-dimensionality of the bulk electronic structure in WTe_2

Figure 6.2 (a) shows that the MR has a parabolic behavior without any saturation for fields up to 14 T. In order to analyze the quantum oscillation spectra, we subtracted the background using a second-order polynomial function to fit the background MR in the range of $6\,\mathrm{T} \leq H \leq 14\,\mathrm{T}$ for all temperatures. The oscillations show periodic behavior in $1/H$, as shown in Fig. 6.2 (b).

The frequencies of the oscillation were obtained by FFT analysis, as shown in Fig. 6.2 (c). Five frequencies, including $F^1 = 92\,\mathrm{T}$, $F^2 = 132\,\mathrm{T}$, $F^3 = 152\,\mathrm{T}$, $F^4 = 172\,\mathrm{T}$, and $F^5 = 264\,\mathrm{T}$, are similar to published results. [24, 126, 127] F^5 is thought to be due to the magnetic breakdown between F^1 and F^4, as suggested in Ref. [24]. Interestingly, a new, low-frequency peak, $F^* = 10\,\mathrm{T}$, is also clearly observed in our data. In order to make sure that it is not an artifact from background subtraction, we did FFTs of the data over three different magnetic field windows: 4 T - 14 T, 5 T - 14 T, and 6 T - 14 T. In all cases, we found the low-frequency peak, F^*. The amplitude of the F^* decreases with increasing temperature, as shown in Fig. 6.2 (d). Note that for sake of consistency the exact same

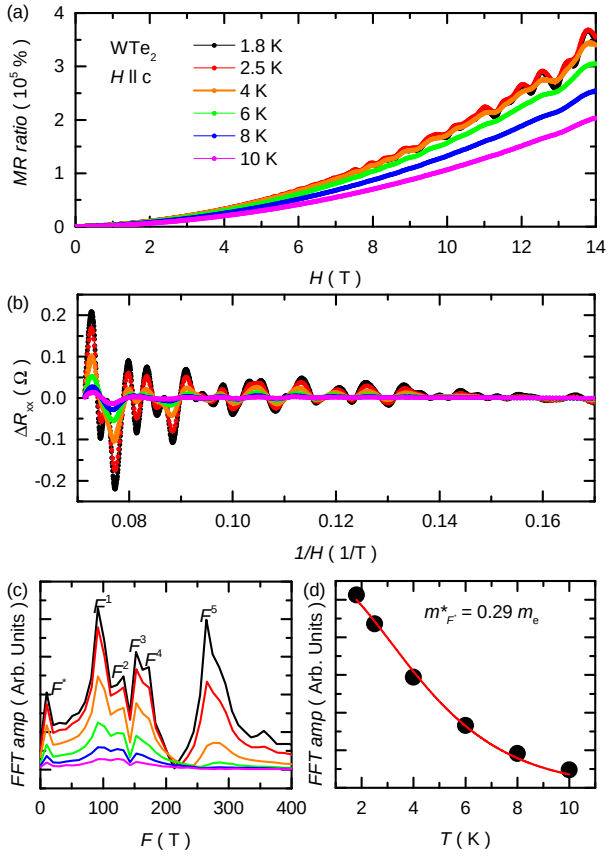

Figure 6.2 (a) Magnetoresistance measured at $T = 1.8\,\mathrm{K}$, $2.5\,\mathrm{K}$, $4\,\mathrm{K}$, $6\,\mathrm{K}$, $8\,\mathrm{K}$, and $10\,\mathrm{K}$. (b) Shubnikov-de Haas oscillation after subtracting a monotonic second order polynomial fit for background. (c) FFT analysis of quantum oscillations. (d) Temperature dependence of the oscillations amplitude as a function for the peak, F^*. The closed circles are the data, and solid line is the fitted line of Lifshitz-Kosevich formula.

data acquisition and processing protocol were followed for all temperatures. The observed decrease of the oscillation amplitude is due to the temperature-induced scattering of electrons, described by the Lifshitz-Kosevich formula. (As described in Sec. 2.3) Using this formula, we calculated the effective mass of the carriers linked to the oscillation frequency F^*, $m^*_{F^*} = 0.29 \pm 0.01\, m_e$. Note that we used an average value for $1/B$, $1/B = (1/B_{max} + 1/B_{min})/2$; this might give a certain error in our effective mass of F^* due to the Dingle envelope.

To match this small frequency observed in quantum oscillation to a specific Fermi surface, we carried out photon-energy-dependent ARPES measurements with the collaboration with Yun Wu in Adam Kaminski's group. These results are published in Ref. [124]. The photon energy dependence measurements with relatively fine energy steps have revealed the three-dimensional character of the electron and hole pockets along the Γ-Z direction. With the increase of the incident photon energy from 5.77 to 6.70 eV (i.e., probing along k_z direction), we have observed that the hole pocket expands and then shrinks, while the electron pocket displays opposite behavior. Strong photon energy dependence is also observed in the hole bands at the Γ point. Furthermore, at the photon energy of 6.36 eV we have revealed a pair of tiny electron pockets sitting at the opposite side of the Γ point, providing strong support for the low quantum oscillation frequency peak that was not accounted for in the previous studies. [24, 127] It should be noted that the details of the band structure calculation depend critically on small changes of parameters of the crystal structure, especially precise ionic positions, and equally important model approximations used in computations. We hope that the observation of extra electron pockets will be used by experts to analyze the approximations of the band structure calculations and improve the algorithms used for WTe_2 and related materials.

6.1.2 Temperature induced Lifshitz transition in WTe_2

We performed temperature dependent TEP and Hall effect ($B = 9$ T) measurements as shown in Fig. 6.3. In particular, the temperature dependence of the TEP in Fig. 6.3 (a) shows two features that are noteworthy: (i) a nonmonotonic dependence of the TEP on temperature with a local maximum at 30 K and (ii) a kink at $T \sim 160$ K marked by an arrow in the inset of Fig. 6.3 (a) observed in the rate of change of the TEP $\mathrm{d}S/\mathrm{d}T$ as a function of temperature. Similarly, Hall data at $B = 9$ T shows the two features: (i) a huge drop of ρ_H/B below 50 K and (ii) a slope change or local minimum in between 150 K and 200 K. Note that, Hall resistivity, ρ_H, was measured using a four probe method, in positive (ρ_{+H}) and negative (ρ_{-H}) magnetic field and was calculated as $\rho_H = (\rho_{+H} - \rho_{-H})/2$ to separate odd in field ρ_H from possible contamination of the even in field

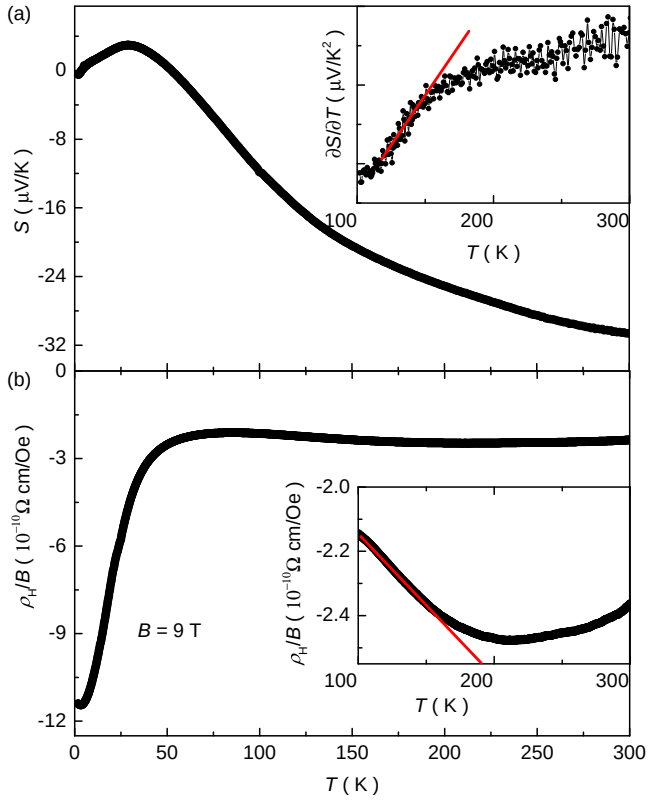

Figure 6.3 (a) Temperature dependence of TEP. Inset shows first derivative with a red linear line marking the change of slope due to Lifshitz transition. (b) Temperature dependence of ρ_H/B at $B = 9\,\mathrm{T}$. Inset shows enlarged ρ_H/B data between 100 and 300 K with a red linear line marking the change of slope due to Lifshitz transition.

magnetoresistance. More detail can be found in the subsection 3.2.3. We also noticed that the here-reported feature in TEP occurs at very similar temperature to one where the large MR is suppressed.

The temperature and field dependence of the extraordinarily large MR of WTe_2 are shown in Fig. 6.4 inset as well as Fig. 6.2. The generalized Kohler's plot shows that there is fairly good scaling of the data with an exponent of ~ 1.98 at lower temperatures. As the temperature is increased, Kohler's scaling breaks down, as was also previously suggested, [98] at the H/ρ_0 indicated by the vertical arrow in Fig. 6.4; at this point temperatures range from 70 to 140 K for scans at different

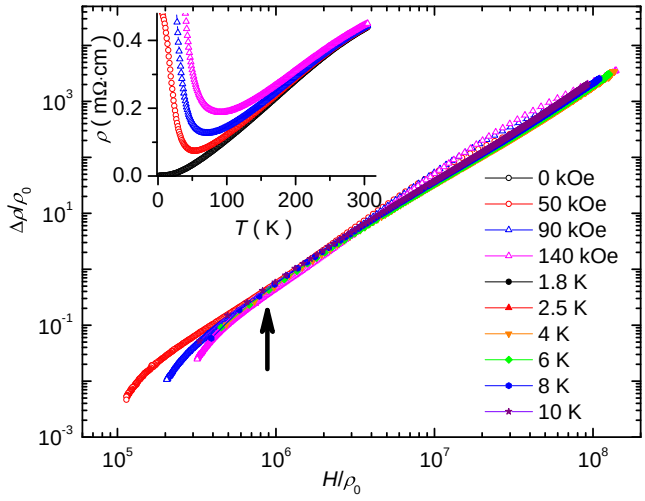

Figure 6.4 Generalized Kohler plot. Arrow marks the point below which the Kohler rule is violated ($T > 60\,\mathrm{K}$). Inset shows temperature dependence of the resistance measured for magnetic field of 0, 50, 90, and 140 kOe.

fields. We now proceed to elucidate the electronic origin of the change of the slope of the TEP and Hall effect, and violation of Kohler's rule.

To understand the anomalies in transport and thermal-transport, we conducted temperature dependent ARPES measurement in the collaboration with Yun Wu in Adam Kaminski's group and electronic structure calculation by Nandini Trivedi and Ryotaro Arita group. This result is published in Ref. [24]. By correlating spectroscopic studies with electronic structure calculations, we found that the chemical potential can be temperature dependent in semimetallic materials such as WTe_2, which in turn can strongly affect their magnetotransport properties [9] by driving a Lifshitz transition. Such shifts in μ with temperature were previously reported in pnictides high-temperature superconductors, [128, 129] where both electron and hole pockets were found in close proximity to the chemical potential. The mechanisms described here, the presence of small electron and hole pockets, strong chemical potential shifts, and Lifshitz transitions, are likely to be relevant for other systems, such as 3D Dirac semimetals, Weyl semimetals, and thermoelectric materials. In the presence of interactions, the restructured Fermi surfaces could change the nesting conditions

and drive various magnetic, charge ordered, and superconducting transitions in these classes of dichalcogenide and related materials.

6.2 Strain engineering of electronic and quantum transport properties of WTe_2

Elastoresistance describes the relative change of a material's resistance when strained. It has two major contributions: strain induced geometric and electronic changes. If the geometric factor dominates, like in ordinary metals such as copper, the elastoresistance is positive and rather small, i.e. typically of order 1. [30] In a few materials, however, changes in electronic structure dominate, which gives rise to larger and even negative values, such as (-11) for Bi. [130] Here, we present that the transition metal dichalcogenide (TMDC) WTe_2 is a member of the second group, exhibiting a large and non-monotonic elastoresistance that is about (-20) near 100 K and changes sign at low temperatures. We discover that an applied magnetic field has a dramatic effect on the elastoresistance in WTe_2: in the quantum regime at low temperatures, it leads to quantum oscillations of the elastoresistance, that ranges between (-80) to 120 within a field range of only half a Tesla. In the semiclassical regime at intermediate temperatures, we find that the elastoresistance rapidly increases and changes sign in a magnetic field. We provide a semi-quantitative understanding of our experimental results using a combination of first-principle and analytical low-energy model calculations. Understanding bulk properties of TMDCs under uniaxial strain is an important stepping stone toward strain engineering of 2D TMDCs.

The majority of TMDCs have layered structures, which can be easily exfoliated, due to van der Waals bonding between chalcogenides layers. [131] This low dimensionality, as well as novel electronic transitions and properties, led to studies of the effects of hydrostatic pressure on these materials. As a result, superconductivity was often found upon suppression of charge density wave (CDW) by applying pressure to TMDCs such as TaS_2, $TaSe_2$ and 2H-$NbSe_2$. [4] Another particularly striking example is WTe_2, which displays the fascinating behavior of extremely large magnetoresistance (XMR) [9, 89] at low pressures and superconductivity at higher pressures. [21]

The tunability of TMDCs by hydrostatic pressure, combined with their low dimensionality, suggests that uniaxial strain might be another powerful tuning parameter. Despite the importance of strain for thin films and device applications, a systematic experimental study of the response of bulk TMDCs to continuously controlled strain is still lacking. In addition, first-principle calculations have emphasized that strain can be employed to tune electronic characteristics of TMDCs such as band gap, charge carrier effective masses, thermal conductivity, dielectric properties and spin-orbit coupling. [4] In this section, we demonstrate that WTe_2 has phenomenal elastoresistance that is highly tunable by an external magnetic field. We employ a combination of quantum oscillation, first-principle density functional theory [108, 109] (DFT) and analytical low-energy model calculations to elucidate the physical origin of this novel "magneto-elastoresistance (MER)" phenomenon. Our analysis provides new insights into the interplay of elastic and electronic degrees of freedom in WTe_2 that will facilitate strain engineering of electronic properties of TMDCs in the future.

WTe_2 can be considered as a pseudo-1D structure [131] with distorted zig-zag chains of W atoms running along the a direction. We therefore applied uniaxial strain on bulk single crystals of WTe_2 along the crystallographic a direction as shown in Fig. 6.5 (a) and (b). We observe that the elastoresistance of WTe_2, with both strain and electric current directed along the a direction, is very large. It reaches (-20) around a temperature of 100 K (Fig. 6.5 (c)). This value is too large to arise from purely geometric changes, considering a Poisson ratio of 0.16. [132] The elastoresistance properties of single crystals of WTe_2 are thus clearly governed by the strain induced electronic changes. Interestingly, we observe a non-monotonic behavior of elastoresistance that exhibits a rapid increase around 35 K leading to a sign change at low temperatures. As shown below, this behavior can be understood within a low-energy model calculation as arising from a strain-induced redistribution of carriers among electron and hole pockets with different effective masses.

WTe_2 is well-known for its XMR at low temperature. As seen in Fig. 6.6 (a), the resistance exhibits a large increase in an applied magnetic field. As shown in Fig. 6.6 (b), the temperature dependent elastoresistance also shows a pronounced response to an applied magnetic field. Remarkably, in the quantum regime, at temperatures $T < 12$ K, the elastoresistance changes dramatically

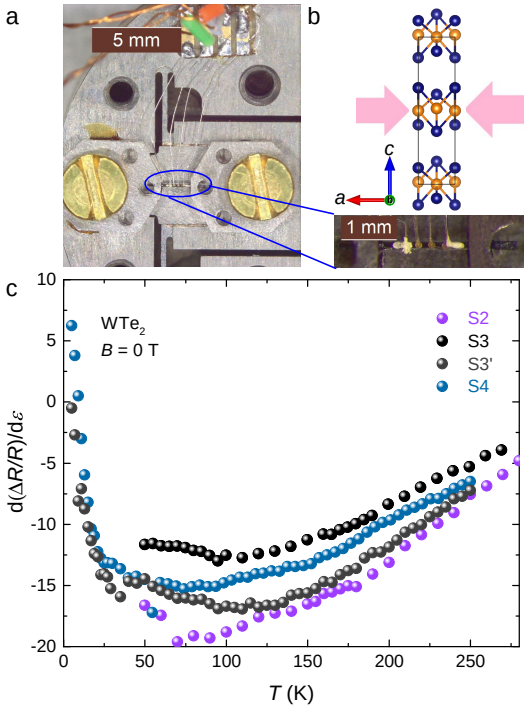

Figure 6.5 (a) A single crystal of WTe_2 is mounted on Razorbill CS100 cryogenic uniaxial strain cell. The electrical current and mechanical stress was applied along the crystallographic a direction, and the magnetic field was applied along the crystallographic c direction. (b) Crystal structure of WTe_2. (c) Elastoresistance of WTe_2 in the temperature range of $5\,\mathrm{K} \leq T \leq 270\,\mathrm{K}$ with $B = 0\,\mathrm{T}$ for samples S2, S3, S3' and S4. All samples exhibit a large, negative elastoresistance at not too low temperatures. S3 and S4 show a pronounced upturn at low temperatures $T \leq 25$ K. Quantitative differences between samples can be due to a difference in quality and/or strain transmission through the sample.

with relatively small changes in the magnetic field. The inset of Fig. 6.6 depicts the low-T elastoresistance for $B = 13.1\,\mathrm{T}$, $13.6\,\mathrm{T}$ and $14.0\,\mathrm{T}$. Over this relatively small field range, the elastoresistance varies from 120 to (-75) and back to 50. We show below that such newly observed elastoresistance quantum oscillations occur due to strain tuning of Shubnikov-de Haas (SdH) oscillations (see SI for more detail). Furthermore, at low to intermediate temperatures (e.g. $T = 15\,\mathrm{K}$), the elastoresistance changes abruptly as a function of magnetic field from (-10) to (+20) and eventually saturates. Figure 6.6 (c) shows a three dimensional plot of the elastoresistance. To avoid the effects of quantum oscillation at the lowest temperatures, we focus on the MER at $15\,\mathrm{K}$ which is highlighted in

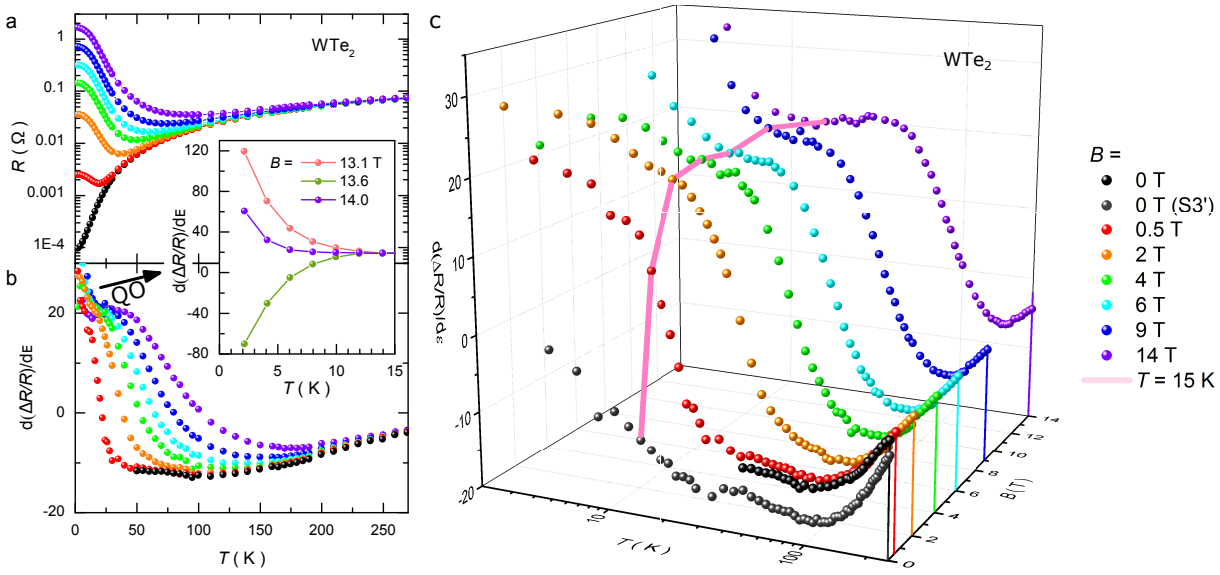

Figure 6.6 (a) Resistance of sample S3 as a function of temperature for various magnetic fields, $H = 0, 0.5, 2, 4, 6, 9, 14$ (in units of T). The legend is shown on the right. The field is applied along the crystallographic c direction. (b) Elastoresistance of sample S3 as a function of temperature in the same magnetic fields H. Inset shows elastoresistance in the low temperature regime ($2\,\mathrm{K} \leq T \leq 15\,\mathrm{K}$) with an applied magnetic field of 13.1 T, 13.6 T and 14 T. (c) Three-dimensional representation of MER data from panel (b) including $H = 0$T data of sample S3'. The pink line connects the data at $T = 15\,\mathrm{K}$, highlighting the rapid increase and eventual saturation of MER in magnetic field.

pink. At this temperature, the elastoresistance changes rapidly below 0.5 T, and then saturates above 2 T. This behavior can be readily captured by semiclassical transport calculations, which we will discuss in detail below (and in the SI). Importantly, this discussion shows that measuring MER provides new insights into the strain response of a material (beyond the zero field elastoresistance) as it it probes different strain derivatives. For example, it allows us to infer that the sign change of the elastoresistance in zero field arises from strain tuning of the carrier densities as opposed to tuning of effective masses and scattering rates.

To understand the effect of strain on the electronic properties of WTe_2 such as the carrier's effective masses m^* or the cross-sections of extremal orbits on the Fermi surface (FS) (perpendicular to an applied magnetic field), we measure SdH oscillations and use DFT band structure calculations.

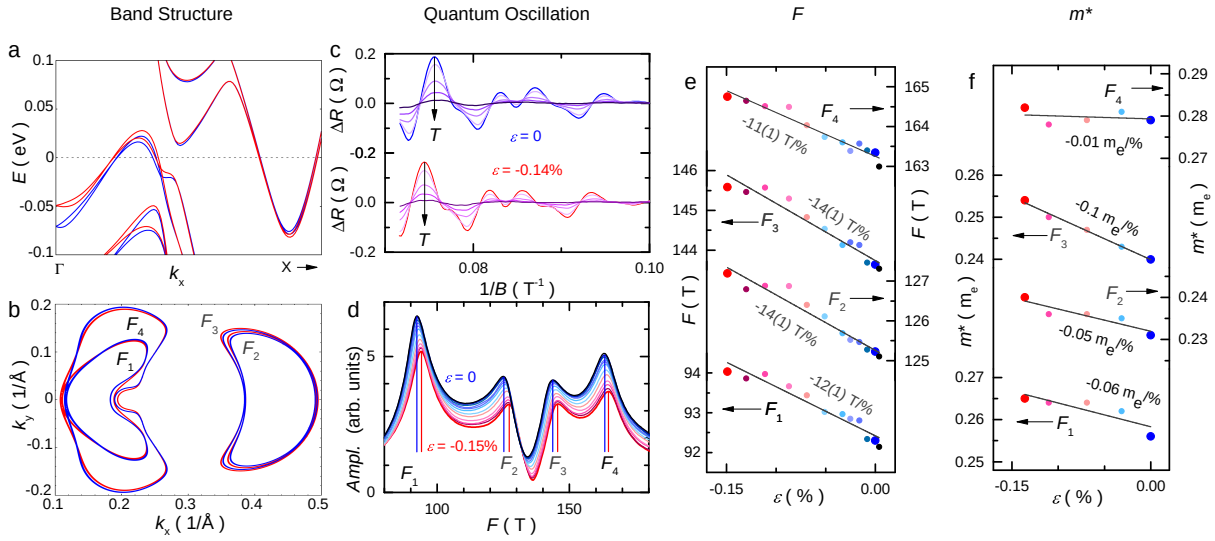

Figure 6.7 (a) Results of DFT band structure calculation along the Γ - X direction without strain ($\epsilon = 0\%$, blue) and with strain ($\epsilon = -0.2\%$, red). (b) Strain induced modification of extremal orbits at $k_z = 0$ from DFT calculation. Blue and red lines refer to the same strain as in panel (a). Fermi surfaces F_1 and F_4 correspond to hole bands and F_2 and F_3 to electron bands. (c) Experimental results for Shubnikov-de Haas (SdH) quantum oscillations after subtracting the background at temperatures $T = 2, 3, 5, 7 and 10$ K. Upper panel is for ϵ = 0 % and lower panel is for ϵ = -0.14 %. (d) Fast Fourier transformation (FFT) results at various strains. Blue lines indicate the frequencies at zero strain and red lines are located at the frequencies at -0.15 % strain. (e) SdH oscillation frequencies of the four extremal orbits $F_{1,2,3,4}$ as a function of strain ϵ. The numerical values of the slopes are given in the figure. (f) Effective cyclotron masses of the four extremal orbits $F_{1,2,3,4}$ as a function of strain with slopes given in the figure.

Figure 6.7 (a) shows DFT calculations on WTe_2 without and with strain. Given that the curvature of a band at the Fermi level relates to the effective mass of the charge carrier, one can see that the effective masses change as strain is applied. In addition, the FS areas enclosed by extremal orbits [133] in the k_x-k_y plane at $k_z = 0$ also vary as a function of strain as shown in Fig. 6.7 (b).

The changes of the extrema FS area and the effective (cyclotron) masses can be experimentally inferred from analyzing SdH oscillation frequencies and their amplitudes as a function of temperature. After subtracting a quadratic background, the residual oscillatory parts of resistance, with

and without stain, are plotted as a function of $1/B$ in Fig. 6.7 (c). In order to quantify the FS changes, a Fast Fourier Transform (FFT) was taken in Fig. 6.7 (d). All four frequencies shift to higher values when the sample is compressed. Since the frequency is related to the extremal orbit of the FS via the Onsager relation, $F_i = \frac{\hbar c}{2\pi e} S_i$, [11] these positive shifts indicate enlarged extremal FS orbits. Figure 6.7 (e) shows a linear dependence of frequency on strain. Figure 6.7 (c) also shows that the amplitude of the SdH oscillation decreases with increasing temperature. Such a tendency allows us to extract the effective masses by fitting with Lifshitz-Kosevich (LK) theory, $R_T = \frac{\alpha m^* T/H}{\sinh(\alpha m^* T/H)}$, [11] where $\alpha = 2\pi^2 c k_B/e\hbar$. Figure 6.7 (f) demonstrates that all masses increase with compressive strain, even though the magnitude of changes is different, in agreement with our DFT predictions.

To interpret our MER measurements, we employ an effective low-energy model that can account for the salient experimental features. Using input from DFT calculations as well as ARPES and quantum oscillations measurements, our minimal low-energy model consists of three parabolic bands (see Fig. 6.8): one electron pocket with effective mass m_e^* and two hole pockets with different effective masses $m_{lh}^* \ll m_{hh}^*$. The electron pocket and the light-hole (lh) pocket cross the Fermi energy E_F, whereas the heavy-hole (hh) pocket sits slightly below E_F. [134, 24, 124]

Let us first discuss the elastoresistivity in zero magnetic field. Within a semiclassical approach, the conductivity is given by $\sigma = \sum_\alpha \sigma_\alpha$ with $\sigma_\alpha = n_\alpha e^2/(\Gamma_\alpha m_\alpha^*)$ being the contributions from individual bands. Here, n_α is the carrier density and Γ_α is the scattering rate of band α. The zero-field elastoresistivity thus reads

$$\frac{1}{\rho(0)}\frac{d\rho(0)}{d\epsilon} = \sum_\alpha \frac{\sigma_\alpha(0)}{\sigma(0)}\left[\frac{\zeta_m^{(\alpha)}}{m_\alpha^*} + \frac{\zeta_\Gamma^{(\alpha)}}{\Gamma_\alpha} - \frac{\zeta_n^{(\alpha)}}{n_\alpha}\right], \tag{6.1}$$

where $\rho(0) \equiv \rho(\mathbf{B} = 0)$ and we have introduced the strain derivatives $\zeta_m^{(\alpha)} = \frac{dm_\alpha^*}{d\epsilon}$, $\zeta_\Gamma^{(\alpha)} = \frac{d\Gamma_\alpha}{d\epsilon}$ and $\zeta_n^{(\alpha)} = \frac{dn_\alpha}{d\epsilon}$. Increasing m_α^* and Γ_α increases ρ, whereas increasing the carrier density n_α reduces ρ. Contributions from different bands are weighted according to their contribution to the total conductivity. One can estimate the strain response of the scattering rates $d\Gamma_\alpha/d\varepsilon$ using expressions for impurity and phonon scattering rates from Boltzmann theory and using Matthiessen's rule [135] (see also the SI).

At low temperatures, where impurity scattering dominates, the elastoresistivity then becomes $\frac{1}{\rho(0)}\frac{d\rho(0)}{d\epsilon} = 2\sum_\alpha \frac{\sigma_\alpha}{\sigma}\left(\frac{\zeta_m^{(\alpha)}}{m_\alpha^*} - \frac{1}{3}\frac{\zeta_n^{(\alpha)}}{n_\alpha}\right)$. From analyzing quantum oscillations (see Fig. 6.7), we conclude that both strain derivatives have the same sign $\zeta_m^{(\alpha)}, \zeta_n^{(\alpha)} < 0$ such that the two effects compete with each other. Which of the two dominates depends on microscopic details. A DFT transport calculation, which keeps the scattering rates constant, predicts a positive elastoresistivity, in agreement with experimental results (see SI for details). As shown in Fig. 6.8, this behavior is also readily captured within our effective three-band model, where we use as input from DFT that the two holes bands move up in energy under compressive strain, while the electron band moves down (see Fig. 6.7 (a)). Interestingly, the heavy-hole band shifts up by an amount about ten times larger than the other two bands, yet still remains below E_F. At low temperatures, it thus remains completely filled and does not contribute to transport. Electrons redistribute solely among the electron and light-hole pockets such that both n_e and n_{lh} increase, causing an increase in the total carrier density n and positive elastoresistivity (see Fig. 6.8 (d)). In the experiment, this effect seems to dominate over the strain-induced enhancement of the effective masses, which tends to reduce the elastoresistivity.

The situation is different at finite temperature, where one needs to take into account additional bands that lie within a range of k_BT of the Fermi energy. The non-monotonic behavior and associated sign change of the elastoresistance as a function of T can thus be understood as a result of a redistribution of carriers including those nearby bands, i.e. including the hh band. A precise modeling of the strain-induced modifications of the bandstructure at finite T require further experimental studies, e.g. ARPES under finite strain, or first-principle calculations that take thermal expansion effects into account. We can, however, capture the experimentally observed behavior of Fig. 6.5 within our low-energy model. As shown in Fig. 6.8, the decrease of the elastoresistivity (as T increases) follows from the fact that the heavy-hole pocket is shifted upwards by strain to within a range of k_BT of the Fermi energy. It is thus only partially occupied at finite T, and holes redistribute from the light-hole to the heavy-hole pocket. This leads to the observed increase of the resistivity at finite temperatures, and the eventual sign change. Note that there

is an additional negative contribution to elastoresistivity from the enhancement of the effective masses. The broad minimum of the elastoresistivity arises within our model from a competition of electrons moving from the heavy-hole pocket to both the light-hole band (decreasing n_{lh} and ρ) and the electron band (increasing n_e and ρ). Specifically, the slope of the elastoresistivity is determined by the ratio of the density of states g_{lh}/g_e at the chemical potential $\mu(T)$. The slope is negative for $g_{lh} > g_e$, as electrons from the heavy-hole pocket are then more likely to enter the light-hole one. The precise value of this ratio depends on microscopic details.

At finite magnetic field, the MER shows distinct behavior in the low-temperature quantum regime $T \leq 15$ K and the semiclassical regime at higher T. In the quantum regime, the sensitivity of the MER to strain and fields described above, readily follows from strain tuning of the Shubnikov-de Haas (SdH) oscillation frequencies. In the semiclassical regime $T > 15$ K, the observed MER can be captured by an effective two-band model of electron and hole carriers with density n_e, n_h and mobilities $\mu_e = e/(m_e^*\Gamma_e)$ and μ_h. We capture the contribution of the two hole pockets via an effective hole mobility $\mu_h = e/(\bar{m}_h^*\bar{\Gamma}_h)$, where $\bar{m}_h^*, \bar{\Gamma}_h$ are averages of the two hole pockets. As shown in detail in the SI, we start from the well-known semiclassical form of the resistivity $\rho(B) = \rho(0)\left(\frac{1+e\rho(0)(n_e\mu_h+n_h\mu_e)\mu_e\mu_h B^2}{1+[e\rho(0)\mu_e\mu_h(n_e-n_h)B]^2}\right)$ and consider "intermediate" magnetic field strengths, where the magnetoresistance is not yet saturated, to arrive at

$$\frac{1}{\rho(B)}\frac{d\rho(B)}{d\epsilon} - \frac{1}{\rho(0)}\frac{d\rho(0)}{d\epsilon} = 2\mu^2 B^2 \frac{\rho(0)}{\rho(B)} \sum_\alpha \frac{\sigma_\alpha}{\sigma(0)} \left(-\frac{\zeta_m^{(\bar{\alpha})}}{m_{\bar{\alpha}}^*} - \frac{\zeta_\Gamma^{(\bar{\alpha})}}{\Gamma_{\bar{\alpha}}} \right) . \tag{6.2}$$

Here, $\bar{\alpha} = e(h)$ for $\alpha = h(e)$, and we have approximated $\mu_e \approx \mu_h \equiv \mu$ (see the SI for the general case). Importantly, we find a deviation of the finite field elastoresistivity from the zero-field one that increases as B^2 for small fields $B \ll B_1 = e\rho(0)[(n_e\mu_h + n_h\mu_e)\mu_e\mu_h]^{-1/2}$. It reaches saturation when $B \gg B_1$ due to the term $\rho(B)$ in the denominator (see Fig. 6.6 (c) and SI). Note that B_1 can also be extracted from the coefficient of the non-saturating, quadratic MR $= (B/B_1)^2$, which yields that B_1 increases from $B_1(30\text{ K}) = 1.4$ T to $B_1(90\text{ K}) = 12$ T, [9] in agreement with our findings. According the Eq. (6.2) the prefactor of the quadratic MER term depends on the strain response of the effective masses and the scattering rate, but interestingly does not depend on the change of the carrier density. It probes a different strain derivative and thus provides novel insights

beyond a zero-field elastoresistivity measurement. In particular, unlike, the elastoresistivity in zero field, it exhibits the same sign for all temperatures. This allows us to conclude that the sign change of the $B = 0$ elastoresistivity is rooted in the non-monotonic behavior of the strain derivative of the carrier densities $\zeta_n^{(\alpha)}(T)$ (see Fig. 6.8). Finally, from our effective model we find that $\zeta_m^{(\alpha)} < 0$ and $\zeta_\Gamma^{(\alpha)} < 0$, and therefore predict a quadratically increasing MER (at all T and low $B \ll B_1$), in agreement with experiment (see Fig. 6.6 and SI Fig. 6.17).

To conclude, we report a large and non-monotonic MER in high-mobility crystals of WTe_2. This provides new insights into the strong coupling of elastic and electronic degrees of freedom in this material, opening a route to engineer magneto-transport properties via strain. Using a combination of density-functional theory and analytical low-energy multi-band model calculations, we relate these observations to strain-induced changes of the bandstructure, resulting in an increase as well as a redistribution of carriers between bands with different mobilities. Promising future research directions are to investigate the impact of thermal expansion and electronic correlations on both the bandstructure and its response to strain, as well as the role of the edge states in magnetotransport under finite strain.

6.2.1 Method

Single crystals of WTe_2 were grown by solution method, following the procedure described in Ref. [24]. Temperature and field dependent transport properties were measured in a Quantum Design(QD), Physical Property Measurement System for $1.8 \leq T \leq 300\,\mathrm{K}$ and $|H| \leq 140\,\mathrm{kOe}$. Resistance measurements under uniaxial strain were carried out using a Razorbill CS100 cryogenic uniaxial strain cell. To be more specific, outer and inner piezoelectric stacks were controlled by two Keithley Model 2400 source meters, and corresponding length changes of the crystals were measured by a capacitance sensor using an Andeen-Hagerling(AH) Model 2550A capacitance bridge. Note that there is always certain errors in the length change measurements due to thermal contraction of various parts. Although some thermal effects were addressed (i.e. the thermal effect from piezoelectric materials was canceled via symmetric usage of outer and inner piezoelectric stacks

and the thermal effect from the capacitance sensor was removed by subtracting the temperature dependence capacitance of the empty cell result), others, including the thermal contraction from the cell and the crystal itself, were not considered. The crystals were mounted across the two plates with Stycast 2850 FT, so that the crystal was mechanically attached to the plates firmly and electrically isolated from the cell body.(Fig. 6.5 (a)) We estimated that, due to the epoxy, about 80 % of the displacement was transmitted as sample strain. In this calculation, we used the Young's modulus of the crystals of 80 GPa and the thickness of the glue was $\sim 50\,\mu m$. [136, 137] The contacts for the electrical transport measurement were prepared in a standard linear four-probe configuration using Epotek-H20E silver epoxy and silver paint, and Lakeshore Model 370 AC resistance bridge conducted the resistance measurement of the crystals. Due to the large drop in the resistivity of WTe_2 upon cooling in zero field combined with the limit of the resistance bridge (resolution is $1\,\mu\Omega$ with $I = 3.16\,\mathrm{mA}$ in the range of $2.0\,\mathrm{m}\Omega$), we were not able to conduct the elastoresistance measurements below $T < 50\,\mathrm{K}$ with $H = 0\,\mathrm{T}$ in the above experimental setting. In order to overcome this limit of the measurement, we performed the elastoresistance experiment without the magnetic field using Stanford Research Systems(SRS) 860, Lock-In Amplifier and SRS Model CS580, voltage controlled current source in a Janis SHI-950-T closed cycle cryostat. Two samples were measured in this way, S3' and S4. S3' is esentially same as S3, which was measured in PPMS, but new contacts were made after cleaving the top layer. S4 was mounted in Razorbill CS130 cryogenic uniaxial strain cell. S4 was secured with a small amount of Devcon 5 minute epoxy in between anodized plates, which can give the largest transmitted strain on the sample.

Strain is defined as $\epsilon\,[\%] = (L - L_0)/L_0 \times 100$, where L_0 is the unstrained length. Thus, a positive sign represents tensile strain and a negative sign stands for compressive strain. We noticed that the crystals are very easy to break when even a small amount of tensile strain is applied. The compressive strain at which the sample starts to buckle can be calculated based on the ratio between length and thickness (L/t) of the crystals: $L/t = \pi/\sqrt{3\epsilon}$. [138] From the calculation, we expected buckling of all three samples that we measured above $\epsilon = -1.5\,\%$. However, the first sample of WTe_2, S1, cleaved at $\epsilon \sim -0.3\,\%$, which was before the sample started to buckle due to

the easily exfoliatable nature of the crystal. In addition, the second crystal, S2, showed a jump at $\epsilon \sim -0.16\,\%$ without visual observation of a cleave or crack in the sample. This might indicate that cracks or small cleaving can happen even with small strain due to a layered structure. Based on all of the above, elastoresistance measurements were done only $\epsilon \leq \pm 0.013\,\%$ which corresponds to a maximum voltage applied to the piezoelectric material of $V = \pm 5\,\mathrm{V}$ for the third single crystals of WTe_2, S3. Within this range, resistance response to the strain ($\Delta R/R$ Vs. strain) was linear without hysteresis (more details are in SI). Details about Shubnikov de Haas oscillations can be found in SI.

Band structures of WTe_2 at strains from -0.2 to 0% were calculated in density functional theory [108, 109] (DFT) using local density approximation [139, 140] (LDA) with spin-orbit coupling (SOC) effect included. The dimensions of the unit cells were determined from experimental lattice constants [141] ($a = 3.477\,\mathring{A}$, b =6.249 $\mathring{A}$ and $c = 14.018\,\mathring{A}$) plus strain and a Poisson ratio [132] of 0.16. The ionic positions in the unit cells were relaxed at different strains and then band structures are calculated. The carrier densities were calculated from the volume of electron and hole pockets in reciprocal space. The quantum oscillation frequencies were calculated by finding the extreme orbit [133] of hole and electron pockets with the magnetic field along the c direction. The conductivity without magnetic field were calculated from the semi-classical Boltzmann equation with the interpolated DFT band structures. [142] DFT calculations were done in VASP [112] with a plane-wave basis set and projector augmented wave [111] method. We used the orthorhombic cell of 12 atoms with a Γ-centered Monkhorst-Pack [114] ($12 \times 6 \times 3$) k-point mesh. The kinetic energy cutoff was 223 eV. The convergence with respect to k-point mesh was carefully checked, with total energy converged, e.g., well below 1 meV/atom. For ionic relaxation, the absolute magnitude of force on each atom was reduced below $0.01\,\mathrm{eV}/\mathring{A}$.

6.2.2 Supplementray information

6.2.2.1 Elastoresistance experiment

We took care to measure our data in the linear response limit. To do this we measured $\Delta R/R$ versus strain loops for a variety of strain (or voltage) sweeps at base temperature (Fig. 6.9) as well as over the whole temperature range (Fig 6.10). We find that as we increase the size of strain sweeps there is an increasing hysterisis. As a result of these measurements and out of an abundance of caution, we limit our measurements to $|\epsilon| \leq 0.013\,\%$ so as to be in the linear regime.

6.2.2.2 Large changes in elastoresistance due to quantum oscillations

Figure 6.11 shows magnetoresistance without and with ($\epsilon = -0.136\,\%$) strain at $T = 2\,\mathrm{K}$. Whereas the MR increases quadratically without saturation up to 14 T, quantum oscillations are detected above $\sim 4\,\mathrm{T}$ in both cases. Due to the strain induced changes in frequencies, there are mismatches in quantum oscillation peaks in the high magnetic field regime. Therefore, elastoresistances change dramatically from negative to positive with small changes of the magnetic field. To illustrate this more clearly, enlarged magnetoresistances from 10 T to 14 T are shown in the inset of Fig. 6.11. The green dashed line indicates negative elastoresistance whereas the blue dashed line indicates positive elastoresistance.

Subtracting the MR without strain from MR with strain allows us to directly examine oscillations in the MER as shown in Fig. 6.12 (a) and (c). In order to confirm these as quantum oscillations, we did FFT on the data with $1/B$. Figure 6.12 (b) and (d) are the results of FFT on S2 and S3. All four frequencies, that were detected from SdH, are observed in both samples. As such, these data, as well as the data highlighted in the inset of Fig. 6.6 (a) and (b), are clear manifestations of quantum oscillations in MER.

Based on Lifshitz and Kosevich fomula, one can write MER oscillation as below.

$$MER_{osc} = \sum_i A_i \left[sin\left\{ \frac{2\pi(F_i + \delta F_i)}{B} + \phi_i \right\} - sin\left\{ \frac{2\pi F_i}{B} + \phi_i \right\} \right] / \varepsilon. \tag{6.3}$$

For $\delta F \ll F$ and $\frac{2\pi\delta F_i}{B} \ll 1$,

$$MER_{osc} = \sum_i A_i cos\left\{\frac{2\pi F_i}{B} + \phi_i\right\} \cdot \frac{2\pi\delta F_i}{B} \cdot \frac{1}{\varepsilon} \tag{6.4}$$

Note that the frequency of oscillations are same as SdH.

6.2.2.3 Quantum oscillation analysis

When using a FFT to determine the frequencies of the quantum oscillations, the resolution of frequencies is determined by the size of the Fourier window. Figure 6.13 highlights the data spacing around the local maximum which defines F^1; the data points are more closely spaced for wider field range windows. In order to resolve the strain dependence of frequency changes in WTe_2, within a relatively small strain range, the magnetic field range of $0.5\,\mathrm{T} < H < 13.95\,\mathrm{T}$ was used for all strains.

In order to check the reproducibility, we performed similar experiments and analysis on S3 with a fewer number of strains. As shown in Fig. 6.14 (a) and (b), S3 also shows similar behavior as S2 (Fig. 6.7).

Although the resolution is important to resolve the peaks, one also needs to consider the amplitude of peaks to get an effective mass. In this case, it is important to choose the magnetic field range from where the MR starts to show quantum oscillations at the highest temperature. To be more specific, the amplitude of peaks can be reduced due to an artifact of the FFT analysis which comes from the low magnetic field MR data without quantum oscillation. In addition, quantum oscillations at higher temperatures require higher magnetic fields to start. Thus, one needs to determine the magnetic field range based on the highest temperature data that will be used for the analysis. With all these points in mind, we used the magnetic field range of $5\,\mathrm{T} < H < 13.95\,\mathrm{T}$ to infer the amplitude changes as a function of the temperature with different strains.

6.2.2.4 Electrical conductivity from density functional theroy (DFT) calculation

The conductivity is calculated from the semi-classical Boltzmann equation with the interpolated DFT band structures. [142] Conductivity over relaxation time (σ/τ) without and with (ϵ = -0.2 %)

are plotted as a function of chemical potential in Fig. 6.15. The result shows positive elastoresistance(It is positive since for negative strain the conductivity goes up) within the chemical potential range of -0.04 $< \mu <$ 0.04 eV. This may be an additional indication that the pure electronic term gives positive elastoresistance in WTe_2.

Table 6.1 Curvature and Edge for each bands in the pocket regions (Fig. 6.16) that are of interest for the modeling of conductivity

Curvature (eV A^2)	1	2	3'	3/4	5/6
0.0	-18.4	-19.2	26.6	35.8	15.1
-0.2	-16.9	-18.2	28.1	37.1	15.4
Edge (eV)	1	2	3'	3/4	5/6
0.0	0.028	0.033	0.024	-0.068	0.012
-0.2	0.032	0.039	0.026	-0.071	0.010

6.2.2.5 Modeling and analysis

To interpret the (magneto-)elastoresistance (MER) measurements we employ an effective low-energy three-band model. This simplified model can account for the salient features of the (magneto-)elastoresistance (or resistivity rather), in particular its non-monotonic behavior in zero magnetic field and its increase and rapid saturation in finite field. As input it uses the strain-induced changes in the electronic bandstructure, that we infer from experiment and DFT calculations. The minimal model consists of one hole and one electron pocket that cross the Fermi energy E_F at $T = 0$ as well as another hole pocket slightly below E_F (see Fig. 6.8 (a)). This captures the essence of the more complicated bandstructure of WTe_2 observed within ARPES [24, 124, 134] and first-principle calculations [143] (see Fig. 6.7 (a)) with two pairs of (almost degenerate) electron and two pairs of (almost degenerate) hole pockets, and an additional hole pocket around the Γ point with a flat dispersion. (There are additional electron pockets slightly above the Fermi energy, see Fig. 6.16. Taking them into account does not change our main qualitative conclusions). The three bands can be characterized by effective masses m^*_α with $\alpha = e, lh, hh$ corresponding to electron (e), light-hole (lh) and heavy-hole (hh) pockets. We can approximate the effective masses using DFT calculations, neglecting small anisotropies in momentum space. We note that at $T = 0$, our simplified model

calculation described below agrees with a more detailed DFT transport calculation (see Fig. 6.15) that takes the anisotropies in momentum space properly into account.

Let us first discuss the case of zero magnetic field $\mathbf{B} = 0$. Using a semiclassical Drude-Boltzmann approach and within the quadratic band approximation, one arrives at the well-known Drude formula for the conductivity $\sigma_\alpha = n_\alpha e^2/(\Gamma_\alpha m^*_\alpha)$, where n_α is the carrier density and Γ_α is the scattering rate of band α. The contributions from different bands add in parallel $\sigma = \sum_\alpha \sigma_\alpha$ and the total resistivity is given by $\rho = \sigma^{-1}$. The elastoresistivity is now governed by a sum of different contributions

$$\frac{1}{\rho(0)}\frac{d\rho(0)}{d\epsilon} = \sum_\alpha \frac{\sigma_\alpha(0)}{\sigma(0)}\left[\frac{\zeta_m^{(\alpha)}}{m^*_\alpha} + \frac{\zeta_\Gamma^{(\alpha)}}{\Gamma_\alpha} - \frac{\zeta_n^{(\alpha)}}{n_\alpha}\right], \tag{6.5}$$

where $\rho(0) \equiv \rho(\mathbf{B} = 0)$ and we have introduced the strain derivatives $\zeta_m^{(\alpha)} = \frac{dm^*_\alpha}{d\epsilon}$, $\zeta_\Gamma^{(\alpha)} = \frac{d\Gamma_\alpha}{d\epsilon}$ and $\zeta_n^{(\alpha)} = \frac{dn_\alpha}{d\epsilon}$. Increasing m^*_α and Γ_α increases ρ, while increasing the carrier density n_α reduces ρ. Contributions from different bands are weighted according to their contribution to the total conductivity.

To make progress and estimate $d\Gamma/d\epsilon$, we will use the scattering rates derived within Boltzmann theory and relate $d\Gamma_\alpha/d\epsilon$ to changes in the density of states and the phonon properties. The scattering rate consists of a temperature independent impurity part and a T-dependent phonon part due to scattering off (mainly acoustic) phonons. One finds [135]

$$\frac{1}{\Gamma^{(\alpha)}_{\text{imp}}}\frac{d\Gamma^{(\alpha)}_{\text{imp}}}{d\epsilon} = \frac{\zeta_m^{(\alpha)}}{m^*_\alpha} + \frac{1}{3}\frac{\zeta_n^{(\alpha)}}{n_\alpha} \tag{6.6}$$

$$\frac{1}{\Gamma^{(\alpha)}_{\text{ph}}}\frac{d\Gamma^{(\alpha)}_{\text{ph}}}{d\epsilon} = -\frac{\zeta_m^{(\alpha)}}{m^*_\alpha} - 4\frac{\zeta_c}{c_s}, \tag{6.7}$$

where $\zeta_c = \frac{dc_s}{d\epsilon}$ is the strain induced change of the phonon velocity. More generally, strain may affect $\Gamma^{(\alpha)}_{\text{ph}}$ in a more complicated way as well, for example, by modifications of the phonon polarization. Under compressive strain, one generally expects that the acoustic phonon velocity increases (hardening) such that $\zeta_c < 0$, due to a change of the Young modulus under strain. As this is a higher order effect in the strain, we expect it to be subleading compared to the change of the carrier densities $\zeta_n^{(\alpha)}$ and the effective masses $\zeta_m^{(\alpha)}$.

Here, we have assumed parabolic and isotropic bands. A more realistic estimate of the strain induced change, in particular of the electron-phonon scattering rate, requires detailed modeling beyond our current work. One can therefore consider $\frac{d\Gamma_{\rm ph}^{(\alpha)}}{d\epsilon}$ also as a phenomenological parameter of our theory. Using the Matthiessen rule, the total scattering rate is then given by $\Gamma^{(\alpha)} = \Gamma_{\rm imp}^{(\alpha)} + \Gamma_{\rm ph}^{(\alpha)}]$, which yields the elastoresistitivy in zero field as

$$\frac{1}{\rho(0)}\frac{d\rho(0)}{d\epsilon} = \sum_\alpha \frac{\sigma_\alpha(0)}{\sigma(0)}\left[\frac{\zeta_m^{(\alpha)}}{m_\alpha^*}\left(1+\frac{\Gamma_{\rm imp}^{(\alpha)}-\Gamma_{\rm ph}^{(\alpha)}}{\Gamma_\alpha}\right)+\frac{\zeta_n^{(\alpha)}}{n_\alpha}\left(\frac{1}{3}\frac{\Gamma_{\rm imp}^{\alpha}}{\Gamma_\alpha}-1\right)-4\frac{\zeta_c}{c_s}\frac{\Gamma_{\rm ph}^{(\alpha)}}{\Gamma_\alpha}\right]. \tag{6.8}$$

At low temperatures $\Gamma_{\rm ph}^{(\alpha)} \ll \Gamma_{\rm imp}^{(\alpha)}$, the elastoresistivity is determined solely by electronic terms and bands that cross the Fermi energy. The behavior of the hole pocket below E_F is thus not relevant to the strain response at low temperature. At low T, Eq. (6.8) simplifies to

$$\frac{1}{\rho(0)}\frac{d\rho(0)}{d\epsilon} = 2\sum_\alpha \frac{\sigma_\alpha}{\sigma}\left(\frac{\zeta_m^{(\alpha)}}{m_\alpha^*}-\frac{1}{3}\frac{\zeta_n^{(\alpha)}}{n_\alpha}\right) \tag{6.9}$$

From analyzing quantum oscillations, we find that both strain derivatives have the same sign $\zeta_m^{(\alpha)}, \zeta_n^{(\alpha)} < 0$ such that the two effects compete with each other. Which of the two dominates depends on microscopic details. In Fig. 6.5 (c), we find that the sign of the elastoresistance in the low temperature regime is different for different samples, while the magnitude rapidly decreases at low T (see Fig. 6.5). We can understand the increase of the carrier density ($\zeta_n^{(\alpha)} < 0$) within our effective three-band model description by noticing that the heavy-hole band is pulled up in energy by strain while the electron band is lowered. As a result, some electrons are being redistributed from the hole to the electron band, incresing the total number of carriers $n = n_e + n_h$ (keeping $\Delta n = n_e - n_h$ fixed). We thus find a positive contribution to the elastoresistivity from ζ_n within our model (see Fig. 6.8 (c) at low temperatures).

From the data in Fig. 6.7 (e) and (f), we find that $\zeta_n^{(\alpha)}$ and $\zeta_m^{(\alpha)}$ are of the same order of magnitude. It is therefore difficult to estimate which dominates and unambigously predict the sign. In fact, we estimate that the strain-induced enhancement of the mass slightly dominates, which yields $\frac{1}{\rho(0)}\frac{d\rho(0)}{d\epsilon} < 0$. One should keep in mind, however, that quantum oscillations measure the cyclotron mass, which is a property of an extremal orbit, and not the effective mass $m_i^{-1} = \frac{\partial^2 E_{\boldsymbol{k}}}{\partial k_i \partial k_i}$ (or rather the velocity $v_i = \frac{\partial E_{\boldsymbol{k}}}{\partial k_i}$) in the current direction i (averaged over the Fermi surface), which

is the quantity relevant for transport. [135] In fact, a more detailed microscopic DFT transport calculation predicts a positive slope for ρ/τ, in agreement with experiment (this DFT analysis neglects changes in the scattering time though).

At higher temperatures, one must take into account not only the strain-induced modifications of the bandstructure right at the chemical potential μ, but also further away from it within a range of $k_B T$. Strain also affects the carriers in thermally (de)populated bands. This is the dominant effect in semiconductors, where strain leads to a redistribution of carriers among valleys with different effective masses, leading to a characteristic $1/T$ behavior of the elastoresistance. [144] We indeed find such a $1/T$ dependence of the elastoresistance at high temperatures $T > 250$ K. However, in WTe_2 the behavior is much richer due to the presence of both electron and hole carriers.

The observed increase of the resistivity under compressive strain at intermediate and high T in Fig. 6.5 (c), corresponds to $\zeta_n^{(\alpha)} > 0$, i.e., a decrease in the carrier density under compressive strain. As shown in Fig. 6.8 (c) our three-band model calculation reproduces such a behavior (at intermediate temperatures) using the rigid band energy shift trends under strain obtained from DFT as input (see Fig. 6.7 (a)). The non-monotonic behavior of the elastoresistivity as a function of temperature arises within our model from the fact that the heavy-hole pocket contribetes to transport only at finite T, where it is partially filled. Within DFT, strain lifts this pocket in energy by an amount ΔD_{hh} that about a factor of 10 times larger than found for the other two pockets. As a result, the dominant effect is a redistribution of holes from the light to the heavy hole pockets, resulting in an increase of ρ at intermediate and larger temperatures. We note that the effective mass enhancement observed within quantum oscillations now adds with the same sign to this term, making the elastoresistance more negative.

Let us now turn to the analysis of the magneto-elastoresistance (MER), i.e., the elastoresistance in finite magnetic field:

$$\mathrm{MER}(T,B) \equiv \frac{1}{R(T,B,\epsilon=0)} \frac{dR(T,B,\epsilon)}{d\epsilon}\bigg|_{\epsilon=0} \tag{6.10}$$

Experimentally, as shown in Fig. 6.6, we observe a rich behavior that can be described as follows: at high temperatures, where the magnetoresistance (MR) vanishes, the magneto-elastoresistance

(MER) follows the zero-field elastoresistance (ER). At lower T, when the (non-saturating) MR first becomes finite and then exceptionally large, we find an increase of the MER proportional to B^2 (at small B fields). At temperatures $T \leq 50$ K, the observed increase of MER as a function of B crosses over into saturation at a positive plateau value. The MER saturation field strength $B_1(T)$ decreases with temperature T. As we show below, the saturation field scale B_1 can be associated with the coefficient of the quadratic B-field dependence of the non-saturating MR. At the lowest temperatures $T < 10$ K, where MR exhibits SdH oscillations, the MER exhibits a delicate and strong dependence on the magnetic field, ranging from $\mathrm{MER}(T_0, B) = +120$ to $\mathrm{MER}(T_0, B') = -80$ in the field range of less than one Tesla: $|B - B'| \approx 0.5$ T (see Fig. 6.6).

The interesting behavior of MER quantum oscillations in the quantum regime can be straightforwardly understood from the strain-induced change of the SdH oscillation frequency that we have experimentally observed. It occurs due to strain tuning the size of the extremal orbits (see above for more details). We find that the orbits increase under compressive strain, which is in agreement with the prediction of the three-band model that the carrier densities increase at low temperatures. At fixed temperature and field, strain can move the minima and maxima of the oscillating resistance such that a from a position close to the maximum of a SdH oscillation in zero strain becomes a position close to a minimum. This results in a large change of the resistance (see Fig 6.11). The reverse situation can occur at B-field values close by, thus explaining the sign change of $\Delta R_{\epsilon,B}$ when tuning B over a small range.

We will now show that the observations in the intermediate temperature regime 10 K $< T <$ 200 K can be qualitatively captured within a semiclassical two-band model description [11] of electron and hole carriers, where the resistivity takes the well-known form

$$\rho(B) = \rho(0)\left(\frac{1 + e\rho(0)(n_e\mu_h + n_h\mu_e)\mu_e\mu_h B^2}{1 + [e\rho(0)\mu_e\mu_h(n_e - n_h)B]^2}\right). \tag{6.11}$$

The mobilities are given by $\mu_\alpha = e/(m^*_\alpha \Gamma_\alpha)$. It was shown that the carrier compensation in WTe_2 is almost perfect and $\Delta n = n_e - n_h$ is very small. [90] As a result, MR exhibits purely quadratic dependence on magnetic field with no signs of saturation. The magnetic field range we consider

$B < 14$ T thus lies in the "intermediate" regime with $B_1(T) < B < B_{\mathrm{sat}}(T)$ with

$$B_1(T) = e\rho(0)[(n_e\mu_h + n_h\mu_e)\mu_e\mu_h]^{-1/2} \tag{6.12}$$

$$B_{\mathrm{sat}} = (e\rho(0)\mu_e\mu_h|n_e - n_h|)^{-1}\,. \tag{6.13}$$

In this regime of intermediate field strength, MER takes the form

$$\frac{1}{\rho(B)}\frac{d\rho(B)}{d\epsilon} - \frac{1}{\rho(0)}\frac{d\rho(0)}{d\epsilon} = \frac{\rho(0)}{\rho(B)}\frac{B^2}{e^2}\Bigg[\frac{1}{\rho(0)}\frac{d\rho(0)}{d\epsilon}\sum_\alpha\Big(\frac{\sigma_\alpha}{\sigma(0)}\frac{\sigma_{\bar\alpha}^2}{n_{\bar\alpha}^2}\Big) + \sum_\alpha \frac{\sigma_\alpha}{\sigma(0)}\frac{\sigma_{\bar\alpha}^2}{n_{\bar\alpha}^2}\Big(\frac{\zeta_\alpha^{(\alpha)}}{n_\alpha} - \frac{\zeta_m^{(\alpha)}}{m_\alpha^*} - \frac{\zeta_\Gamma^{(\alpha)}}{\Gamma_\alpha} - \frac{2\zeta_m^{(\bar\alpha)}}{m_{\bar\alpha}^*} - \frac{2\zeta_\Gamma^{(\bar\alpha)}}{\Gamma_{\bar\alpha}}\Big)\Bigg]\,, \tag{6.14}$$

where $\bar\alpha = e(h)$ for $\alpha = h(e)$. We thus predict a deviation of the finite field ER that increases as B^2 for small fields and reaches saturation when $B \gg B_1$ (due to the term $\rho(B)$ in the denominator). We can unambigously determine the sign of the term in the bracket, if we approximate $\mu_e \approx \mu_h \equiv \mu$, which seems to be a approximately valid in WTe_2. [102] Under this assumption, the expression simplifies to

$$\frac{1}{\rho(B)}\frac{d\rho(B)}{d\epsilon} - \frac{1}{\rho(0)}\frac{d\rho(0)}{d\epsilon} = 2\mu^2B^2\frac{\rho(0)}{\rho(B)}\sum_\alpha\frac{\sigma_\alpha}{\sigma(0)}\left(-\frac{\zeta_m^{(\bar\alpha)}}{m_{\bar\alpha}^*} - \frac{\zeta_\Gamma^{(\bar\alpha)}}{\Gamma_{\bar\alpha}}\right)\,. \tag{6.15}$$

The coefficient of the B^2 term is thus positive as $\zeta_m^{(\alpha)}/m_\alpha^* < 0$. Moreover, the saturation value is also positive, in agreement with experiment.(Fig. 6.17) Interestingly, the saturation plateau of the MER measures a different combination of strain derivatives as the zero field ER. In particular, it does not explicitly depend on the change of carrier density $\zeta^{(\alpha)}/n_\alpha$ (compare with Eq. 6.5). Combining both measurements thus allows to gain more insight into the electronic response of the material under strain. Let us discuss one particular example. We find that the saturation value of MER at large fields $B \gg B_1$ is positive for all T, while ER changes sign as a function of T. This contrasting behavior can be traced back to a non-monotonic behavior of the strain-induced change of the carrier densities $\zeta_n^{(\alpha)}$ as a function of T (as opposed to $\zeta_m^{(\alpha)}, \zeta_\Gamma^{(\alpha)}$), as this derivative $\zeta_n^{(\alpha)}$ only occurs on ER (but not in the saturation value of MER).

Finally, we note that at even larger field strengths of $B \gg B_{\mathrm{sat}}$ beyond the regime studied here, the semiclassical analysis predicts yet another combination of strain derivatives $\lim_{B\gg B_{\mathrm{sat}}}\frac{1}{\rho(B)}\frac{d\rho(B)}{d\varepsilon} =$

$\frac{1}{\Delta n^2}\sum_\alpha \frac{n_\alpha}{\sigma_\alpha}\left(\frac{\zeta^{(\alpha)}}{n_\alpha}+\frac{\zeta_m^{(\alpha)}}{m_\alpha^*}+\frac{\zeta_\Gamma^{(\alpha)}}{\Gamma_\alpha}\right)$. Interestingly, the strain derivative of the carrier density $\zeta_n^{(\alpha)}$ now occurs with the opposite sign than at zero field, predicting a sign change if this is the dominant effect (as we believe to be the case in WTe_2). Note that we have used that the compensation level Δn cannot be tuned by strain due to charge conservation, as long as the quadratic band approximation is valid.

6.2.2.6 Elastoresistance and magneto-elastoresistance of $PtSn_4$

Similar to WTe_2, $PtSn_4$ has a layered structure and an extremely large magnetoresistance (XMR) at low temperatures. [89] An important difference between two is that WTe_2 is semi-metal whereas $PtSn_4$ is metal. In particular, only a small number of bands are crossing the Fermi level in WTe_2, while lots of bands are crossing the Fermi level in $PtSn_4$. Therefore, comparing ER and MER result between two allows us to convince more about our understanding (low energy model in Sec. 6.2.2.5) of large ER and MER in WTe_2. This is because the essence of the low energy model is redistribution of carriers between bands with different curvatures like semiconducting physics.

Same experimental methods as WTe_2 were used to measure ER and MER of $PtSn_4$. Here, the magnetic field direction was parellel to the crystallographic b axis, and both current and strain were applied to crystallographic a (or c) direction. However, $PtSn_4$ was much harder to measure compared to WTe_2, because of i) 100 times smaller resistance compare to WTe_2 at 300 K, ii) huge RRR of $\sim$1000 and iii) low resistance response to strain. Therefore, we were not able to measure the ER below $T = 50$ K even with the lock-in amplifiers (SRS860) for single crystals of $PtSn_4$. In addition, larger voltage sweeps within linear regime did not improve the data quality significantly. On the other hand, we could measure low temperature ER under the magnetic field of 9 T and 14 T due to XMR of $PtSn_4$.

Figure 6.18 (a) shows the temperature dependent ER without magnetic field and with the magnetic field of 9 T and 14 T. Above $T = 50$ K, ER is constant with the value of $\sim$0.5. Considering temperature independent ER of $\sim$2 in ordinary metal systems, the high temperature ER results in $PtSn_4$ are not surprising. Deviations from the constant value below $T = 50$ K for $B = 9$ and 14 T

are rather surprising. However, it is hard to say whether the origin of this effect is due to the magnetic field or some other intrinsic properties of $PtSn_4$. This is because we were not able to obtain 0 T data below 50 K and due to rather poor signal to noise ratio of the measurements. In order to understand the deviation, further studies on high resolution ER measurments are required. In addition, ER values are not as large as WTe_2 at low temperatures even though $PtSn_4$ shows clear SdH oscillations (see Fig. 6.18 (b) inset). This implies that not all the materials with quantum oscillation has large MER at quantum regime. Therefore, large MER is indeed related to changes in Fermi surface as a function of strain.

In conclusion, we were able to check the validity of the low energy model in some sense by comparing WTe_2 and $PtSn_4$. However, the low temperature ER behavior deserves further investigation.

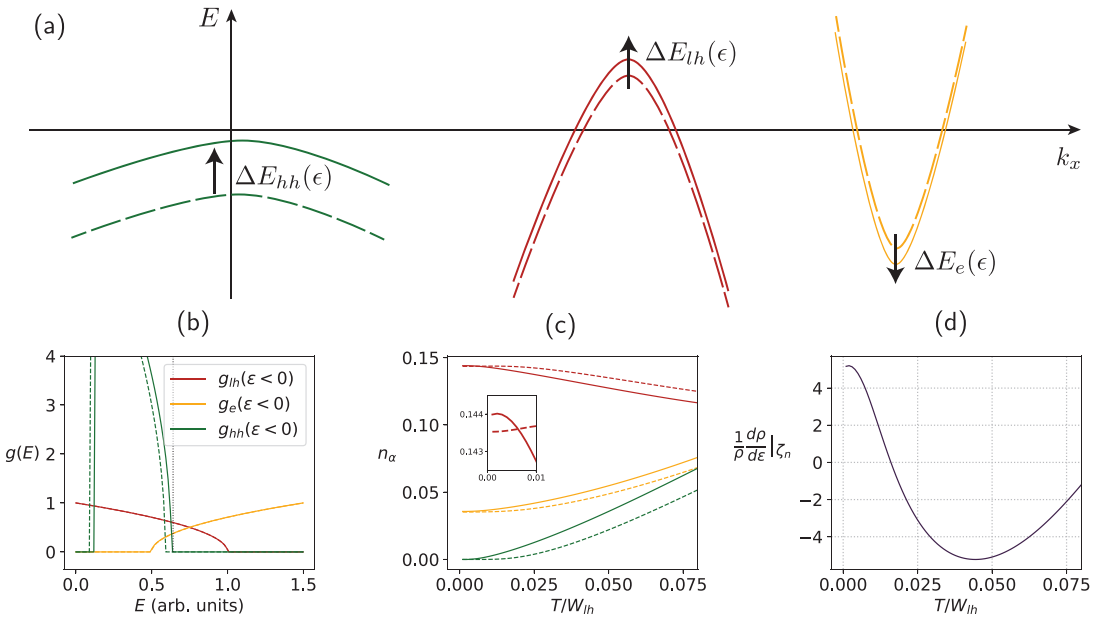

Figure 6.8 (a) Schematics of electron and hole pockets in low-energy three-band model before (dashed) and after (solid) application of compressive strain. Direction and relative size of strain-induced band shifts $\Delta E(\epsilon)$ are taken from DFT calculation (see Fig. 6.7). (b) Density of states $g(E)$ of three-band model before (dashed) and after (solid) rigid band shifts $\Delta E_e = -2 \times 10^{-3}$ and $\Delta E_{\rm hh} = 4 \times 10^{-2}$. All energies are in units of the light-hole bandwidth W_{lh}. Bandwidths are set to $W_e = W_{lh} = 1$ and $W_{hh} = 0.5$. Effective masses assumed to be strain-independent for simplicity, and their ratios set to $m_e^*/m_{lh}^* = 1$ and $m_{hh}^*/m_{lh}^* = 4.6$. The bottom of the bands are at $E_{lh}^{\rm min} = 0$, $E_e^{\rm min} = 0.5$, and $E_{hh}^{\rm min} = 0.09$. The chemical potential $\mu(T = 0) = 0.64\, W_{lh}$ is indicated by the vertical dotted line. (c) Carrier densities of the different bands n_α as a function of temperature T for zero and finite strain. Colors and linestyles are identical to panels (a) and (b). Inset shows that n_{lh} increases at low T (as long as $E_{hh}(\varepsilon) - \mu \ll T$), but decreases at higher T, causing the sign change of the ER. (d) Elastoresistivity that arises from redistribution of carriers due to rigid band shifts $\Delta E(\epsilon)$ shown in panel (b). We have assumed that these band shifts are caused by strain of size $\epsilon = 10^{-3}$. This is justified from DFT calculations, which predicts bandshifts of $2 - 30$ meV (for the different bands) for $\epsilon = 10^{-3}$. Note that the T-axis scale is of the same order, corresponding to a range from zero to roughly (two times) room temperature ($\Delta E_{hh} = 0.04 \approx 30$meV). At $T = 0$, $ER > 0$ as electrons move from the lh to the e band, increasing the total number of carriers (see inset in panel (c)). At $T > 0$, the hh band is only partially filled and moving it closer to the chemical potential shifts hole carriers from lh to hh pocket. We note that the total ER also contains a contribution from the strain-induced increase of the effective masses, which leads to an approximately T-independent negative shift of ER.

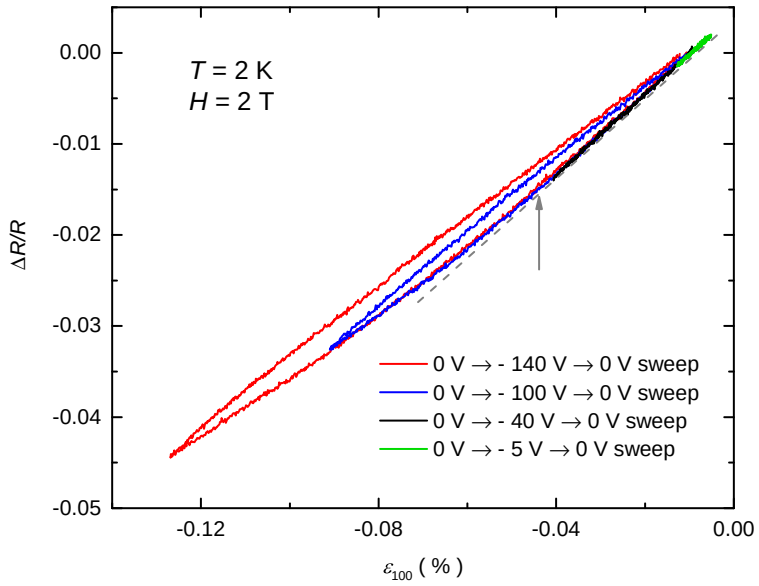

Figure 6.9 Strain(ϵ_{100}) sweep at fixed temperature of $T = 2\,\mathrm{K}$ and the magnetic field $H = 2\,\mathrm{T}$ with various voltage limits; -5 V (green line), -40 V (black line), -100 V (blue line) and -140 V (red line). The Gray dashed line is a linear guide line to point out the deviation from linear behavior, which also indicated with the gray arrow.

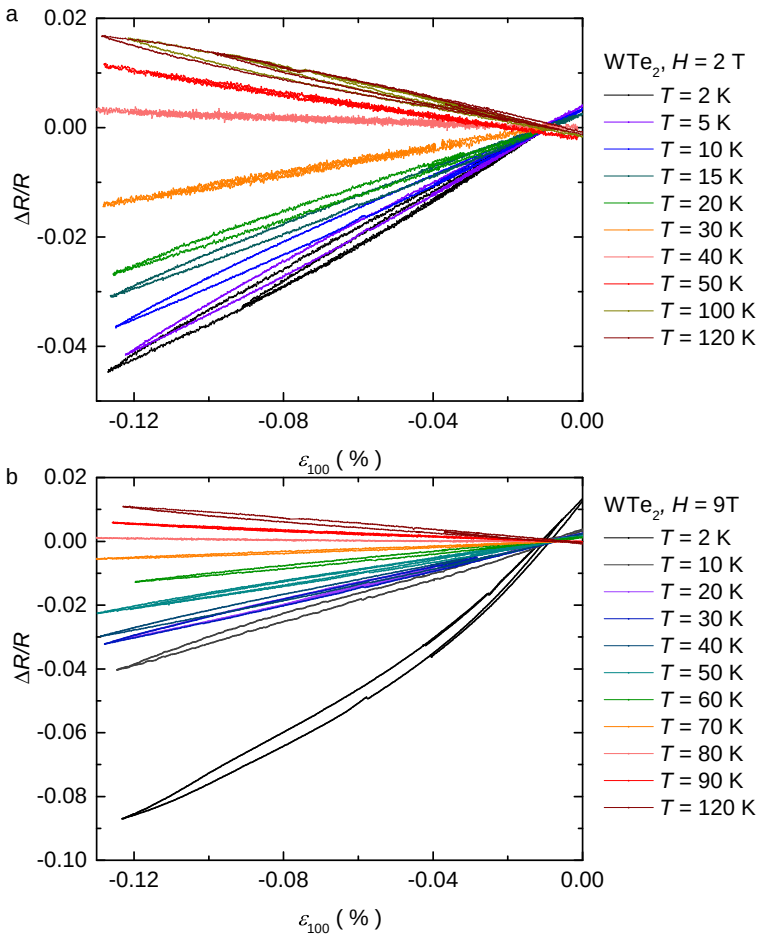

Figure 6.10 (a) Strain(ϵ_{100}) sweep at the magnetic field of 2 T. (b) Strain(ϵ_{100}) sweep at the magnetic field of 9 T. Note: clear non-linearity in 2 K data is likely associated with strain induced changes in QO frequencies and QO in MER is discussed below.

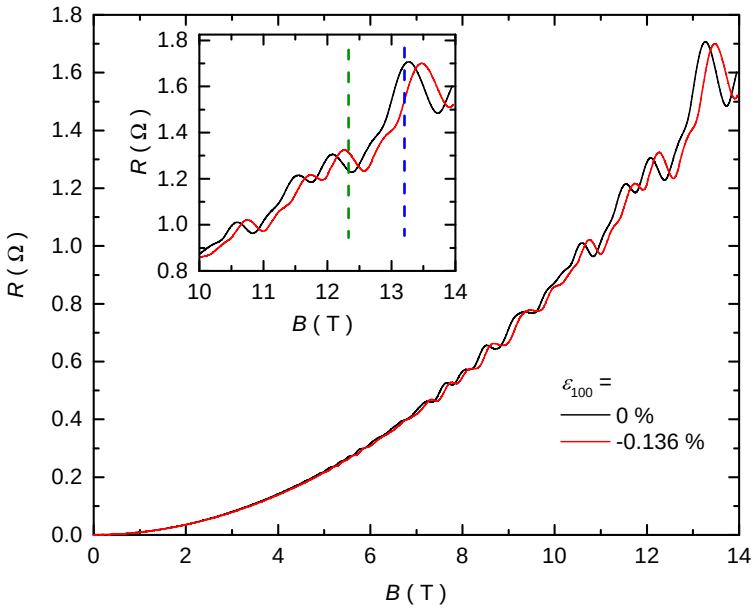

Figure 6.11 Magnetoresistance data without(black line, $\epsilon = 0\,\%$) strain and with (red line, $\epsilon = -0.136\,\%$) at $T = 2\,\mathrm{K}$. Inset shows enlarged magnetoresistances from 10 T to 14 T.

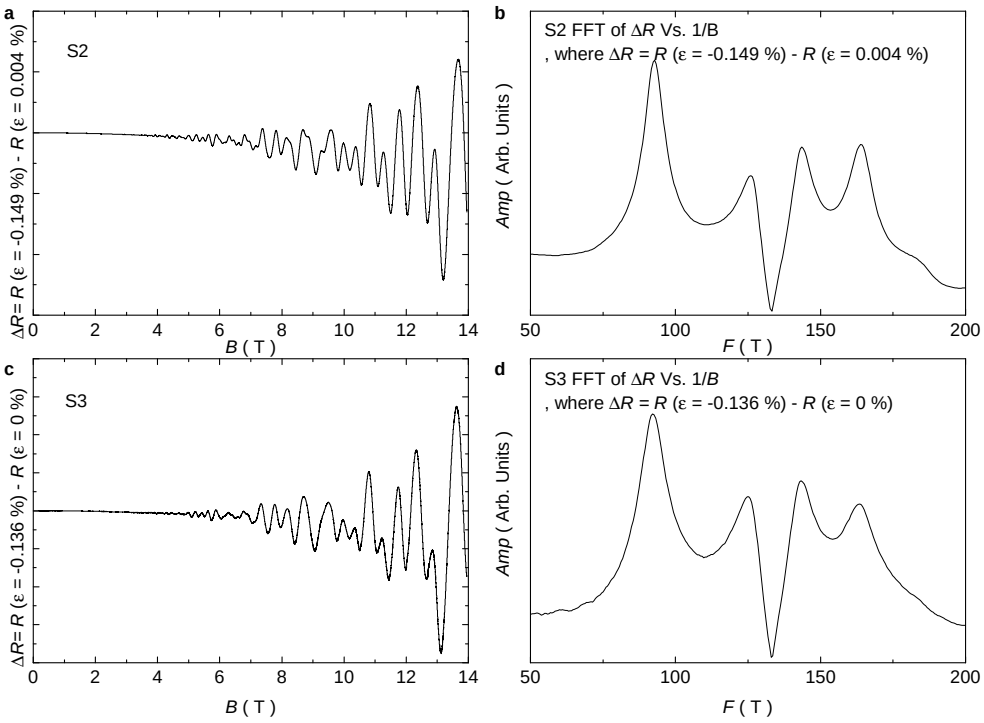

Figure 6.12 (a)$\Delta R = R(\epsilon = -0.149\,\%) - R(\epsilon = 0.004\,\%)$ as a function of the magnetic field in S2. (b) FFT of ΔR in terms of $1/B$ in S2. (c) $\Delta R = R(\epsilon = -0.136\,\%) - R(\epsilon = 0\,\%)$ as a function of the magnetic field in S3. (d) FFT of ΔR in terms of $1/B$ in S3.

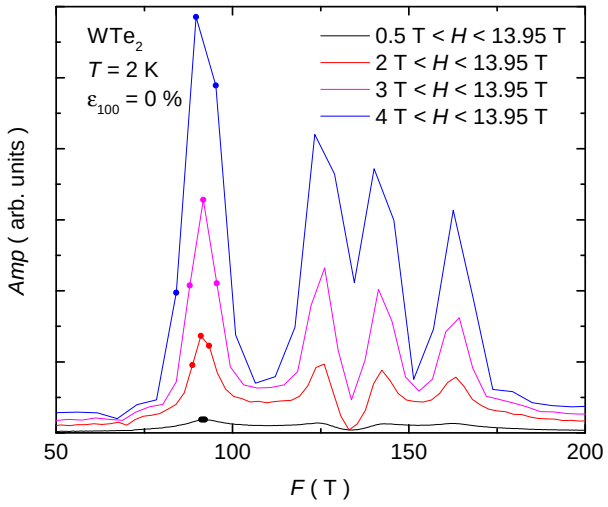

Figure 6.13 FFT results of WTe_2 at $T = 2\,\mathrm{K}$ and $\epsilon = 0\,\%$ for various magnetic field ranges. The filled circles are the data point at F^1 and the nearest data points around the F^1.

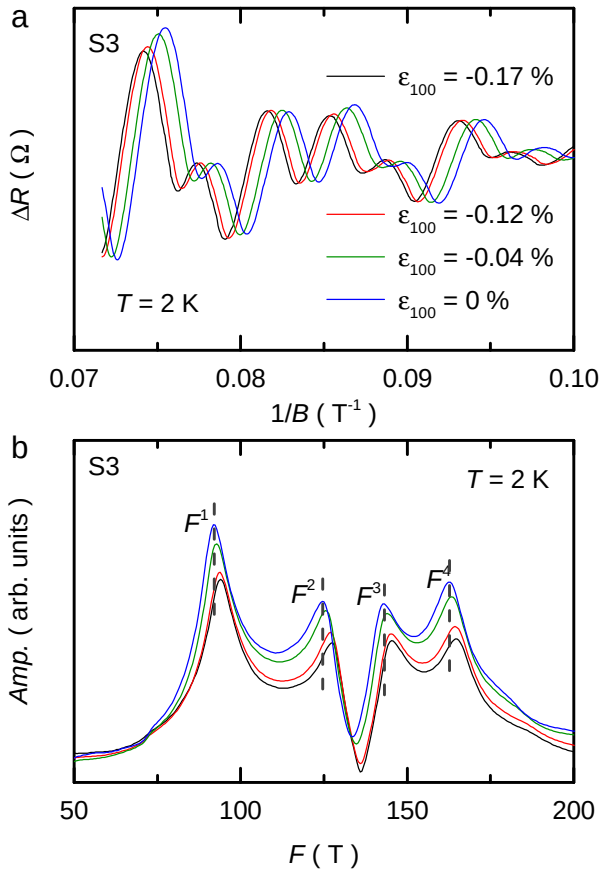

Figure 6.14 (a) SdH oscillations at various strains for S3. (b) FFT results at various strains, and gray dashed lines are guide lines for shifting of the frequencies.

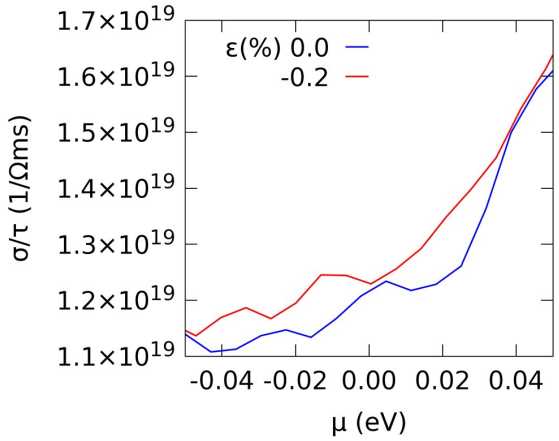

Figure 6.15 Conductivity over relaxation time (σ/τ) vs. electronic chemical potential (μ) as calculated from semi-classical Boltzmann model with DFT band structure for strain (ϵ) at 0 (blue line) and -0.2 % (red line).

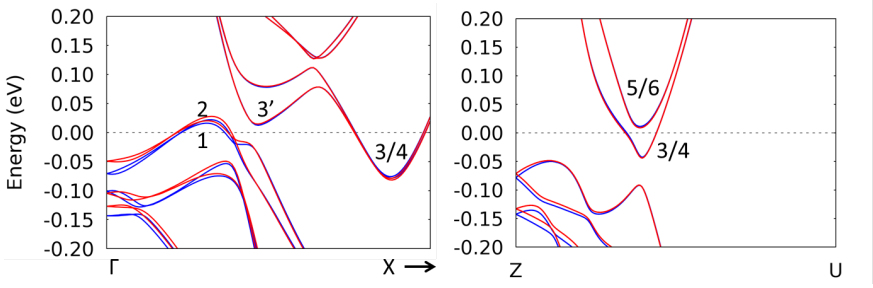

Figure 6.16 DFT band structure for strain (ϵ) at 0 (blue line) and -0.2 % (red line) along Γ-X and Z-U. Band 1 and 2 are the hole bands and band 3 and 4 are the electron bands in Fig. 6.7. Another set of electron bands (5 and 6) along Z-U are also close to Fermi level. The label i/j means the and i and j overlap with each other and have the same dispersion in the specific pocket region. The label i'means the second pocket region is also of interest because it is near the Fermi level.

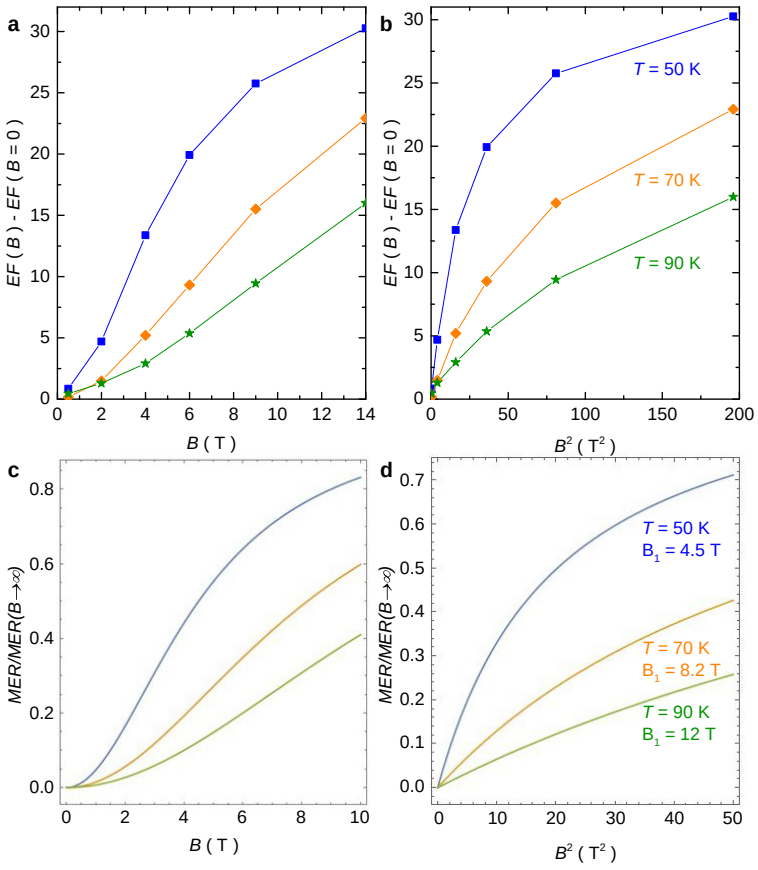

Figure 6.17 (a) The magnetic field (B) dependence data of $EF(B) - EF(0)$ at 50 K (blue), 70 K (orange) and 90 K (green). (b) The B^2 dependence data of $EF(B) - EF(0)$. (c) The magnetic field dependence simulation results of $EF(B) - EF(0)$ at 50 K (blue), 70 K (orange) and 90 K (green). B_1 value is extracted from Ref. [9]. (d) The B^2 dependence simulation results of $EF(B) - EF(0)$.

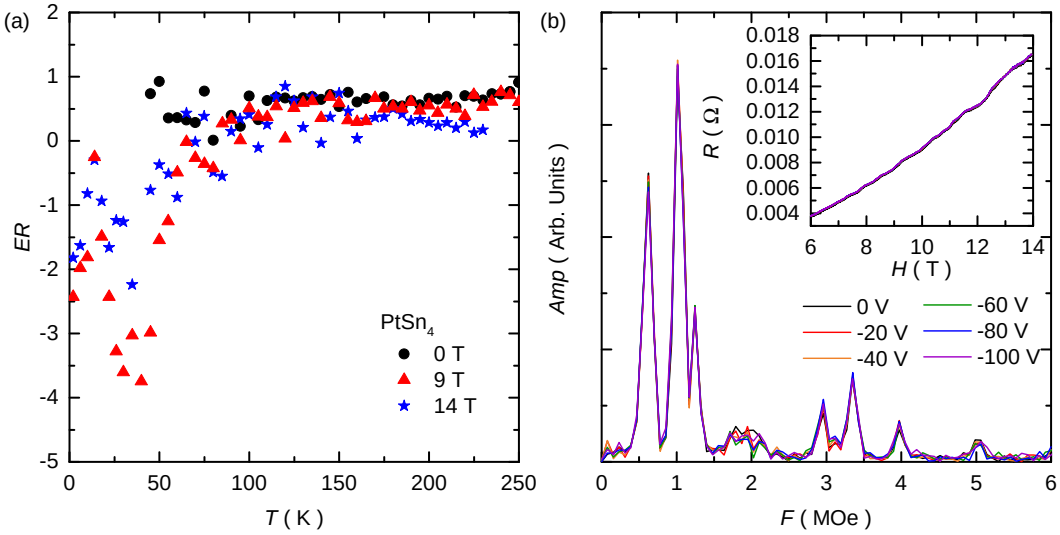

Figure 6.18 (a) Temperature dependent elastoresistance at $B = 0$, 9 and 14 T. (b) FFT results at different strains. Inset shows the magnetoresistance at various strains.

CHAPTER 7. CONCLUSIONS

Single crystals of three selected layered materials; $CrAuTe_4$, $PdSn_4$, and WTe_2 were grown via the high temperature solution growth method. The physical properties, such as magnetization, electrical resistivity and thermal transport, were studied on these single crystals at ambient conditions. In addition, the tuning effects on these layered materials were studies by applying hydrostatic pressure and uniaxial strain, and by substituting an element.

The magnetic moments in $CrAuTe_4$ order antiferromagnetically below 255 K. Clear signatures of the antiferromagnetic ordering are observed from various measurements including magnetization and electrical resistivity. In addition, ARPES observed a clear reconstruction of the Fermi surface associated with the antiferromagnetic ordering. In order to test for possible fragile magnetism, the electrical resistivity was measured with the applied hydrostatic pressure up to 5.22 GPa. The antiferromagnetic transition temperature is decreased down to 236 K by 5.22 GPa. A possible phase transition, of unknown origin, induced by the hydrostatic pressure is detected around 2 GPa.

$PdSn_4$ and $PtSn_4$ have a lot in common in terms of physical properties; structures are same, temperature dependent specific heats are similar, magnetization and resistivity reveals huge anisotropy, and extremely large magnetoresistance (XMR) is observed in both materials. The difference between the two materials are lattice parameters, spin orbit coupling strength, carrier compensation, and presence of the Dirac arc node in the Fermi surface. By comparing and contrasting the physical properties of $PtSn_4$ and $PdSn_4$, we tried to answer why these materials have XMR. Based on our analysis, we ruled out carrier compensation and the Dirac arc node which were suggested as possible origin of XMR. Instead, we observed that the behavior of the temperature and the magnetic field dependent resistivity is captured by the basic metal physics, called Kohler's rule.

Transport and thermal-transport properties of WTe_2 were studied in detail owing to the availability of high quality single crystals. Three dimensionality of the bulk electronic structure as

well as the Lifshitz transition induced by temperature were determined in WTe_2. In addition, the uniaxial strain study shows large non-monotonic elastoresistance and magneto-elastoresistance in WTe_2. From quantum oscillation analysis, DFT calculation and low energy model, we were able to conclude that the strain can be employed to control and dramatically modify electronic transport properties, especially through carrier density changes.

This dissertation contributed to an understanding of tuning bulk properties in layered materials. In particular, we established that strain is a powerful tuning tool. This therefore opens the possibility to combine strain with other experimental techniques on layered materials in the future.

Bibliography

[1] K. S. Novoselov, A. K. Geim, S. V. Morozov, D. Jiang, Y. Zhang, S. V. Dubonos, I. V. Grigorieva, and A. A. Firsov. Electric Field Effect in Atomically Thin Carbon Films. *Science*, 306(5696):666–669, 2004.

[2] Y. Zhang, Y. W. Tan, H. L. Stormer, and P. Kim. Experimental observation of the quantum Hall effect and Berry's phase in graphene. *Nature*, 438:201–204, 2005.

[3] A. H. Castro Neto, F. Guinea, N. M. R. Peres, K. S. Novoselov, and A. K. Geim. The electronic properties of graphene. *Rev. Mod. Phys.*, 81:109–162, 2009.

[4] Sajedeh Manzeli, Dmitry Ovchinnikov, Diego Pasquier, Oleg V Yazyev, and Andras Kis. 2D transition metal dichalcogenides. *Nature Reviews Materials*, 2(8):17033, 2017.

[5] H. Boschker and J. Mannhart. Quantum-Matter Heterostructures. *Annual Review of Condensed Matter Physics*, 8(1):145–164, 2017.

[6] David Johnson, Simon Clarke, John Wiley, and Kunihito Koumoto. Layered materials. *Semiconductor Science and Technology*, 29(6):060301, may 2014.

[7] J.A. Wilson, F.J. Di Salvo, and S. Mahajan. Charge-density waves and superlattices in the metallic layered transition metal dichalcogenides. *Advances in Physics*, 24(2):117–201, 1975.

[8] Shang Gao, Felix Flicker, Raman Sankar, He Zhao, Zheng Ren, Bryan Rachmilowitz, Sidhika Balachandar, Fangcheng Chou, Kenneth S. Burch, Ziqiang Wang, Jasper van Wezel, and Ilija Zeljkovic. Atomic-scale strain manipulation of a charge density wave. *Proceedings of the National Academy of Sciences*, 115(27):6986–6990, 2018.

[9] Mazhar N. Ali, Jun Xiong, Steven Flynn, Jing Tao, Quinn D. Gibson, Leslie M. Schoop, Tian Liang, Neel Haldolaarachchige, Max Hirschberger, N. P. Ong, and R. J. Cava. Large, non-saturating magnetoresistance in WTe_2. *Nature*, 514(7521):205–208, 2014. ISSN 0028-0836.

[10] N. P. Armitage, P. Fournier, and R. L. Greene. Progress and perspectives on electron-doped cuprates. *Rev. Mod. Phys.*, 82:2421–2487, 2010.

[11] A.B. Pippard. *Magnetoresistance in Metals*. Cambridge university press, 1989.

[12] Ilia Mikhailovich Lifshits, M. Ya. Azbel, and M. I. Kaganov. Electron theory of metals. *Plenum Press, New York. 1973, 326 p*, 1973.

[13] J. M Ziman. *Electrons and phonons : the theory of transport phenomena in solids*. Oxford classic texts in the physical sciences Electrons and phonons. Clarendon, Oxford, 2001.

[14] A. A. Abrikosov. *Fundamentals of the theory of metals*. North-Holland : Sole distributors for the USA and Canada, Elsevier Science Pub. Co., Amsterdam ; New York, 1988.

[15] Giuseppe Grosso. *Solid state physics / Giuseppe Grosso, Giuseppe Pastori Parravicini.* 2nd ed.. edition, 2014.

[16] D. Aoki. *Fermi Surface Properties of Rare Earth and Uranium Compounds Grown by the Self-Flux and Chemical Transport Methods*. PhD thesis, Osaka University, 2000.

[17] D. Shoenberg. *Magnetic oscillations in metals*. Cambridge university press, 1984.

[18] IM Lifshitz. ANOMALIES OF ELECTRON CHARACTERISTICS IN THE HIGH PRESSURE REGION. *Zhur. Eksptl'. i Teoret. Fiz.*, 38, 1960.

[19] AA Varlamov, VS Egorov, and AV Pantsulaya. Kinetic properties of metals near electronic topological transitions (2 1/2-order transitions). *Advances in Physics*, 38(5):469–564, 1989.

[20] S. L. Bud'ko, A. N. Voronovskii, A. G. Gapotchenko, and E. S. Itskevich. The Fermi surface of cadmium at an electron-topological phase transition under pressure. *Zh. Eksp. Teor. Fiz*, 86(2):778–783, 1984. [Sov. Phys. JETP **59**, 454 (1984)].

[21] Defen Kang, Yazhou Zhou, Wei Yi, Chongli Yang, Jing Guo, Youguo Shi, Shan Zhang, Zhe Wang, Chao Zhang, Sheng Jiang, et al. Superconductivity emerging from a suppressed large magnetoresistant state in tungsten ditelluride. *Nature communications*, 6:7804, 2015.

[22] Chang Liu, Takeshi Kondo, Rafael M Fernandes, Ari D Palczewski, Eun Deok Mun, Ni Ni, Alexander N Thaler, Aaron Bostwick, Eli Rotenberg, Jörg Schmalian, et al. Evidence for a Lifshitz transition in electron-doped iron arsenic superconductors at the onset of superconductivity. *Nat. Phys.*, 6(6):419–423, 2010.

[23] Chang Liu, AD Palczewski, RS Dhaka, Takeshi Kondo, RM Fernandes, ED Mun, H Hodovanets, AN Thaler, J Schmalian, SL Budko, et al. Importance of the Fermi-surface topology to the superconducting state of the electron-doped pnictide Ba $(Fe_{1-x}\ Co_x)_2\ As_2$. *Phys. Rev. B*, 84(2):020509, 2011.

[24] Yun Wu, Na Hyun Jo, Masayuki Ochi, Lunan Huang, Daixiang Mou, Sergey L Budko, PC Canfield, Nandini Trivedi, Ryotaro Arita, and Adam Kaminski. Temperature-induced Lifshitz transition in WTe_2. *Phys. Rev. Lett.*, 115(16):166602, 2015.

[25] John Frederick Nye et al. *Physical properties of crystals: their representation by tensors and matrices*. Oxford university press, 1985.

[26] Yongke Sun, Scott E Thompson, and Toshikazu Nishida. *Strain effect in semiconductors: theory and device applications*. Springer Science & Business Media, 2009.

[27] Hsueh-Hui Kuo, Maxwell C. Shapiro, Scott C. Riggs, and Ian R. Fisher. Measurement of the elastoresistivity coefficients of the underdoped iron arsenide $Ba(Fe_{0.975}Co_{0.025})_2As_2$. *Phys. Rev. B*, 88:085113, 2013.

[28] Robert E Newnham. *Properties of materials: anisotropy, symmetry, structure*. Oxford University Press on Demand, 2005.

[29] Udhara S. Kaluarachchi, Valentin Taufour, Aashish Sapkota, Vladislav Borisov, Tai Kong, William R. Meier, Karunakar Kothapalli, Benjamin G. Ueland, Andreas Kreyssig, Roser

Valentí, Robert J. McQueeney, Alan I. Goldman, Sergey L. Bud'ko, and Paul C. Canfield. Pressure-induced half-collapsed-tetragonal phase in $CaKFe_4As_4$. *Phys. Rev. B*, 96:140501, 2017.

[30] James M Gere. *Mechanics of Materials, ; Brooks*. Cole, Pacific Grove, CA, 2004.

[31] C.W.J. Beenakker. Search for Majorana Fermions in Superconductors. *Annual Review of Condensed Matter Physics*, 4(1):113–136, 2013.

[32] Brian R Pamplin. *Crystal Growth: International Series on the Science of the Solid State*. Elsevier, 2013.

[33] H. Okamoto. *Phase Diagrams for Binary Alloys, Desk Handbook*. ASM International, Materials Park, OH, 2000.

[34] Paul C. Canfield, Tai Kong, Udhara S. Kaluarachchi, and Na Hyun Jo. Use of frit-disc crucibles for routine and exploratory solution growth of single crystalline samples. *Philos. Mag.*, 96(1):84–92, 2016.

[35] Cedomir Petrovic, Paul C. Canfield, and Jonathan Y. Mellen. Growing intermetallic single crystals using in situ decanting. *Philos. Mag.*, 92(19-21):2448–2457, 2012.

[36] P. C. Canfield and Z. Fisk. Growth of single crystals from metallic fluxes. *Philos. Mag. B*, 65(6):1117–1123, 1992.

[37] Xiao Lin. *Development and exploration of potential routes of discovery of new superconductors*. PhD thesis, Iowa State University, 2013.

[38] Maryadele J O'Neil. *The Merck index: an encyclopedia of chemicals, drugs, and biologicals*. RSC Publishing, 2013.

[39] S Ohta, T Kanomata, T Kaneko, and H Yoshida. Pressure effect on the Curie temperature and thermal expansion of CrTe. *J. Phys.: Condens. Matter*, 5(17):2759, 1993.

[40] B.E. Brown. The crystal structures of WTe_2 and high-temperature $MoTe_2$. *Acta Crystallogr.*, 2:268–274, 1966.

[41] Charles Kittel. *Introduction to Solid State Physics*. Wiley, 8th edition, 2005.

[42] Armel Le Bail. Whole powder pattern decomposition methods and applications: A retrospection. *Powder Diffraction*, 20(4):316–326, 2005.

[43] A. Jesche, M. Fix, A. Kreyssig, W. R. Meier, and P. C. Canfield. X-Ray diffraction on large single crystals using a powder diffractometer. *Philos. Mag.*, 96(20):2115–2124, 2016.

[44] Jih Shang Hwang, Kai Jan Lin, and Cheng Tien. Measurement of heat capacity by fitting the whole temperature response of a heat-pulse calorimeter. *Review of Scientific Instruments*, 68 (1):94–101, 1997.

[45] Eundeok Mun, Sergey L Bud'ko, Milton S Torikachvili, and Paul C Canfield. Experimental setup for the measurement of the thermoelectric power in zero and applied magnetic field. *Measurement Science and Technology*, 21(5):055104, 2010.

[46] H. Hodovanets. *Tuning of 4f- and Fe-based correlated electron systems by magnetic field and chemical substitution*. PhD thesis, Iowa State University, 2014.

[Instruments] Razorbill Instruments. *Datasheet: CS100*. URL https://razorbillinstruments.com/uniaxial-strain-cell/.

[47] M. S. Ikeda, T. Worasaran, J. C. Palmstrom, J. A. W. Straquadine, P. Walmsley, and I. R. Fisher. Symmetric and antisymmetric strain as continuous tuning parameters for electronic nematic order. *Phys. Rev. B*, 98:245133, 2018.

[48] Na Hyun Jo, Udhara S. Kaluarachchi, Yun Wu, Daixiang Mou, Lunan Huang, Valentin Taufour, Adam Kaminski, Sergey L. Bud'ko, and Paul C. Canfield. Anisotropic physical properties and pressure dependent magnetic ordering of $CrAuTe_4$. *Phys. Rev. B*, 94:184413, 2016.

[49] Paul C Canfield and Sergey L Budko. Preserved entropy and fragile magnetism. *Rep. Prog. Phys.*, 79(8):084506, 2016.

[50] D. B. McWhan and T. M. Rice. Pressure Dependence of Itinerant Antiferromagnetism in Chromium. *Phys. Rev. Lett.*, 19:846–849, 1967.

[51] Eric Fawcett. Spin-density-wave antiferromagnetism in chromium. *Rev. Mod. Phys.*, 60: 209–283, 1988.

[52] E. Fawcett, H. L. Alberts, V. Yu. Galkin, D. R. Noakes, and J. V. Yakhmi. Spin-density-wave antiferromagnetism in chromium alloys. *Rev. Mod. Phys.*, 66:25–127, 1994.

[53] A. Yeh, Yeong-Ah Soh, J. Brooke, G. Aeppli, T. F. Rosenbaum, and S. M. Hayden. Quantum phase transition in a common metal. *Nature*, 419(6906):459–462, 2002. ISSN 0028-0836.

[54] M. Lee, A. Husmann, T. F. Rosenbaum, and G. Aeppli. High Resolution Study of Magnetic Ordering at Absolute Zero. *Phys. Rev. Lett.*, 92:187201, 2004.

[55] Yejun Feng, R. Jaramillo, G. Srajer, J. C. Lang, Z. Islam, M. S. Somayazulu, O. G. Shpyrko, J. J. Pluth, H.-k. Mao, E. D. Isaacs, G. Aeppli, and T. F. Rosenbaum. Pressure-Tuned Spin and Charge Ordering in an Itinerant Antiferromagnet. *Phys. Rev. Lett.*, 99:137201, 2007.

[56] R. Jaramillo, Yejun Feng, J. Wang, and T. F. Rosenbaum. Signatures of quantum criticality in pure Cr at high pressure. *Proceedings of the National Academy of Sciences*, 107(31): 13631–13635, 2010.

[57] Wei Wu, Jinguang Cheng, Kazuyuki Matsubayashi, Panpan Kong, Fukun Lin, Changqing Jin, Nanlin Wang, Yoshiya Uwatoko, and Jianlin Luo. Superconductivity in the vicinity of antiferromagnetic order in CrAs. *Nat. Comm.*, 5:–, 2014.

[58] Piers Coleman and Andrew J. Schofield. Quantum criticality. *Nature*, 433(7023):226–229, 2005. ISSN 0028-0836.

[59] Thomas K. Reynolds, Michael A. McGuire, and Francis J. DiSalvo. Thermoelectric properties and antiferromagnetism of the new ternary transition metal telluride $CrAuTe_4$. *J. Solid State Chem.*, 177(9):2998 – 3006, 2004. ISSN 0022-4596.

[60] D. C. Johnston. Magnetic susceptibility of collinear and noncollinear heisenberg antiferromagnets. *Phys. Rev. Lett.*, 109:077201, 2012.

[61] David C. Johnston. Unified molecular field theory for collinear and noncollinear Heisenberg antiferromagnets. *Phys. Rev. B*, 91:064427, 2015.

[62] Michael E. Fisher. Relation between the Specific Heat and Susceptibility of an Antiferromagnet. *Philos. Mag.*, 7(82):1731–1743, 1962.

[63] Michael E. Fisher and J. S. Langer. Resistive Anomalies at Magnetic Critical Points. *Phys. Rev. Lett.*, 20:665–668, 1968.

[64] Rui Jiang, Daixiang Mou, Yun Wu, Lunan Huang, Colin D. McMillen, Joseph Kolis, Henry G. Giesber, John J. Egan, and Adam Kaminski. Tunable vacuum ultraviolet laser based spectrometer for angle resolved photoemission spectroscopy. *Rev. Sci. Instrum.*, 85(3):033902, 2014.

[65] Takeshi Kondo, R. M. Fernandes, R. Khasanov, Chang Liu, A. D. Palczewski, Ni Ni, M. Shi, A. Bostwick, E. Rotenberg, J. Schmalian, S. L. Bud'ko, P. C. Canfield, and A. Kaminski. Unexpected Fermi-surface nesting in the pnictide parent compounds $BaFe_2As_2$ and $CaFe_2As_2$ revealed by angle-resolved photoemission spectroscopy. *Phys. Rev. B*, 81:060507, 2010.

[66] S. K. Kim, M. S. Torikachvili, E. Colombier, A. Thaler, S. L. Bud'ko, and P. C. Canfield. Combined effects of pressure and Ru substitution on $BaFe_2As_2$. *Phys. Rev. B*, 84:134525, 2011.

[67] M. S. Torikachvili, S. K. Kim, E. Colombier, S. L. Budko, and P. C. Canfield. Solidification and loss of hydrostaticity in liquid media used for pressure measurements. *Rev. Sci. Instrum.*, 86(12):123904, 2015.

[68] E. Colombier and D. Braithwaite. Simple adaptation of the Bridgman high pressure technique for use with liquid media. *Review of Scientific Instruments*, 78(9):093903, 2007.

[69] Naoyuki Tateiwa and Yoshinori Haga. Evaluations of pressure-transmitting media for cryogenic experiments with diamond anvil cell. *Rev. Sci. Instrum.*, 80(12):123901, 2009.

[70] S Klotz, J-C Chervin, P Munsch, and G Le Marchand. Hydrostatic limits of 11 pressure transmitting media. *J. Phys. D: Appl. Phys.*, 42(7):075413, 2009.

[71] G. J. Piermarini, S. Block, and J.D. Barnett. Hydrostatic limits in liquids and solids to 100 kbar. *J. Appl. Phys.*, 44(12):5377–5382, 1973.

[72] B Bireckoven and J Wittig. A diamond anvil cell for the investigation of superconductivity under pressures of up to 50 GPa: Pb as a low temperature manometer. *J. Phys. E: Sci. Instrum.*, 21(9):841, 1988.

[73] A. A. Abrikosov. Quantum magnetoresistance. *Phys. Rev. B*, 58:2788–2794, 1998.

[74] J. E. Schirber and W. J. O'Sullivan. Effect of Hydrostatic Pressure on the Fermi Surface of Bi. *Phys. Rev. B*, 2:2936–2940, 1970.

[75] Na Hyun Jo, Yun Wu, Lin-Lin Wang, Peter P. Orth, Savannah S. Downing, Soham Manni, Dixiang Mou, Duane D. Johnson, Adam Kaminski, Sergey L. Bud'ko, and Paul C. Canfield. Extremely large magnetoresistance and Kohler's rule in $PdSn_4$: A complete study of thermodynamic, transport, and band-structure properties. *Phys. Rev. B*, 96:165145, 2017.

[76] N. P. Armitage, E. J. Mele, and Ashvin Vishwanath. Weyl and Dirac semimetals in three-dimensional solids. *Rev. Mod. Phys.*, 90:015001, 2018.

[77] Z. K. Liu, B. Zhou, Y. Zhang, Z. J. Wang, H. M. Weng, D. Prabhakaran, S.-K. Mo, Z. X. Shen, Z. Fang, X. Dai, Z. Hussain, and Y. L. Chen. Discovery of a Three-Dimensional Topological Dirac Semimetal, Na_3Bi. *Science*, 343(6173):864–867, 2014. ISSN 0036-8075.

[78] Zhijun Wang, Hongming Weng, Quansheng Wu, Xi Dai, and Zhong Fang. Three-dimensional Dirac semimetal and quantum transport in Cd_3As_2. *Phys. Rev. B*, 88:125427, 2013.

[79] Hongming Weng, Xi Dai, and Zhong Fang. Topological semimetals predicted from first-principles calculations. *J. Phys.: Condens. Matter*, 28(30):303001, 2016.

[80] B. Q. Lv, N. Xu, H. M. Weng, J. Z. Ma, P. Richard, X. C. Huang, L. X. Zhao, G. F. Chen, C. E. Matt, F. Bisti, V. N. Strocov, J. Mesot, Z. Fang, X. Dai, T. Qian, M. Shi, and H. Ding. Observation of Weyl nodes in TaAs. *Nat. Phys.*, 11(9):724–727, 2015. ISSN 1745-2473.

[81] Su-Yang Xu, Ilya Belopolski, Nasser Alidoust, Madhab Neupane, Guang Bian, Chenglong Zhang, Raman Sankar, Guoqing Chang, Zhujun Yuan, Chi-Cheng Lee, Shin-Ming Huang, Hao Zheng, Jie Ma, Daniel S. Sanchez, BaoKai Wang, Arun Bansil, Fangcheng Chou, Pavel P. Shibayev, Hsin Lin, Shuang Jia, and M. Zahid Hasan. Discovery of a Weyl fermion semimetal and topological Fermi arcs. *Science*, 349(6248):613–617, 2015. ISSN 0036-8075.

[82] Su-Yang Xu, Nasser Alidoust, Ilya Belopolski, Zhujun Yuan, Guang Bian, Tay-Rong Chang, Hao Zheng, Vladimir N. Strocov, Daniel S. Sanchez, Guoqing Chang, Chenglong Zhang, Daixiang Mou, Yun Wu, Lunan Huang, Chi-Cheng Lee, Shin-Ming Huang, BaoKai Wang, Arun Bansil, Horng-Tay Jeng, Titus Neupert, Adam Kaminski, Hsin Lin, Shuang Jia, and M. Zahid Hasan. Discovery of a Weyl fermion state with Fermi arcs in niobium arsenide. *Nat. Phys.*, 11(9):748–754, 2015. ISSN 1745-2473.

[83] Su-Yang Xu, Ilya Belopolski, Daniel S. Sanchez, Chenglong Zhang, Guoqing Chang, Cheng Guo, Guang Bian, Zhujun Yuan, Hong Lu, Tay-Rong Chang, Pavel P. Shibayev, Mykhailo L. Prokopovych, Nasser Alidoust, Hao Zheng, Chi-Cheng Lee, Shin-Ming Huang, Raman Sankar, Fangcheng Chou, Chuang-Han Hsu, Horng-Tay Jeng, Arun Bansil, Titus Neupert, Vladimir N. Strocov, Hsin Lin, Shuang Jia, and M. Zahid Hasan. Experimental discovery of a topological Weyl semimetal state in TaP. *Sci. Adv.*, 1(10), 2015.

[84] Yun Wu, Daixiang Mou, Na Hyun Jo, Kewei Sun, Lunan Huang, S. L. Bud'ko, P. C. Canfield, and Adam Kaminski. Observation of Fermi arcs in the type-II Weyl semimetal candidate WTe_2. *Phys. Rev. B*, 94:121113, 2016.

[85] Guang Bian, Tay-Rong Chang, Raman Sankar, Su-Yang Xu, Hao Zheng, Titus Neupert, Ching-Kai Chiu, Shin-Ming Huang, Guoqing Chang, Ilya Belopolski, Daniel S. Sanchez, Madhab Neupane, Nasser Alidoust, Chang Liu, BaoKai Wang, Chi-Cheng Lee, Horng-Tay Jeng, Chenglong Zhang, Zhujun Yuan, Shuang Jia, Arun Bansil, Fangcheng Chou, Hsin Lin, and M. Zahid Hasan. Topological nodal-line fermions in spin-orbit metal $PbTaSe_2$. *Nat. Comms.*, 7:10556, 2016.

[86] Leslie M. Schoop, Mazhar N. Ali, Carola Straer, Andreas Topp, Andrei Varykhalov, Dmitry Marchenko, Viola Duppel, Stuart S. P. Parkin, Bettina V. Lotsch, and Christian R. Ast. Dirac cone protected by non-symmorphic symmetry and three-dimensional Dirac line node in ZrSiS. *Nat. Comms.*, 7:11696, May 2016.

[87] Guang Bian, Tay-Rong Chang, Hao Zheng, Saavanth Velury, Su-Yang Xu, Titus Neupert, Ching-Kai Chiu, Shin-Ming Huang, Daniel S. Sanchez, Ilya Belopolski, Nasser Alidoust, Peng-Jen Chen, Guoqing Chang, Arun Bansil, Horng-Tay Jeng, Hsin Lin, and M. Zahid Hasan. Drumhead surface states and topological nodal-line fermions in $TlTaSe_2$. *Phys. Rev. B*, 93: 121113, 2016.

[88] Yun Wu, Lin-Lin Wang, Eundeok Mun, D. D. Johnson, Daixiang Mou, Lunan Huang, Yongbin Lee, S. L. Bud'ko, P. C. Canfield, and Adam Kaminski. Dirac node arcs in $PtSn_4$. *Nat. Phys.*, 12:667, 2016. ISSN 1745-2481.

[89] Eundeok Mun, Hyunjin Ko, Gordon J. Miller, German D. Samolyuk, Sergey L. Bud'ko, and Paul. C. Canfield. Magnetic field effects on transport properties of $PtSn_4$. *Phys. Rev. B*, 85: 035135, 2012.

[90] Mazhar N Ali, Leslie Schoop, Jun Xiong, Steven Flynn, Quinn Gibson, Max Hirschberger, NP Ong, and RJ Cava. Correlation of crystal quality and extreme magnetoresistance of WTe_2. *EPL (Europhysics Letters)*, 110(6):67002, 2015.

[91] Tian Liang, Quinn Gibson, Mazhar N. Ali, Minhao Liu, R. J. Cava, and N. P. Ong. Ultrahigh mobility and giant magnetoresistance in the Dirac semimetalCd_3As_2. *Nat. Mater.*, 14(3):280–284, 2015. ISSN 1476-1122.

[92] F. F. Tafti, Q. D. Gibson, S. K. Kushwaha, N. Haldolaarachchige, and R. J. Cava. Resistivity plateau and extreme magnetoresistance in LaSb. *Nat. Phys.*, 12(3):272–277, 2016. ISSN 1745-2473.

[93] Fazel Fallah Tafti, Quinn Gibson, Satya Kushwaha, Jason W Krizan, Neel Haldolaarachchige, and Robert Joseph Cava. Temperature- field phase diagram of extreme magnetoresistance. *Proc. Natl. Acad. Sci. U.S.A.*, page 201607319, 2016.

[94] R. Kubiak and M. Wolcyrz. Refinement of the crystal structures of $AuSn_4$ and $PdSn_4$. *J. Less Common Met.*, 97:265 – 269, 1984. ISSN 0022-5088.

[95] J. Nyln, F.J. Garcia Garcia, B.D. Mosel, R. Pttgen, and U. Hussermann. Structural relationships, phase stability and bonding of compounds $PdSn_n$ (n=2, 3, 4). *Solid State Sci.*, 6(1): 147 – 155, 2004. ISSN 1293-2558.

[96] Bernd Knnen, Dirk Niepmann, and Wolfgang Jeitschko. Structure refinements and some properties of the transition metal stannides Os_3Sn_7, Ir_5Sn_7, $Ni_{0.402(4)}Pd_{0.598}Sn_4$, α-$PdSn_2$ and $PtSn_4$. *J. Alloys and Compd.*, 309(12):1 – 9, 2000. ISSN 0925-8388.

[97] N. Ni. *Structural / magnetic phase transitions and superconductivity in $Ba(Fe_{1?x}TM_x)_2As_2$ (TM=Co, Ni, Cu, Co / Cu, Rh and Pd) single crystals.* PhD thesis, Iowa State University, 2009.

[98] Yanfei Zhao, Haiwen Liu, Jiaqiang Yan, Wei An, Jun Liu, Xi Zhang, Huichao Wang, Yi Liu, Hua Jiang, Qing Li, Yong Wang, Xin-Zheng Li, David Mandrus, X. C. Xie, Minghu Pan, and

Jian Wang. Anisotropic magnetotransport and exotic longitudinal linear magnetoresistance in WTe_2 crystals. *Phys. Rev. B*, 92:041104, 2015.

[99] Kazuma Eto, Zhi Ren, A. A. Taskin, Kouji Segawa, and Yoichi Ando. Angular-dependent oscillations of the magnetoresistance in Bi_2Se_3 due to the three-dimensional bulk Fermi surface. *Phys. Rev. B*, 81:195309, 2010.

[100] F. Rullier-Albenque, D. Colson, A. Forget, and H. Alloul. Hall Effect and Resistivity Study of the Magnetic Transition, Carrier Content, and Fermi-Liquid Behavior in $Ba(Fe_{1-x}Co_x)_2As_2$. *Phys. Rev. Lett.*, 103:057001, 2009.

[101] F. Rullier-Albenque, D. Colson, A. Forget, P. Thuéry, and S. Poissonnet. Hole and electron contributions to the transport properties of $Ba(Fe_{1-x}Ru_x)_2As_2$ single crystals. *Phys. Rev. B*, 81:224503, 2010.

[102] Yongkang Luo, H. Li, Y. M. Dai, H. Miao, Y. G. Shi, H. Ding, A. J. Taylor, D. A. Yarotski, R. P. Prasankumar, and J. D. Thompson. Hall effect in the extremely large magnetoresistance semimetal WTe_2. *Appl. Phys. Lett.*, 107(18):182411, 2015.

[103] Edward A Boudreaux and LN Mulay. *Theory and applications of molecular paramagnetism*. Wiley New York, 1976.

[104] Gordon A. Bain and John F. Berry. Diamagnetic Corrections and Pascal's Constants. *J. Chem. Educ.*, 85(4):532, 2008.

[105] Stephen Blundell. *Magnetism in Condensed Matter*. Oxford New York, 2001.

[106] Wenshuai Gao, Ningning Hao, Fa-Wei Zheng, Wei Ning, Min Wu, Xiangde Zhu, Guolin Zheng, Jinglei Zhang, Jianwei Lu, Hongwei Zhang, Chuanying Xi, Jiyong Yang, Haifeng Du, Ping Zhang, Yuheng Zhang, and Mingliang Tian. Extremely Large Magnetoresistance in a Topological Semimetal Candidate Pyrite $PtBi_2$. *Phys. Rev. Lett.*, 118:256601, 2017.

[107] P. S. Alekseev, A. P. Dmitriev, I. V. Gornyi, V. Yu. Kachorovskii, B. N. Narozhny, M. Schütt, and M. Titov. Magnetoresistance of compensated semimetals in confined geometries. *Phys. Rev. B*, 95:165410, 2017.

[108] P. Hohenberg and W. Kohn. Inhomogeneous Electron Gas. *Phys. Rev.*, 136:B864–B871, 1964.

[109] W. Kohn and L. J. Sham. Self-Consistent Equations Including Exchange and Correlation Effects. *Phys. Rev.*, 140:A1133–A1138, 1965.

[110] John P. Perdew, Kieron Burke, and Matthias Ernzerhof. Generalized Gradient Approximation Made Simple. *Phys. Rev. Lett.*, 77:3865–3868, 1996.

[111] P. E. Blöchl. Projector augmented-wave method. *Phys. Rev. B*, 50:17953–17979, 1994.

[112] G. Kresse and J. Furthmüller. Efficient iterative schemes for ab initio total-energy calculations using a plane-wave basis set. *Phys. Rev. B*, 54:11169–11186, 1996.

[113] G. Kresse and J. Furthmller. Efficiency of ab-initio total energy calculations for metals and semiconductors using a plane-wave basis set. *Comput.Mater. Sci*, 6(1):15 – 50, 1996. ISSN 0927-0256.

[114] Hendrik J. Monkhorst and James D. Pack. Special points for Brillouin-zone integrations. *Phys. Rev. B*, 13:5188–5192, 1976.

[115] Nicola Marzari and David Vanderbilt. Maximally localized generalized Wannier functions for composite energy bands. *Phys. Rev. B*, 56:12847–12865, 1997.

[116] Ivo Souza, Nicola Marzari, and David Vanderbilt. Maximally localized Wannier functions for entangled energy bands. *Phys. Rev. B*, 65:035109, 2001.

[117] Nicola Marzari, Arash A. Mostofi, Jonathan R. Yates, Ivo Souza, and David Vanderbilt. Maximally localized Wannier functions: Theory and applications. *Rev. Mod. Phys.*, 84:1419–1475, 2012.

[118] D. H. Lee and J. D. Joannopoulos. Simple scheme for surface-band calculations. I. *Phys. Rev. B*, 23:4988–4996, 1981.

[119] D. H. Lee and J. D. Joannopoulos. Simple scheme for surface-band calculations. II. The Green's function. *Phys. Rev. B*, 23:4997–5004, 1981.

[120] M P Lopez Sancho, J M Lopez Sancho, and J Rubio. Quick iterative scheme for the calculation of transfer matrices: application to Mo (100). *Journal of Physics F: Metal Physics*, 14(5): 1205, 1984.

[121] M P Lopez Sancho, J M Lopez Sancho, J M L Sancho, and J Rubio. Highly convergent schemes for the calculation of bulk and surface Green functions. *Journal of Physics F: Metal Physics*, 15(4):851, 1985.

[122] QuanSheng Wu, ShengNan Zhang, Hai-Feng Song, Matthias Troyer, and Alexey A. Soluyanov. WannierTools: An open-source software package for novel topological materials. *Computer Physics Communications*, 224:405 – 416, 2018. ISSN 0010-4655.

[123] John M Ziman. *Electrons and phonons: the theory of transport phenomena in solids*. Oxford university press, 1960.

[124] Yun Wu, Na Hyun Jo, Daixiang Mou, Lunan Huang, S. L. Bud'ko, P. C. Canfield, and Adam Kaminski. Three-dimensionality of the bulk electronic structure in WTe_2. *Phys. Rev. B*, 95: 195138, 2017.

[125] N. H Jo, L. L. Wang, P. P. Orth, S. L. Bud'ko, and P. C. Canfield. Phenomenal magneto-elastoresistance of WTe_2: strain engineering of electronic and quantum transport properties. *arXiv*, (1901.05090), 2019.

[126] Zengwei Zhu, Xiao Lin, Juan Liu, Benoît Fauqué, Qian Tao, Chongli Yang, Youguo Shi, and Kamran Behnia. Quantum Oscillations, Thermoelectric Coefficients, and the Fermi Surface of Semimetallic WTe_2. *Phys. Rev. Lett.*, 114:176601, 2015.

[127] P. L. Cai, J. Hu, L. P. He, J. Pan, X. C. Hong, Z. Zhang, J. Zhang, J. Wei, Z. Q. Mao, and S. Y. Li. Drastic Pressure Effect on the Extremely Large Magnetoresistance in WTe_2: Quantum Oscillation Study. *Phys. Rev. Lett.*, 115:057202, Jul 2015.

[128] R. S. Dhaka, S. E. Hahn, E. Razzoli, Rui Jiang, M. Shi, B. N. Harmon, A. Thaler, S. L. Bud'ko, P. C. Canfield, and Adam Kaminski. Unusual Temperature Dependence of Band Dispersion in $Ba(Fe_{1-x}Ru_x)_2As_2$ and its Consequences for Antiferromagnetic Ordering. *Phys. Rev. Lett.*, 110:067002, 2013.

[129] V. Brouet, Ping-Hui Lin, Y. Texier, J. Bobroff, A. Taleb-Ibrahimi, P. Le Fèvre, F. Bertran, M. Casula, P. Werner, S. Biermann, F. Rullier-Albenque, A. Forget, and D. Colson. Large Temperature Dependence of the Number of Carriers in Co-Doped $BaFe_2As_2$. *Phys. Rev. Lett.*, 110:167002, 2013.

[130] G. C. Kuczynski. Effect of Elastic Strain on the Electrical Resistance of Metals. *Phys. Rev.*, 94:61–64, 1954.

[131] A.V. Kolobov and J. Tominaga. *Bulk TMDCs: Review of Structure and Properties. In: Two-Dimensional Transition Metal Dichalcogenides.*, volume 239 of *Springer Series in Materials Science*. Springer, Cham, 2016.

[132] F. Zeng, W. B. Zhang, and B. Y. Tang. Electronic structures and elastic properties of monolayer and bilayer transition metal dichalcogenides MX_2 (M = Mo, W; X = O, S, Se, Te): A comparative first-principles study. *Chinese Phys B*, 24:097103, 2015.

[133] S. R. Rourke, P. M. C.; Julian. Numerical extraction of de Haas-van Alphen frequencies from calculated band energies. *Computer Physics Communications*, 183:324–332, 2012.

[134] I. Pletikosić, Mazhar N. Ali, A. V. Fedorov, R. J. Cava, and T. Valla. Electronic Structure Basis for the Extraordinary Magnetoresistance in WTe_2. *Phys. Rev. Lett.*, 113:216601, 2014.

[135] H. Smith and H. H. Jensen. *Transport Phenomena*. Oxford University Press, Oxford, U.K., 1989.

[136] Daniel O. Brodsky, Mark E. Barber, Jan A. N. Bruin, Rodolfo A. Borzi, Santiago A. Grigera, Robin S. Perry, Andrew P. Mackenzie, and Clifford W. Hicks. Strain and vector magnetic field tuning of the anomalous phase in $Sr_3Ru_2O_7$. *Science Advances*, 3(2), 2017.

[137] Jaesung Lee, Fan Ye, Zenghui Wang, Rui Yang, Jin Hu, Zhiqiang Mao, Jiang Wei, and Philip X.-L. Feng. Single- and few-layer WTe_2 and their suspended nanostructures: Raman signatures and nanomechanical resonances. *Nanoscale*, 8:7854–7860, 2016.

[138] Clifford W. Hicks, Mark E. Barber, Stephen D. Edkins, Daniel O. Brodsky, and Andrew P. Mackenzie. Piezoelectric-based apparatus for strain tuning. *Review of Scientific Instruments*, 85(6):065003, 2014.

[139] B. J. Ceperley, D. M.; Alder. Ground-State of the Electron-Gas by a Stochastic Method. *Phys Rev Lett*, 45:566–569, 1980.

[140] A. Perdew, J. P.; Zunger. Self-Interaction Correction to Density-Functional Approximations for Many-Electron Systems. *Phys Rev B*, 23:5048–5079, 1981.

[141] Arthur Mar, Stephane Jobic, and James A. Ibers. Metal-metal vs tellurium-tellurium bonding in WTe_2 and its ternary variants $TaIrTe_4$ and $NbIrTe_4$. *Journal of the American Chemical Society*, 114(23):8963–8971, 1992.

[142] Georg K.H. Madsen and David J. Singh. BoltzTraP. A code for calculating band-structure dependent quantities. *Computer Physics Communications*, 175(1):67 – 71, 2006. ISSN 0010-4655.

[143] Domenico Di Sante, Pranab Kumar Das, C. Bigi, Z. Ergönenc, N. Gürtler, J. A. Krieger, T. Schmitt, M. N. Ali, G. Rossi, R. Thomale, C. Franchini, S. Picozzi, J. Fujii, V. N. Strocov, G. Sangiovanni, I. Vobornik, R. J. Cava, and G. Panaccione. Three-Dimensional Electronic Structure of the Type-II Weyl Semimetal WTe_2. *Phys. Rev. Lett.*, 119:026403, Jul 2017.

[144] Y. Kanda and Y. Kanda. A graphical representation of the piezoresistance coefficients in silicon. *IEEE Transactions on Electron Devices*, 29:64–70, 1982.

[145] Inga Schellenberg, Ulrike Pfannenschmidt, Matthias Eul, Christian Schwickert, and Rainer Pttgen. A 121Sb and 151Eu Mssbauer Spectroscopic Investigation of $EuCd_2X_2$ (X = P, As, Sb) and $YbCd_2Sb_2$. *Zeitschrift fr anorganische und allgemeine Chemie*, 637(12):1863–1870, 2011.

[146] H. P. Wang, D. S. Wu, Y. G. Shi, and N. L. Wang. Anisotropic transport and optical spectroscopy study on antiferromagnetic triangular lattice $EuCd_2As_2$: An interplay between magnetism and charge transport properties. *Phys. Rev. B*, 94:045112, 2016.

[147] Guiyuan Hua, Simin Nie, Zhida Song, Rui Yu, Gang Xu, and Kailun Yao. Dirac semimetal in type-IV magnetic space groups. *Phys. Rev. B*, 98:201116, 2018.

[148] M. C. Rahn, J.-R. Soh, S. Francoual, L. S. I. Veiga, J. Strempfer, J. Mardegan, D. Y. Yan, Y. F. Guo, Y. G. Shi, and A. T. Boothroyd. Coupling of magnetic order and charge transport in the candidate Dirac semimetal $EuCd_2As_2$. *Phys. Rev. B*, 97:214422, 2018.

[149] L. L. Wang, N. H. Jo, B. Kuthanazhi, Y. Wu, R. J. McQueeney, A. Kaminski, and P. C. Canfield. A Single Pair of Weyl Fermions in Half-metallic $EuCd_2As_2$ Semimetal. *arXiv*, (1901.08234), 2019.

[150] Na Hyun Jo, Qisheng Lin, Manh Cuong Nguyen, Udhara S. Kaluarachchi, William R. Meier, Soham Manni, Savannah S. Downing, Anna E. Bhmer, Tai Kong, Yang Sun, Valentin Taufour, Cai-Zhuang Wang, Kai-Ming Ho, Sergey L. Budko, and Paul C. Canfield. Growth and characterization of BaZnGa. *Philosophical Magazine*, 97(35):3317–3324, 2017.

[151] Na Hyun Jo, Li Xiang, Udhara S. Kaluarachchi, Morgan Masters, Kathryn Neilson, Savannah S. Downing, Paul C. Canfield, and Sergey L. Bud'ko. Pressure induced change in the electronic state of $Ta_4Pd_3Te_{16}$. *Phys. Rev. B*, 95:134516, 2017.

[152] W. R. Meier, T. Kong, U. S. Kaluarachchi, V. Taufour, N. H. Jo, G. Drachuck, A. E. Böhmer, S. M. Saunders, A. Sapkota, A. Kreyssig, M. A. Tanatar, R. Prozorov, A. I. Goldman, Fedor F.

Balakirev, Alex Gurevich, S. L. Bud'ko, and P. C. Canfield. Anisotropic thermodynamic and transport properties of single-crystalline $CaKFe_4As_4$. *Phys. Rev. B*, 94:064501, 2016.

[153] E. M. Levin, T. M. Riedemann, A. Howard, N. H. Jo, S. L. Budko, P. C. Canfield, and T. A. Lograsso. ^{125}Te NMR and seebeck effect in Bi_2Te_3 synthesized from stoichiometric and Te-rich melts. *The Journal of Physical Chemistry C*, 120(44):25196–25202, 2016.

[154] Sergey L. Budko, Na Hyun Jo, Savannah S. Downing, and Paul C. Canfield. On magnetic structure of $CuFe_2Ge_2$: Constrains from the ^{57}Fe Mössbauer spectroscopy. *Journal of Magnetism and Magnetic Materials*, 446:260 – 263, 2018. ISSN 0304-8853.

[155] Andrew F May, Stuart Calder, David S Parker, Brian C Sales, and Michael A McGuire. Competing magnetic ground states and their coupling to the crystal lattice in $CuFe_2Ge_2$. *Scientific reports*, 6:35325, 2016.

[156] K. V. Shanavas and David J. Singh. Itinerant Magnetism in Metallic $CuFe_2Ge_2$. *PLOS ONE*, 10(3):1–9, 2015.

[157] B. G. Ueland, N. H. Jo, A. Sapkota, W. Tian, M. Masters, H. Hodovanets, S. S. Downing, C. Schmidt, R. J. McQueeney, S. L. Bud'ko, A. Kreyssig, P. C. Canfield, and A. I. Goldman. Reduction of the ordered magnetic moment and its relationship to Kondo coherence in $Ce_{1-x}La_xCu_2Ge_2$. *Phys. Rev. B*, 97:165121, 2018.

[158] Elizabeth L. Kunz Wille, Na Hyun Jo, James C. Fettinger, Paul C. Canfield, and Susan M. Kauzlarich. Single crystal growth and magnetic properties of the mixed valent Yb containing Zintl phase, $Yb_{14}MgSb_{11}$. *Chem. Commun.*, 54:12946–12949, 2018.

[159] I. R. Fisher, S. L. Bud'ko, C. Song, P. C. Canfield, T. C. Ozawa, and S. M. Kauzlarich. $Yb_{14}ZnSb_{11}$: Charge Balance in Zintl Compounds as a Route to Intermediate Yb Valence. *Phys. Rev. Lett.*, 85:1120–1123, 2000.

[160] S. Teknowijoyo, Na Hyun Jo, Mathias S. Scheurer, M. A. Tanatar, Kyuil Cho, S. L. Bud'ko, Peter P. Orth, P. C. Canfield, and R. Prozorov. Nodeless superconductivity in the type-II

Dirac semimetal $PdTe_2$: London penetration depth and pairing-symmetry analysis. *Phys. Rev. B*, 98:024508, 2018.

APPENDIX A. LIST OF Te/Se CONTAINED CRYSTAL GROWTHS

Table A.1 List of Te/Se contained crystal growths I

Sample ID#	Initial composition	T_{high} (C)	T_{decant} (C)	Comments
TU174	Bi25Te75	580	440	Bi2Te3
TU202	(Bi0.25Te0.75)95Rh5	580	440	Not sure Rh doping
TU216	Nb3Te97	900	460	NbTe4
TU217	W1Te99	900	460	WTe2
TU255	Cr5Au5Te90	900	500	Cr5Te8
TU263	W1Te99	1000	460	WTe2
TU264	W2Te98	1000	460	WTe2
TU269	Cr5Te67Au28	900	500	Cr5Te8 &CrAuTe4
TU280	Fe5Au28Te67	900	500	FeTe2&AuTe2
TU281	Co5Au28Te67	900	500	CoTe2+AuTe2
TU282	Ni5Au28Te67	900	500	NiTe2+AuTe2
TU292	Zr6Te94	1000	560	ZrTe3
TU295	Hf4Te96	800	500	HfTe5
TU296	Cr3Au30Te67	900	500	Cr5Te8&CrAuTe4
TU326	Zr4Te96	1000	560	ZrTe3
TU336	Hf10Te90	1000	600	
TU337	Sb15Te85	700	450	Sb2Te3
TU338	Sb10Te85V5	700	450	VTe2
TU339	Sb7.5Te857.5	700	450	VTe2
TU348	Zr4Te96	1000	560	ZrTe3
TU401	Cr1.5Au31.5Te67	900	500	Cr5Te8&CrAuTe4
TU402	Cr5Au40Te55	900	500	Cr5Te8
TU437	Ta1Te99	800	520	Total spin
TU455	Ta1Te99	800	470	Really big, TaTe4
TU459	Cr3Au30Te67	900	500	Cr5Te8
TU466	Ta2Te98	800	470	Bird nest, TaTe4
TU467	Ta3Te97	800	470	Bird nest, TaTe4
TU471	Ta1Te99	800	470	Really big TaTe4, Best
TU487	Cr3Au30Te67	900	750	Total spin
TU488	Cr4Co2Te94	900	500	Cr5Te8&CoTe2
TU499	Cr5Te78Ge17	900	500	CrGeTe3
TU500	B2Te98	900	500	Looks like B did not melt.
TU502	Cr5Te78Ge17	900	500	CrGeTe3
TU503	Cr5Te78Si17	900	500	CrSiTe3
TU504	(B0.13Cr0.87)5Te78Ge17	900	500	CrGeTe3, B did not go in at all.

Table A.2 List of Te/Se contained crystal growths II

Sample ID#	Initial composition	T_{high} (C)	T_{decant} (C)	Comments
TU512	Cu32Mn5Te63	750	470	MnTe2
TU533	Mn_5Cu_40Te_55	950	550	Cu2Mn2Te2 and binaries, Dendrite
TU534	Mn_5Cu_45Te_50	950	550	Cu2Mn2Te2 and binaries, Dendrite
TU627	Mn5Cu45Te50	900	550	Cu2Mn2Te2 and binaries, Dendrite
TU635	Cr5Au25Te70	900	500	Cr5Te8&CrAuTe4
TU636	Cr5Au30Te65	900	500	Cr5Te8&CrAuTe4
TU637	Mn10Cu40Te50	950	550	Similar to previous
TU647	Tb3Ag32Te65	1000	400	Binaries
TU648	Tb6Ag31Te63	1000	400	Binaries
TU649	Cr3Ag32Te65	1000	400	Binaries
TU650	Cr6Ag31Te63	1000	400	Binaries
TU653	Cr3Eu2Te95	800	500	Cr5Te8
TU654	Cr5Au20Te75	900	500	Cr5Te8&CrAuTe4
TU655	Cr5Au15Te80	900	500	Cr5Te8
TU665	Ag58Te42	900	500	Alpha Ag2Te and Ag5Te3 dendrites
TU666	Ag57Te43	900	500	Alpha Ag2Te and Ag5Te3 dendrites
TU667	Tb7Ag37Te56	1000	475	Binaries
TU668	Tb7Ag42Te51	1000	475	Binaries
TU669	Eu10Cr5Te85	800	500	Cr5Te8
TU674	Cr2Au30Te68	900	500	Cr5Te8&CrAuTe4, Best batch for CrAuTe4
TU675	Cr2Au28Te70	900	500	Cr5Te8&CrAuTe4
TU689	Tb23Ag80Te7	900	500	no spin
TU701	Tb13Ag80Te7	1000	825	got binaries
TU753	Cr10As30Te60	900	450	A nice yield of flat crystals
TU757	Cr3Ag32Te63	900	600	grew a binary
TU851	Ta2PdTe97	1000	500	nice rod-like samples
TU852	Ta4Pd2Te94	1000	500	TaTe4
TU864	Pd2Ta2Te96	1000	550	TaTe4
TU865	Pd4Ta2Te94	1000	550	Similar to previous
TU867	(Y5Fe2Te2)3Sn97	1000	800	Binaries
Ml171b	Pt4Te96	900	500	PtTe2
Ml172b	Pd10Te90	900	500	PdTe2
ML213a	Nb3Ni3Te94	1000	600	NbTe4+NbNiTe5
ML214a	Nb6Ni6Te88	1000	600	NbTe4+NbNiTe5
ML247	Nb6Ni6Te88	1000	800	Total spin
ML248	Nb10Ni10Te80	1000	800	NbTe2
ML257	TaPtTe98	1000	600	PtTe2
ML261	Zr2Ti2Te96	1000	600	ZrTe3
ML262	IrNbTe98	1000	600	Ir3Te8
ML264	Nb6Ni6Te88	1000	700	Total spin
ML265	Ni34Te66	1100	30	Eutectic check
ML266	Nb6Ni6Te88	1000	650	NbNiTe5&binaries
ML267	Ta2PtTe97	1000	600	PtTe2
ML276	Zr2Ti4Te94	1000	600	ZrTe3
ML277	Zr2Ti8Te90	1000	600	ZrTe3&TiTe2
ML278	Ni66Te34	1100	30	Eutectic check
ML279	IrNb2Te97	1000	600	NbTe4&Ir3Te8
ML280	IrNb4Te95	1000	600	NbTe4
ML284	Nb3Ni47Te50	1100	875	NbNiTe2
ML285	Nb6Ni44Te50	1100	875	NbNiTe2

Table A.3 List of Te/Se contained crystal growths III

Sample ID#	Initial composition	T_{high} (C)	T_{decant} (C)	Comments
ML289	Bi25Te75	580	440	Bi2Te3
ML295	Nb3Ni60Te37	1100	1005	NbNi3
ML296	Nb6Ni56Te38	1100	1005	NbNi3
ML301	Nb3Ni30Te67	1100	800	NbTe2&NaTe4
ML352	Ir2Nb2Te8In88	1000	500	Binaries
ML353	(IrNbTe4)2In98	1000	500	Binaries
ML377	Ta4Pd6Te90	1000	500	Ta3Pd3Te14&Ta4Pd3Te16
ML378	Ta8Pd12Te80	1000	500	Ta3Pd3Te14&Ta4Pd3Te16
ML379	Ta10Pd15Te75	1000	500	PdTe2
ML383	Ta10Pd15Te75	1000	600	Ta4Pd3Te16&PdTe2
ML384	Ta15Pd10Te75	1000	600	Ta4Pd3Te16&PdTe2
ML391	Ta10Pd15Te75	1000	700	Ta4Pd3Te16&PdTe2
ML392	Ta15Pd10Te75	1000	700	Ta4Pd3Te16&PdTe2
ML415	Ta10Pd15Te75	1000	600	Ta4Pd3Te16&PdTe2
ML416	Ta10Pd15Te75	1000	700	Ta4Pd3Te16&PdTe2
ML431	Ti5(Au46Te54(95	1000	500	TiTe2
ML432	Ti5(Au13Te87)95	1000	500	Binaries
ML446	Ti3Au3Te94	1000	500	TiAu arcmelt
ML458	Te50Ge5Ni45	1100	870	reseal
ML459	Te48Ge5Ni47	1100	870	reseal
ML480	Ti10Au36Te54	1000	500	TiTe2&binaries
ML510a	Ta10Pd15Te75	1000	700	Ta4Pd3Te16&PdTe2
ML511a	Ta10Pd15Te75	1000	700	Ta4Pd3Te16&PdTe2
ML512	Ta10Pd15Te75	1000	700	Ta4Pd3Te16&PdTe2
ML522	Ta10Pd15Te75	1000	750	Ta4Pd3Te16&PdTe2
ML573	W2Te98	1000	460	WTe2
ML574	W2Te98	1000	460	WTe2
ML624	W2Te98	1000	460	WTe2
ML625	W2Te98	1000	460	WTe2
ML 684	Yb5(Aq34Te66)95	1000	425	TbTe&binaries
ML695	Yb3(Ag34Te66)97	1000	600	TbTe&binaries
ML712	Pd10Te90	900	500	PdTe2
ML713	Pt4Te96	900	500	PtTe2
ML728	Gd5(Sb70Te30)95	1100	600	Binaries
ML737	Gd5(Sb70Te30)95	1100	650	Binaries
ML751	Pd10Te90	900	500	PdTe2
ML752	Pd10Te90	900	500	PdTe2
ML759	Gd5Sb90Te15	1100	650	Binaries
ML767	Cr5Te78Ge17	900	500	CrGeTe3
ML768	Cr5Te78Si17	900	500	CrSiTe3
ML773	Sn35Te65	750	450	SnTe
ML811	Gd5Ag31Te64	900	500	Binaries
ML816	Gd2Ag32Te66	850	450	Binaries
ML880	TaPtTe98	1000	600	PtTe2
ML881	TaPtTe98	1000	600	Total spin
ML882	TaPtTe98	1000	600	Total spin
ML883	Ta2Ni2Te96	1000	500	Total spin
ML884	(Ta3Pt)Te99	1000	600	Total spin
ML888	TaNiTe98	1000	500	Total spin
ML889	Ta2Ni2Te96	1000	500	Binaries
ML890	(Ta3Pt)Te99	1000	500	Binaries

Table A.4 List of Te/Se contained crystal growths IV

Sample ID#	Initial composition	T_{high} (C)	T_{decant} (C)	Comments
ML907	Mo10Te90	1000		MoTe2 many phases
ML910	Cr5Te78Ge17	900	500	CrGeTe3
ML911	Cr5Te78Ge17	900	500	CrGeTe3
ML912	Cr5Te78Si17	900	500	CrSiTe3
ML913	Cr5Te78Si17	900	500	CrSiTe3
DR040	W2Te98	1000	460	WTe2
DR041	W2Te98	1000	460	WTe2
ML369	Bi45Se55	725	620	Bi2Se3
ML380	Sr4Bi45Se55	725	620	Goo
ML381	Sr4Bi40Se60	725	620	No SC transition
ML398	Sr4Bi90Se60	850	650	Sr0.1Bi2Se3&BiSe&SrBi2Se4
ML441	Sr2Bi40Se60	850	650	ice quench
ML447	Bi40Se60	850	650	ice quench
ML561	V7Se93	500	230	Lots of Se on the wall, Goo
ML575	V7Se93	500	230	redo of ML561
ML578	V7Se93	500	230	Goo
ML599	V3Se97	600	230	Goo
ML600	V5Se95	600	230	Goo
ML631	Ti0.5Se99.5	650	270	Crucibles coated in Se
ML632	TiSe99	650	270	Goo
ML638	Se96Pt4	600	255	Total spin
ML642	Pt6Se94	600	255	Missed spin.
ML646	Pt6Se94	600	255	PtSe2
ML722	V7Se93	500	230	Goo
ML879	(Ta2Ni)Se99	600	400	Lost a lot as vapor
DR056	Pb14Cr29Se57	850	20	plate:PbSe, hairy globs:PbCr2Se4

APPENDIX B. SALT GROWTH

$EuCd_2As_2$ has hexagonal structure (space group 164) with the lattice parameter of $a = 4.4499\,\mathring{A}$ and $c = 7.350\,\mathring{A}$. A previous magnetization and Mössbauer study shows antiferromagnetic (AFM) transition at $T_N = 9.5\,\mathrm{K}$. [145] Another study on transport properties claimed Kondo-like behavior at low temperature but slightly above the T_N. [146] Recently, $EuCd_2As_2$ was identified as a possible AFM Dirac semimetal with a single Dirac cone crossing the Fermi level. [147] However, another study shows gap opening of Dirac cone at AFM state based on the magnetic structure that they obtained from resonant elastic x-ray scattering experiments. [148] Our DFT calculation of $EuCd_2As_2$ in either a ferromagnetic state or a polarized spin state revealed a pair of Weyl points. [149] In order to experimentally confirm the magnetic Weyl semimetal, we tried to grow the single crystals of $EuCd_2As_2$.

Ref. [145] reported a successful growth of $EuCd_2As_2$ with the salt (NaCl/KCl); Ref. [146, 148] also followed this method. Given that Cd and As have high vapor pressures, there is a very limited phase space to grow $EuCd_2As_2$ with self-flux method. Therefore, we decided to reproduce the previous salt growth. However, the growth procedure outline in Ref. [145] does not provide adequate detail. Given the difficultied and risks associated with both salt and As/Cd-based growths, we decided to test the compatibility of the salt flux and silica tubing first, without any Eu, Cd or As in the ampoule prior.

We put the salt itself into a fused silica ampoule, heated up to 847 °C (the highest temperature that the paper used to grow $EuCd_2As_2$ [145]) and cooled down to room temperature in a furnace. As shown in Fig. B.1 (a), the silica ampoule was cracked while cooling down due to different thermal expansion between the salt and fused silica tube. In order to prevent any leakage through the cracks, double sealed fused silica ampoules were used (see Fig. B.1 (b)).

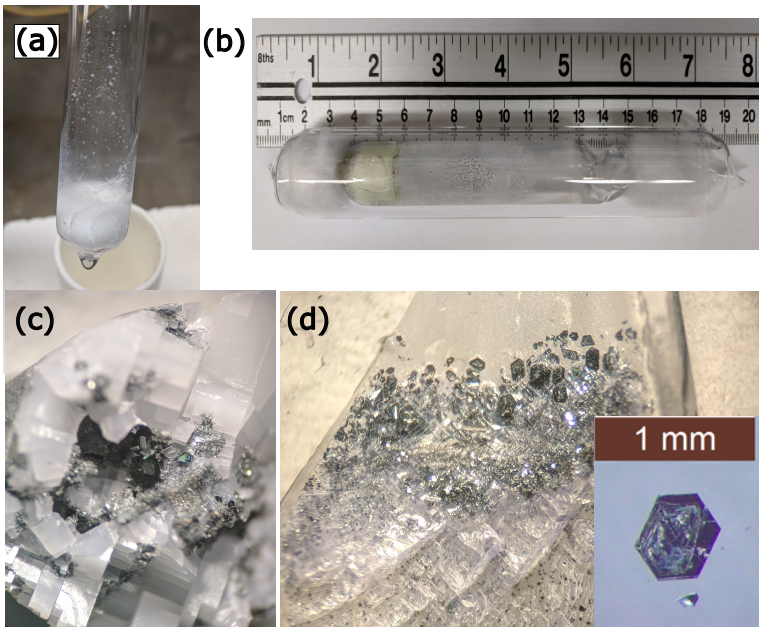

Figure B.1 (a) Salt growth with one fused silica ampoule. (b) Salt growth with two fused silica ampoules, one inside the other. (c) After the salt growth, bottom. (d) After the salt growth, wall. Inset shows the nice single crystals of $EuCd_2As_2$

To be more specific, all the elements including NaCl (Alfa Aesar, ultra dry, 99.99 %) and KCl (Alfa Aesar, Ultra dry, 99.95 %) were weighted and put it into fused silica tube in a glove box with Ar atmosphere. We minimized the air exposure by using a Swagelok ball valve when we move the ampoule from the glove box to glass sealing bench. After sealing the first fused silica tube, we put it into the second fused silica tube, which has slightly larger diameter, with silica wool supporting it on both ends. The ampoule was then heated up to 847 °C, and subsequently slowly cooled to room temperature over 163 hours, which is same temperature profile as the ref. [145]. The outer fused silca tube was fine although the inner fused silica tube was cracked. The results were small sized single crystals of $EuCd_2As_2$ and large sized single crystals of $CdAs_2$.

For the second attempts, we put a seed crystal on the bottom of the fused silica tube and took the ampoule out at 630 °C in order to avoid the binary phase. Single crystals of $EuCd_2As_2$ with hexagonal plates shape are yielded without binary as shown in Fig. B.1 (d). Interestingly, there is not a big difference in the bottom of the tube which means the seed crystal was not helpful. On

the other hand, there were $\sim 0.5\,\mathrm{mm}$ size crystals on the wall of the tube. This may indicate that vapor transport can be a good way to grow the single crystals of $EuCd_2As_2$.

APPENDIX C. SUMMARY OF OTHER PUBLICATIONS

During my PhD, I was also involved in the following projects which were not covered in my dissertation.

C.1 Growth and characterization of BaZnGa

This work was published in Ref. [150]. Here, I suggested the project and was involved all the experimental work.

We report the growth, structure and characterization of BaZnGa, identifying it as the sole known ternary compound in the Ba-Zn-Ga system. Single crystals of BaZnGa can be grown out of excess BaZn and adopt a tI36 structure type. There are three unique Ba sites and three M = Zn/Ga sites. Using DFT calculations we argued that whereas one of these three M sites is probably solely occupied by Ga, the other two M sites, most likely, have mixed Zn/Ga occupancy. Temperature-dependent resistivity and magnetization measurements suggest that BaZnGa is a poor metal with no structural, electronic or magnetic phase transitions between 1.8 and 300 K.

C.2 Pressure induced change in the electronic state of $Ta_4Pd_3Te_{16}$

This work was published in Ref. [151]. Here, I grew the single crystals of $Ta_4Pd_3Te_{16}$, conducted XRD measurement and analysis, and was involved in the pressure experiments and data analysis.

We present measurements of superconducting transition temperature, resistivity, magnetoresistivity, and temperature dependence of the upper critical field of $Ta_4Pd_3Te_{16}$ under pressures up to 16.4 kbar. All measured properties have an anomaly at $\sim$2-4 kbar pressure range; in particular there is a maximum in T_c and upper critical field, $H_{c2}(0)$, and minimum in low temperature, normal state resistivity. Qualitatively, the data can be explained considering the density of state at the Fermi level as a dominant parameter.

C.3 Use of frit-disc crucibles for routine and exploratory solution growth of single crystalline samples

This work was published in Ref. [34]. Here, I conducted $PrZn_{11}$ and Pr_2Zn_{17} experiments

Solution growth of single crystals from high temperature solutions often involves the separation of residual solution from the grown crystals. For many growths of intermetallic compounds, this separation has, historically, been achieved with the use of plugs of silica wool acting as filters during a decanting process. Whereas this is generally efficient in a mechanical sense, it leads to a significant contamination of the decanted liquid with silica fibres. In this paper, we present a simple design for frit-disc alumina crucible sets. Their use to growth single crystals from high temperature solutions is both simple and affordable. An alumina frit-disc allows for the clean separation of the residual liquid from the solid phase. This allows for the reuse of the decanted liquid, either for further growth of the same phase, or for subsequent growth of other, related phases. In this paper, we provide examples of the growth of isotopically substituted $TbCd_6$ and icosahedral i-RCd quasicrystals, as well as the separation of (i) the closely related $Bi_2Rh_3S_2$ and $Bi_2Rh_{3.5}S_2$ phases and (ii) $PrZn_{11}$ and Pr_2Zn_{17}.

C.4 Anisotropic thermodynamic and transport properties of single-crystalline $CaKFe_4As_4$

This work was published in Ref. [152]. Here, I performed TEP and Hall measurements.

Single-crystalline, $CaKFe_4As_4$ was grown out of a high-temperature, quaternary melt. Temperature-dependent measurements of x-ray diffraction, anisotropic electrical resistivity, elastoresistivity, thermoelectric power, Hall effect, magnetization, and specific heat, combined with field-dependent measurements of electrical resistivity and field and pressure-dependent measurements of magnetization indicated that $CaKFe_4As_4$ was an ordered, stoichiometric, Fe-based superconductor with a superconducting critical temperature, $T_c = 35.0 \pm 0.2\,\mathrm{K}$. Other than superconductivity, there was no indication of any other phase transition for $1.8\,\mathrm{K} \leq T \leq 300\,\mathrm{K}$. All of these thermodynamic and transport data revealed striking similarities to those found for optimally doped or slightly

overdoped $(Ba_{1-x}K_x)Fe_2As_2$, suggesting that stoichiometric $CaKFe_4As_4$ was intrinsically close to what is referred to as optimal-doping on a generalized, Fe-based superconductor, phase diagram. The anisotropic superconducting upper critical field, $H_{c2}(T)$, of $CaKFe_4As_4$ was determined up to 630 kOe. The anisotropy parameter $\gamma(T) = H_{c2}^{\perp}/H_{c2}^{\parallel}$, for H applied perpendicular and parallel to the c axis, decreases from ~ 2.5 at T_c to ~ 1.5 at 25 K, which can be explained by interplay of paramagnetic pair breaking and orbital effects. The slopes of $\mathrm{d}H_{c2}^{\parallel}/\mathrm{d}T \sim 44$ kOe/K and $\mathrm{d}H^{\perp})c2/\mathrm{d}T \sim 109$ kOe/K at T_c yield an electron mass anisotropy of $m_{\perp}/m_{\parallel} \sim 1/6$ and short Ginzburg-Landau coherence lengths $\xi_{\parallel}(0) \sim 5.8\,AA$ and $\xi_{\perp}(0) \sim 14.3\,AA$. The value of $H_{c2}^{\perp}(0)$ can be extrapolated to 920 kOe, well above the BCS paramagnetic limit.

C.5 ^{125}Te NMR and Seebeck effect in Bi_2Te_3 synthesized from stoichiometric and Te-rich melts

This work was published in Ref. [153]. Here, I grew the single crystals of Bi_2Te_3.

Bi_2Te_3 is a well-known thermoelectric material and, as a new form of quantum matter, a topological insulator. Variation of local chemical composition in Bi_2Te_3 results in formation of several types of atomic defects, including Bi and Te vacancies and Bi and Te antisite defects; these defects can strongly affect material functionality via generation of free electrons and/or holes. Nonuniform distribution of atomic defects produces electronic inhomogeneity, which can be detected by ^{125}Te nuclear magnetic resonance (NMR). Here we reported on ^{125}Te NMR and Seebeck effect measurements for two single crystalline samples: (#1) grown from stoichiometric composition by Bridgman technique and (#2) grown out of Te-rich, high temperature flux. The Seebeck coefficients of these samples showed p- and n-type conductivity, respectively, arising from different atomic defects. ^{125}Te NMR spectra and spin-lattice relaxation measurements demonstrate that both Bi_2Te_3 samples were electronically inhomogeneous at the atomic scale, which can be attributed to a different Te environment due to spatial variation of the Bi/Te ratio and formation of atomic defects. Correlations between ^{125}Te NMR spectra, spinlattice relaxation times, the Seebeck coefficients, carrier concen-

trations, and atomic defects were discussed. Our data demonstrated that ^{125}Te NMR is an effective probe to study antisite defects in Bi_2Te_3.

C.6 On magnetic structure of $CuFe_2Ge_2$: constrains from the ^{57}Fe Mössbauer spectroscopy

This work was published in Ref. [154]. Here, I was involved in crystal growth, performed XRD measurement and analysis.

^{57}Fe Mössbauer spectroscopy measurements were performed on a powdered $CuFe_2Ge_2$ sample that ordered antiferromagnetically at ~ 175 K. Whereas a paramagnetic doublet was observed above the Néel temperature, a superposition of paramagnetic doublet and magnetic sextet (in approximately 0.5 : 0.5 ratio) was observed in the magnetically ordered state, suggesting a magnetic structure similar to a double-Q spin density wave with half of the Fe paramagnetic and another half bearing static moment of ~ 0.5 - 1 μ_B. These results called for a re-evaluation of the recent neutron scattering data [155] and band structure calculations, [156] as well as for a deeper examination of the details of sample preparation techniques.

C.7 Reduction of the ordered magnetic moment and its relationship to Kondo coherence in $Ce_{1-x}La_xCu_2Ge_2$

This work was published in Ref. [157]. Here, I was involved in crystal growth.

The microscopic details of the suppression of antiferromagnetic order in the Kondo-lattice series $Ce_{1x}La_xCu_2Ge_2$ due to nonmagnetic dilution by La were revealed through neutron diffraction results for x = 0.20, 0.40, 0.75, and 0.85. Magnetic Bragg peaks were found for $0.20 \leq x \leq 0.75$, and both the Néel temperature T_N and the ordered magnetic moment per Ce, μ, linearly decrease with increasing x. The reduction in μ pointed to strong hybridization of the increasingly diluted Ce $4f$ electrons, and we found a remarkable quadratic dependence of μ on the Kondo-coherence temperature. We discussed our results in terms of local-moment- versus itinerant-type magnetism

and mean-field theory and showed that $Ce_{1x}La_xCu_2Ge_2$ provides an exceptional opportunity to quantitatively study the multiple magnetic interactions in a Kondo lattice.

C.8 Single crystal growth and magnetic properties of the mixed valent Yb containing Zintl phase, $Yb_{14}MgSb_{11}$

This work was published in Ref. [158]. Here, I was involved in crystal growth, physical property measurements and analysis.

Large crystals of $Yb_{14}MgSb_{11}$ were grown through a Sn flux method. [159] Magnetic susceptibility measurements yielded an effective magnetic moment of $3.4(1)\,\mu_B$, revealing the presence of both divalent and trivalent Yb in $Yb_{14}MgSb_{11}$. Previously assumed to only contain Yb^{2+} as in $Yb_{14}MgSb_{11}$, the mixed valency demonstrates that $Yb_{14}MgSb_{11}$ is a Zintl phase.

C.9 Nodeless superconductivity in the type-II Dirac semimetal $PdTe_2$: London penetration depth and pairing-symmetry analysis

This work was published in Ref. [160]. Here, I grew the single crystals of $PdTe_2$, and conducted XRD measurement and analysis.

The superconducting gap structure was probed in type-II Dirac semimetal, $PdTe_2$, by measuring the London penetration depth using the tunnel diode resonator technique. At low temperatures, the data for two samples were well described by a weak-coupling exponential fit yielding $\lambda\,(T = 0) = 230\,\mathrm{nm}$ as the only fit parameter at a fixed $\Delta(0)/T_c \approx 1.76$, and the calculated superfluid density was consistent with a fully gapped superconducting state characterized by a single gap scale. Electrical resistivity measurements for in-plane and inter-plane current directions found a very low, and nearly temperature-independent, normal-state anisotropy. The temperature dependence of resistivity was typical for conventional phonon scattering in metals. We compare these experimental results with expectations from a detailed theoretical symmetry analysis and reduce the number of possible superconducting pairing states in $PdTe_2$ to only three nodeless candidates: a regular, topologically trivial s-wave pairing, and two distinct odd-parity triplet states that both can be

topologically nontrivial depending on the microscopic interactions driving the superconducting instability.

APPENDIX D. POEMS

Amerian limerick:

There once was a student so kind
She was a most glorious find
The sample she studied were planes
with great stresses and strains
and analysis all done in her mind

Korean sijo:

There once was a student called trouble maker,
who was fascinated by materials with layers.
Her search for a fragile magnet failed,
and her study to find the origin of XMR did not prevail.
BUT! The strain study on WTe_2 was fruitful.
Her ARPES study on layered materials will be crucial.